Summer 2016

Repetitive process control of additive manufacturing with application to laser metal deposition

Patrick M. Sammons

Department: Mechanical and Aerospace Engineering

REPETITIVE PROCESS CONTROL OF ADDITIVE MANUFACTURING WITH APPLICATION TO LASER METAL DEPOSITION

by

PATRICK MICHAEL SAMMONS

A DISSERTATION

Presented to the Faculty of the Graduate School of the

MISSOURI UNIVERSITY OF SCIENCE AND TECHNOLOGY

In Partial Fulfillment of the Requirements for the Degree

DOCTOR OF PHILOSOPHY

in

MECHANICAL ENGINEERING

2016

Approved

Douglas A. Bristow, Advisor

Robert G. Landers, Advisor

S.N. Balakrishnan

Frank Liou

Jagannathan Sarangapani

ABSTRACT

Additive Manufacturing (AM) is a set of manufacturing processes which has promise in the production of complex, functional structures that cannot be fabricated with conventional manufacturing and the repair of high-value parts. However, a significant challenge to the adoption of additive manufacturing processes to these applications is proper process control. In order to enable closed-loop process control compact models suitable for control design and for describing the layer-by-layer material addition process are needed. This dissertation proposes a two-dimensional modeling and control framework, with an application to a specific metal-based AM process, whereby the deposition of the current layer is affected by both in-layer and layer-to-layer dynamics, both of which are driven by the state of the previous layer. The proposed modeling framework can be used to create two-dimensional dynamic models for the analysis of layer-to-layer stability and as a foundation for the design of layer-to-layer controllers for AM processes. In order to analyze the stability of this class of systems, linear repetitive process results are extended enabling the treatment of the process model as a two-dimensional analog of a discrete time system. For process control, the closed-loop repetitive process is again treated as a two-dimensional analog of a discrete time system for which controllers are designed. The proposed methodologies are applied to a metal-based AM process, Laser Metal Deposition (LMD), which is known to exhibit layer-to-layer unstable behavior and is also of significant interest to high-value manufacturing industries.

ACKNOWLEDGEMENTS

The work presented here would not have been possible without the significant mentoring and guidance provided by my advisors, Dr. Douglas A. Bristow and Dr. Robert G. Landers. They not only provided me the necessary tools and resources I needed to complete my dissertation work, but also enabled me to gain experience on a multitude of other engineering and research projects. The time I have spent at Missouri S&T under their guidance has profoundly shaped my professional and academic view and I am forever grateful for everything they have allowed me to accomplish.

I would like to also acknowledge the financial support of the National Science Foundation (CMMI1301414) and the US Department of Education GAANN Fellowship (P200A120062). Further, Optomec, MachMotion, and Dr. Frank Liou's Laser Aided Manufacturing Processes (LAMP) Lab provided essential access to resources and equipment in the completion of this work. I am appreciative of Drs. S.N. Balakrishnan, Frank Liou, and Jagannathan Sarangapani for their membership on my dissertation committee.

Although it has never been easy for me to communicate the personal and professional importance of this endeavor to my family or friends (or really anything else for that matter!), their support has never wavered. Specifically, I want to express my deep gratitude to my parents Jon and Kathie Sammons and my other half Liz Harris for putting up with the long hours and distance, the requisite dog sitting, and for all other intangible burdens they have borne during the past four years.

TABLE OF CONTENTS

LIST OF ILLUSTRATIONS

LIST OF TABLES

1. INTRODUCTION

Additive Manufacturing (AM) processes are increasingly becoming an attractive option for industry to build monolithic, complex parts with designed morphologies and material properties. While there is significant promise for AM processes, they currently lack the enabling technologies that would allow them to become viable production-level alternatives to conventional manufacturing processes. This section serves to introduce AM, its potential applications and current research problems, and a brief description of the class of systems to which AM processes belong; repetitive processes.

1.1. ADDITIVE MANUFACTURING

Additive Manufacturing is a growing class of manufacturing processes in which parts are fabricated by adding material in a layer-by-layer fashion. While the underlying governing physics vary significantly from process to process [Huang 2014], most AM processes share a common part fabrication procedure. Within each layer, a material-accretion source is traced along a pre-defined toolpath, which is generated directly from a CAD model [Pandey 2003]. At each position along the toolpath, process inputs are commanded in an attempt to produce the desired layer morphology or material properties. At the end of the toolpath, the process is indexed to the next layer, and another layer of material is accreted on top of the previous layer. This repeated addition of material creates layer-to-layer dynamics, as the formation of the current layer is now affected by both the in-layer process dynamics and the states of the previous layer, e.g. its morphology. This fabrication paradigm is in contrast to what is typically termed

conventional or subtractive manufacturing where a part is made by removing material from bulk raw material. A schematic of the AM process flow is shown in Figure 1.1.

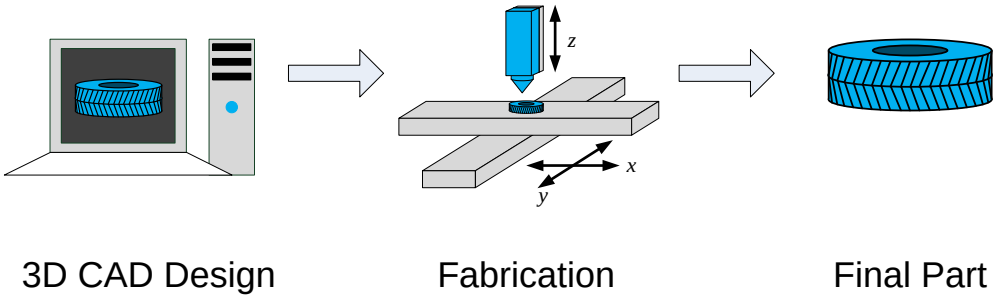

Figure 1.1. Schematic of the additive manufacturing process flow.

AM processes are attracting interest across several industries for production use for several reasons. First, AM processes are generally capable of a wider range of geometries than subtractive manufacturing with less tooling, including internal structures and overhang geometries, as a result of the layer by layer fabrication paradigm. Because of this property, the cost of geometric complexity in the design stage of parts is extremely low as compared to conventional manufacturing processes. Secondly, because AM processes typically take material from one state, though an amorphous state, to a final solid state through an energy exchange process, it is possible to obtain a variety of material properties within a given part. Finally, because the virtually zero tooling requirements and the low design costs, AM processes are well adapted to creating small volume or one-off parts. This is a particularly attractive feature in high-value industries

such as aerospace and medical implants. Despite these advantages however, AM processes have yet achieved their full potential.

While some commercially available processes incorporate in-layer process sensing and feedback control [Optomec 2015], layer-to-layer fabrication is typically not regulated systematically and process control is largely carried out using operator knowledge or process maps in an ad hoc manner [Raghunath 2007, Dwivedi, 2005, Han 2003, Vasinonta 2007, Zhou, 2012, Limaye 2007]. Fabricating parts in this uncontrolled, open-loop manner can lead to dimensional instability, e.g. the height rippling phenomenon seen in the structure in in Figure 1.2 fabricated using constant process parameters in a Laser Metal Deposition (LMD) process [Sammons 2013, Ruan 2010]. The ripple, highlighted by the added white lines in Figure 1.2, increases in magnitude as it propagates from one layer to the next. Although for certain processes, such as LMD [e.g., Fathi et al., 2008; Tang and Landers, 2010, Tang and Landers, 2011, Duomanidis, 2000, Song 2012], Selective Laser Sintering (SLS) [Craeghs 2010], and Electron Beam Melting (EBM) [Mireles 2015, Gockel 2014], some work has been dedicated to closed-loop process control, process control for metal AM in general has received relatively little attention, creating a major obstacle to the widespread adoption of LMD [NIST 2013, UT, 2009]. Therefore, process models that describe, and control methods that incorporate, both the in-layer and layer-to-layer fabrication phenomena are needed.

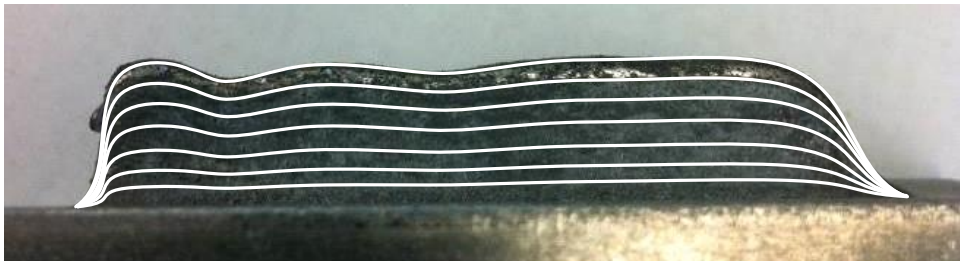

Figure 1.2. Structure fabricated with constant process parameters (Laser Power, 600 W; Scan Speed, 2.54 mm/s; Powder Flow Rate, 3.73 g/min) in a LMD process. White lines are drawn to highlight individual layers.

1.2. LASER METAL DEPOSITION

Metal AM processes, such as LMD [Mazumder 1997, Mazumder 2000, Atwood 1993], have received considerable attention for their ability to create serviceable parts with properties comparable to annealed wrought or forged material [Mazumder 1997, Baufelt 2009, Paul 2007]. In the LMD process, also known as Direct Metal Deposition (DMD) or Laser Engineered Net Shaping (LENS), powdered metal is delivered by a carrier gas through a cladding head or nozzle into a laser beam in order to form a molten metal bead on a substrate. The substrate is mounted on a motion stage which is controlled via a toolpath generation software to trace a pre-defined tool path. In this way, functional, complex metal parts are fabricated. The process can be used in the repair of high-value parts, fabricating one-off metal components, and manufacturing material-graded structures. A schematic of the LMD process is shown in Figure 1.3.

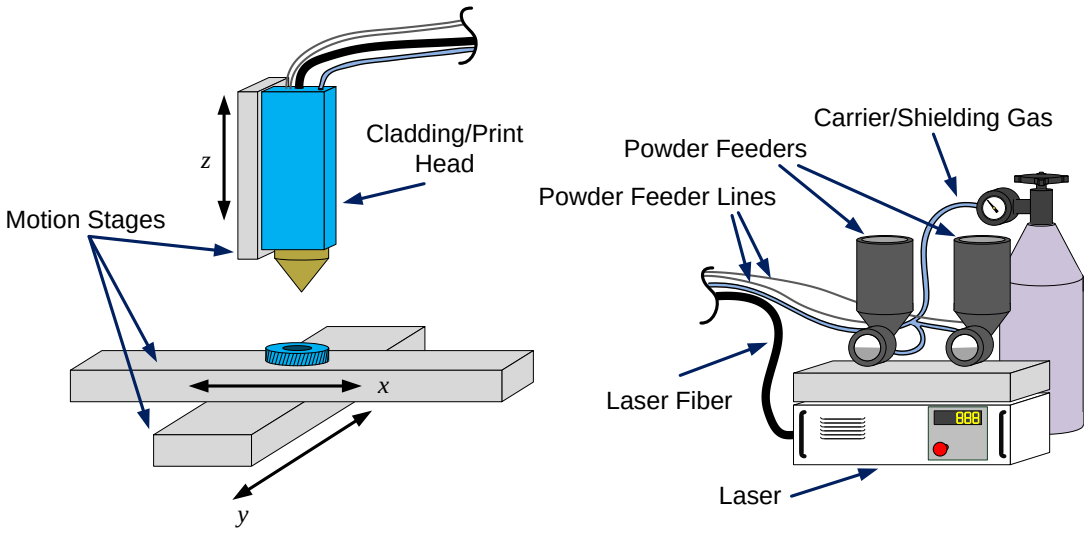

Figure 1.3. Schematic of a Laser Metal Deposition system.

Dynamic LMD process models largely fall into two distinct categories: single layer and multi-layer. While many of these studies involve high order finite element models, e.g., [Peyre 2008], which are generally too complex for control synthesis or computationally intensive for real-time implementation, other work investigates lumped parameter models for single layer beads deposited on a substrate [e.g.,Duomanidis 2001, Pinkerton 2004, Munjuluri 2001, Fathi 2007, Boddu 2001]. Some investigators have attempted to capture the multi-layer nature of the LMD process. However, extensions of these lumped parameter models to multiple layers is challenging because it is difficult to predict the melt pool thermal boundary conditions for increasing numbers of layers and complex geometries [Sammons 2013]. Despite their complexity, these model in general provide a much more detailed description of the entire operating space of LMD.

While model accuracy over a large operating space is advantageous, typical LMD operation is conducted over an extremely small range of the operating space. Because of

this, trying to capture the behavior of the process over the entire operating space is an unnecessary task. An alternative modeling approach is to describe the important in-layer material accretion phenomena describing and the layer-to-layer dynamics, while remaining suitable for the design and implementation of process controllers, around a pre-defined operating point. The proposed model has a two-dimensional Hammerstein-Weiner structure where inputs are cascaded through a linear *layer-to-layer* dynamic operator, then through a static nonlinearity, and finally through a linear *in-layer* dynamic operator. This model structure is typically denoted Linear-Nonlinear-Linear (LNL) for one-dimensional systems, although here it is extended to a class of two-dimensional repetitive processes. A system identification framework for the AM repetitive process description, demonstrated through an application to the LMD process, is utilized to completely characterize the dynamic process.

For Laser Metal Deposition, current process control methods typically only consider dynamics describing how the process evolves within a layer, termed in-layer dynamics, in the control design. However, because LMD is a two-dimensional dynamic process, neglecting the dynamics which describe how the process evolves from layer-to-layer in modeling and process control can lead to dimensional instability. The instability caused by these dynamics, termed the layer-to-layer dynamics, can potentially cause catastrophic defects in the deposited part, c.f. Figure 1.2 and in [Tang 2010]. While recent work was concerned with controlling a similar process via an iterative learning control algorithm [Heralic 2012], the coupling between the in-layer and layer-to-layer dynamics was not considered. Incorporating both the spatial and layer-to-layer dynamics

into the process control design and analysis requires a set of control design methods that have not previously been used in AM process control.

There are generally two viable methodologies for control of repetitive processes; feedback control and a combination of feedforward and feedback control. Because repetitive processes operate over two dimensions, pure feedback control in general includes feedback in both dimensions, i.e., the in-layer and the layer-to-layer domains. Here, however, because LMD measurement information for an entire layer is most easily recorded or processed *a posteriori*, feedback control refers to feedback purely in the layer-to-layer domain. That is, the measurements on a given layer are used to inform the control law for the next layer. This control strategy is termed layer-to-layer control and is employed in this work. This paradigm is also applied in the feedforward case; information regarding references or disturbances is fed forward in the layer-to-layer domain. While this paradigm essentially treats the in-layer dynamics as operating in open-loop, feedback controllers in this domain can be considered as part of the process dynamics.

As mentioned above, the AM process flow includes a step where the tool path for each layer is generated before the actual part is fabricated. Because of this property, the entire part reference as a function of both layer and position is generally known *a priori*. In some scenarios, the reference generated in this step is slowly changing with respect to the layer domain. When this is true, a pure layer-to-layer feedback controller can be utilized to achieve reasonable tracking performance during the part fabrication. However, in many cases, the reference is generally non-periodic. That is, reference features required to be fabricated on one layer are not necessarily present on any of the

previous or subsequent layers. In this case, a purely layer-to-layer feedback controller will exhibit poor performance as the reference signal contains layer-to-layer frequency content beyond the controller bandwidth. Fortunately, because the reference information is known, a combination of feedback and feedforward methods (the latter utilizing the known future reference information) can significantly improve tracking performance.

There are several possible techniques that enable the use of future reference signals in order to minimize tracking error. One such technique, Model Predictive Control (MPC) [Garcia 1989], uses a model of the system to estimate the trajectory of the system at future time instances. Then, a control law is calculated to minimize a cost function based on the predicted deviation of the system from the reference. Typically however, because the class of references for which the large majority of MPC literature considers is constant set-points, the horizon over which the MPC law is calculated is infinite and there exists an analytical solution based on solving a set of matrix equations [Pannocchia 2005, Maeder 2009] as each process measurement is received. Here, a the MPC control methodology is used to estimate the system over a finite horizon explicitly incorporating the non-constant references for AM processes and is extended to treat AM processes by transforming the two-dimensional dynamics into an equivalent Multiple Input, Multiple Output (MIMO) discrete time system.

1.3. REPETITIVE PROCESSES

In general, repetitive processes are those dynamic process which operate on a trial by trial basis and contain inherent trial-to-trial memory [Rogers 2007]. On each finite

duration pass or trial, an output profile is created. The output profile of previous passes or trials then acts as a forcing function on the dynamics of subsequent passes or trials.

The first research on repetitive processes began at the University of Sheffield in the United Kingdom in the early 1970's. The impetus for the investigation was the dynamic characteristics of the long wall coal mining, metal rolling processes, and self-steering tractors (before the advent of GPS-steered tractors) [Edwards 1974]. In both of these processes, each pass is explicitly a function of the previous pass. From the outset of research on these repetitive processes, it was observed that an initial pass could exhibit perfectly acceptable temporal dynamics, but lead to subsequent passes in which oscillations amplified in magnitude from pass to pass. These experimental observations lead to the necessary development of stability requirements of repetitive processes. In the following decades, significant contributions to the field of repetitive process control was made including well defined concepts of stability and process descriptions [Galkowski 1999, Dymkov 2002, Rocha 1996]. The specifics of repetitive process representation and analysis are given in the preliminaries section below.

In more recent years, Linear Matrix Inequalities (LMIs) have become the *de facto* control design methodology for pass-to-pass control laws, including pass-to-pass PI and H_∞ controllers [Sulikowski 2006, Galkowski 2002, Paszke 2006]. While LMIs are well suited for designing controllers for processes which are easily represented in a state space form, other representations, e.g., the LNL representation described above, do not lend themselves to LMIs. Therefore, there is a need to broaden the methodologies for designing pass-to-pass controllers.

1.4. OUTLINE

This dissertation addresses modeling and control of Additive Manufacturing processes, with a specific application to the Laser Metal Deposition process. In order to present the modeling and control sections succinctly, this section ends with a set of mathematical preliminaries that will prime the reader and be used throughout the dissertation. Section 2 presents the two-dimensional model and the application to a commercial LMD process. Section 3 presents a model identification methodology and model validation results, generated on the same LMD system on which the modeling is based. Section 4 details the open-loop stability conditions for AM processes which can be modeled using the framework presented in Section 2 again with a specific application to the LMD process. The stability criterion is then used to generate a series of open-loop stability maps for various types of LMD deposition heads. Section 5 presents two control methodologies for AM processes; a feedback algorithm design using a pole-placement procedure and combination feedforward-feedback methodology which borrows from conventional Model Predictive Control (MPC). Finally, Section 6 presents a summary of the work and provides conclusions and some statements regarding future directions.

1.5. PRELIMINARIES

Definition 1.1 [Adapted from Rogers 2007]: A linear repetitive process consists of a Banach space $\mathcal{X}$, a linear subspace $\mathcal{Y}$ of $\mathcal{X}$, a collection of bounded linear operators $\{\mathbf{L}^{(k_\mathbf{L})}\}_{k_\mathbf{L}\geq 1}^{M_\mathbf{L}}$ ($M_\mathbf{L} < \infty$), and $\{\mathbf{T}^{(k_\mathbf{T})}\}_{k_\mathbf{T}\geq 1}^{M_\mathbf{T}}$ ($M_\mathbf{T} < \infty$) mapping $\mathcal{X}$ into itself. The dynamics of a linear repetitive process are described by a linear recursion relation of the form

$$\mathbf{y}(x,j)=\mathbf{L}^{(1)}\mathbf{y}(x,j-1)+\cdots+\mathbf{L}^{(M_{\mathbf{L}})}\mathbf{y}(x,j-M_{\mathbf{L}})+\mathbf{T}^{(0)}\mathbf{u}(x,j)+\cdots+\mathbf{T}^{(M_{\mathbf{T}})}\mathbf{u}(x,j-M_{\mathbf{T}}) \quad (1)$$

where $\mathbf{y}(x,j)\in\mathcal{X}$ is the linear repetitive process output at a position *x* on pass *j*, the operator $\mathbf{L}^{(k_{\mathbf{L}})}\in B(\mathcal{X},\mathcal{X})$ maps outputs from pass $j - k_{\mathbf{L}}$ to outputs on the current pass *j*, $\mathbf{u}(x,j)\in\mathcal{Y}\subset\mathcal{X}$ represents disturbances and inputs to the linear repetitive process, and $\mathbf{T}^{(k_{\mathbf{T}})}\in B(\mathcal{X},\mathcal{X})$ maps inputs or disturbances from pass $j - k_{\mathbf{T}}$ to outputs on the current pass *j*.

Definition 1.2 [Adapted from Rogers 2007]: The linear repetitive process (1) is said to be *stable along the pass* if there exists finite real scalars $M_\infty>0$ and $\gamma_\infty\in(0,1)$ which, for each pass-to-pass constant bounded sequence $\mathbf{u}(x,j)=\mathbf{u}(x,\infty),\ j\geq 0$, ensure the output sequence $\{\mathbf{y}(x,j)\}_{j\geq 0}$ satisfies

$$\|\mathbf{y}(x,j)-\mathbf{y}(x,\infty)\|\leq M_\infty\gamma_\infty^j\left(\|\mathbf{y}(x,0)\|+\frac{\|\mathbf{u}(x,\infty)\|}{1-\gamma_\infty}\right),\ j\geq 0 \quad (2)$$

where $\mathbf{y}(x,\infty)$ is an equilibrium pass profile and $\mathbf{y}(x,0)$ is an initial pass profile.

Remark 1.1: The definition for stability along the pass (2) requires both asymptotic stability in the *x* direction and asymptotic stability in the *j* direction. While this definition may be unusual to readers unfamiliar with two-dimensional dynamics, physically it

requires that the system output on any given pass be bounded and that on each successive pass, the output converge asymptotically to a pass-independent profile, e.g., the origin.

The one-sided *w*-transformation and bi-lateral Laplace transform of the signal $\mathbf{y}(x,j)$, respectively, are

$$\begin{aligned}\mathbf{Y}(x,w) &= \mathcal{W}\{\mathbf{y}(x,j)\} \\ &= \sum_{j=0}^{\infty} \mathbf{y}(x,j)\, w^{-j}\end{aligned} \tag{3}$$

$$\begin{aligned}\mathbf{Y}(s,j) &= \mathcal{L}\{\mathbf{y}(x,j)\} \\ &= \int_{-\infty}^{\infty} e^{-sx}\mathbf{y}(x,j)\,\mathrm{d}x\end{aligned} . \tag{4}$$

Combining both definitions, the Hybrid Laplace-W Transformation (HLWT) is then [Prepelita 2010],

$$\begin{aligned}\mathbf{Y}(s,w) &= \mathcal{L}\mathcal{W}\{\mathbf{y}(x,j)\} \\ &= \mathcal{W}\mathcal{L}\{\mathbf{y}(x,j)\} \\ &= \int_{-\infty}^{\infty} e^{-sx}\left[\sum_{j=0}^{\infty}\left[\mathbf{y}(x,j)\right] w^{-j}\right]\mathrm{d}x\end{aligned} . \tag{5}$$

Inverse transforms can be defined in a similar fashion. System transforms are determined analogously to their one-dimensional counterparts.

Definition 1.3: A linear operator **P** is said to be spatially- and pass-invariant (shift-invariant) if, given the input-output pair $\mathbf{y}_{out}(x, j) = \mathbf{P}\mathbf{y}_{in}(x, j-k)$ for all $(x, j) \in \mathbb{R} \times \mathbb{Z}_+$, then $\mathbf{y}_{out}(x-\tau_x, j-\tau_j) = \mathbf{P}\mathbf{y}_{in}(x-\tau_x, j-k-\tau_j)$ for any $(\tau_x, \tau_j) \in \mathbb{R} \times \mathbb{Z}$.

When $\mathbf{L}^{(k_\mathbf{L})}$ for $k_\mathbf{L} = 1, 2, \ldots, M_\mathbf{L}$ and $\mathbf{T}^{(k_\mathbf{T})}$ for $k_\mathbf{T} = 1, 2, \ldots, M_\mathbf{T}$ are spatial- and pass-invariant, (1) can be converted to the (s,w)-domain by applying the HLWT to give

$$\mathbf{Y}(s,w) = \underbrace{\left[\mathbf{I} - \mathbf{L}^{(1)}(s)w^{-1} - \cdots - \mathbf{L}^{(M_\mathbf{L})}(s)w^{-M_\mathbf{L}}\right]^{-1}\mathbf{T}(s,w)}_{\mathbf{G}(s,w)}\mathbf{U}(s,w) \tag{6}$$

where **I** is an appropriately sized identity matrix, $\mathbf{T}(s,w) = \sum_{k_\mathbf{T}=0}^{M_\mathbf{T}} \mathbf{T}^{(k_\mathbf{T})}(s)w^{-k_\mathbf{T}}$, $\mathbf{T}^{(k_\mathbf{T})}(s)$ is the Laplace transform of $\mathbf{T}^{(k_\mathbf{T})}$, and $\mathbf{L}^{(k_\mathbf{L})}(s)$ is the Laplace transform of $\mathbf{L}^{(k_\mathbf{L})}$. Equation (6) is termed the two-dimensional transfer function representation of the linear repetitive process (1).

Define the interpass transfer function matrix $\mathcal{G}$ and the constant direct-feedthrough interpass matrix $\mathcal{D}$, respectively, as

$$\mathcal{G}(s) = \begin{bmatrix} 0 & \mathbf{I} & \cdots & 0 \\ \vdots & \vdots & & \vdots \\ 0 & \cdots & 0 & \mathbf{I} \\ -\mathbf{L}^{(k_\mathbf{L})}(s) & \cdots & -\mathbf{L}^{(2)}(s) & -\mathbf{L}^{(1)}(s) \end{bmatrix} \tag{7}$$

$$\mathcal{D} = \lim_{\omega_1 \to \infty} \mathcal{G}(i\omega_1) \tag{8}$$

where ω_1 is the in-layer frequency. The following theorem gives conditions for stability along the pass for processes of the form (6).

Theorem 1.1 [Rogers 1989]: The linear repetitive process (6) is stable along the pass if, and only if,

a. The in-layer processes $\{\mathbf{L}^{(k_L)}\}_{k_L \geq 1}^{M_L}$ and $\{\mathbf{T}^{(k_L)}\}_{k_T \geq 1}^{M_T}$ are asymptotically stable in the conventional 1D sense

b. All eigenvalues of the matrix $\mathcal{D}$ have magnitude strictly less than one, alternatively the spectral radius is bounded by unity $\rho(\mathcal{D}) < 1$,

c. All eigenvalues of the matrix $\mathcal{G}(s)$ evaluated at $s = i\omega_1$ have magnitude strictly less than one.

In subsequent sections, a general framework of AM processes will be used to aid in analysis and to generalize the techniques used here. The two-dimensional framework is a Linear-Nonlinear-Linear (LNL) system where inputs are first cascaded to a linear dynamic block in the layer-to-layer domain, then into a static nonlinearity, and finally into a linear dynamic block in the layer domain. A general Linear-Nonlinear-Linear structure of this form is shown schematically in Figure 1.4 and is given by,

$$\begin{aligned} \boldsymbol{\upsilon}(x, j) &= G_1(w)\begin{bmatrix}\mathbf{u}(x, j)\\ \mathbf{y}(x, j)\end{bmatrix} \\ \mathbf{y}(x, j) &= G_2(s)\, f\left(\boldsymbol{\upsilon}(x, j)\right) \end{aligned} \tag{9}$$

where $\boldsymbol{\upsilon} \in \mathbb{R}^m$ is a vector of intermediate states, $G_1 : \mathbb{R}^{n+p} \to \mathbb{R}^m$ is a linear dynamic operator representing the process layer-to-layer dynamics, $\mathbf{u} \in \mathbb{R}^p$ is the set of process inputs, $\mathbf{y} \in \mathbb{R}^n$ is the set of process outputs, $G_2 : \mathbb{R}^r \to \mathbb{R}^n$ is a linear dynamic operator representing the in-layer dynamics, and $f : \mathbb{R}^m \to \mathbb{R}^r$ is a static nonlinearity. While not explicitly denoted in (9), the output of the nonlinearity *f*, and the input to the linear in-layer dynamic operator G_2, is denoted in Figure 1.3 by $\boldsymbol{\xi}(x, j) \in \mathbb{R}^r$.

Remark 1.2: With respect to the input-output relationship, G_1, *f*, and G_2 do not constitute a unique set of operators. That is, the input-output relationship between **u** and **y** can be preserved with a possibly different selection of G_1, *f*, and G_2.

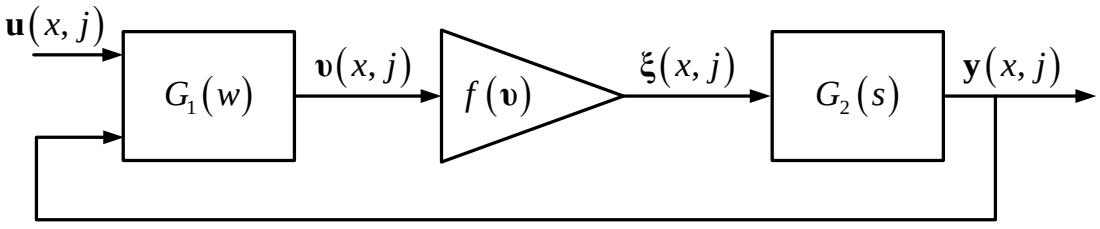

Figure 1.4. Linear-Nonlinear-Linear LMD process model schematic.

2. TWO-DIMENSIONAL LASER METAL DEPOSITION MODEL

As detailed above, generally any dynamic system which operates in a trial-by-trial manner and possesses internal trial-to-trial memory can be classified as a repetitive process [Rogers 2007]. For AM processes, the repetitive accretion of material creates internal process layer-to-layer memory. Therefore, a logical framework for describing AM processes is that of repetitive processes, where the trial analog is layer. Below, a novel single layer LMD model is presented first, and the model is then extended into the multi-layer framework. Finally, a discussion of how the LMD model presented here fits into the general modeling framework presented in Section 1.5 is given along with some comments on how other similar AM process could be similarly described by the modeling framework presented above.

Because a major goal of the modeling efforts presented below is that the resulting model be suitable for control synthesis, model simplicity is valued over comprehensiveness. That is, the model of the LMD process presented below is intended to be accurate only over small ranges of the process parameter space. One can interpret the modeling approach below as being a linear approximation of the underlying highly nonlinear LMD process dynamics near a set of processing parameters.

2.1. MELT POOL MODEL

A typical LMD system consists of two main components; a static cladding head, or nozzle, containing a laser energy source, a powder material source coaxial with the laser, and a motion stage onto which a substrate is mounted [Mazumder 2000, Atwood 1998] (see Figure 1.3). At each position along the toolpath, the laser melts a fraction of

the powder coming from the nozzle to form a molten metal pool. As the substrate moves the molten pool from underneath the nozzle, the pool solidifies, resulting in a continuous solidified structure. To model this process, consider a differential volume of material deposited directly under the nozzle,

$$\mathrm{d}V = \varsigma\mu\frac{\mathrm{d}M}{\mathrm{d}x} = \varsigma\mu\frac{\mathrm{d}M/\mathrm{d}t}{\mathrm{d}x/\mathrm{d}t} \tag{10}$$

where dV is the differential volume (mm^3/mm) captured by the existing melt pool, dM is the differential mass released by the nozzle (kg), μ is the powder catchment efficiency (mass captured/mass released), $\varsigma = \rho^{-1}$ is the material specific volume (mm^3/kg), dx is the substrate differential travel (mm), and dt is the differential time (s). Then, the differential volume captured by the melt pool at a position x, measured in the direction of deposition (mm) is,

$$\mathrm{d}V(x) = \varsigma\mu(x)\frac{\dot{m}(x)}{v(x)} = \varsigma\mu(x)\lambda(x) \tag{11}$$

where $\dot{m}$ is the powder flow rate (kg/s), v is the scan speed (mm/s), and $\lambda = \dot{m}/v$ is the powder spatial flow rate (kg/mm) describing the instantaneous amount of powder released per unit travel of the substrate.

Once material enters the melt pool it experiences flow due to complex thermal and fluid flow phenomena including surface tension forces, convective flow, and viscous forces [Qi 2006, Lei 2001, Picasso 1994]. As the cladding head and solidification front

advance, the faster internal melt pool dynamics [Hoadley 1992] force the melt pool pre-solidification morphology into a shape that is typically ellipsoidal [Doumanidis 2001, Pinkerton 2004]. For operation near a set of defined process parameters, a locally linear model of the steady-state morphology may be assumed. Thus, the cross-sectional area of the solidified bead can be described as,

$$a(x) = \int_0^x \mathrm{d}V(x-\tau)\, f_s(\tau)\,\mathrm{d}\tau \tag{12}$$

where a is the solidified bead cross-sectional area (mm^2) and f_s is a morphology kernel describing the melt pool flow (mm^{-1}). As the morphology kernel represents the relocation of material inside the melt pool, it is constrained by the conservation of mass which requires that material cannot be created or destroyed by the melt pool flow process or,

$$\int_{-\infty}^{\infty} f_s(x)\,\mathrm{d}x = 1, \tag{13}$$

and that the melt pool area must be positive or,

$$f_s(x) \geq 0, \ \forall x. \tag{14}$$

Additional results from the literature will be applied in Section 2.2 to further refine the morphology kernel model.

In general, the relationship between the bead area and bead height is nonlinear and described as

$$\delta h(x) = f_h\left(a(x)\right)$$

where δh is the bead height (mm) and f_h is a static mapping between bead area and bead height. However, in LMD the relationship between the bead area, a, and the bead height is typically modeled statically [Fathi 2007, Hoadley 1992, Kaplan 2001], with the bead height being a principle axis of an elliptic bead area description [Doumanidis 2001, Steen 1986]. Thus, the height of the solidified bead is modeled here as,

$$\delta h(x) = b^{-1}a(x) \tag{15}$$

where b is the characteristic bead width (mm) and $f_h(a(x)) = b^{-1}a(x)$.

2.2. THE MORPHOLOGY KERNEL

As demonstrated above, a typical method for describing the melt pool morphology in an LMD process model is to ascribe a shape function to the melt pool. Here, this methodology is used to obtain a model for the morphology kernel, f_s. Again, as above, several works [e.g., Doumanidis 2001, Pinkerton 2004] model the melt pool shape as a quarter-ellipsoid with principle radii forming the melt pool length, height, and half of

the melt pool width. A schematic of a quarter-ellipsoid melt pool is shown in Figure 2.1. For constant process parameters, spatial flow rate, $\lambda(x) = \lambda_0$, and powder catchment efficiency, $\mu(x) = \mu_0$, an oblate quarter-ellipsoid melt pool results in the solidified bead shape illustrated in Figure 2.1, whose cross-section a is an ellipse. By relating the experimentally observed solidified bead morphology to known constant processes parameters the corresponding analytical expression for the dynamic kernel f_s can be determined as outlined next.

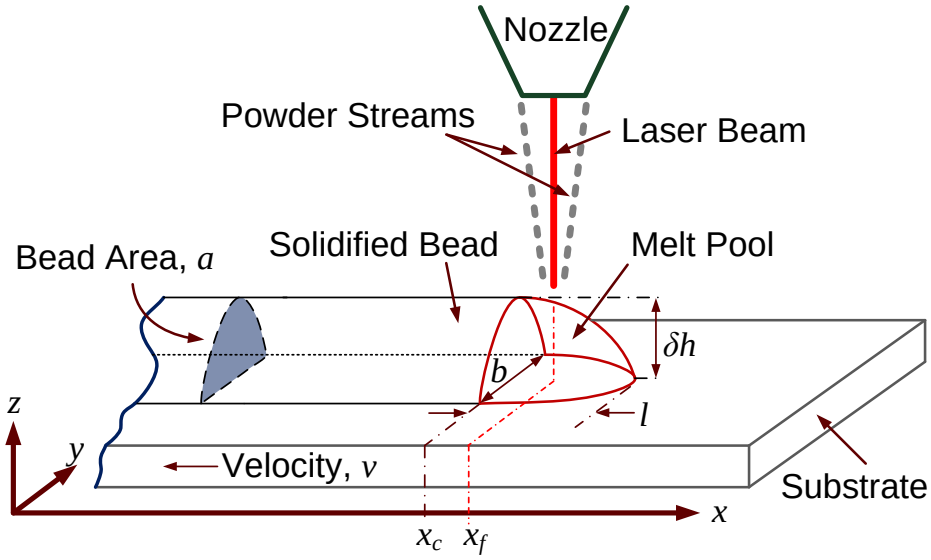

Figure 2.1. Laser metal deposition process schematic.

An oblate ellipsoid, centered at the tuple $(x_c, 0, 0)$ with principle radii length l (mm), half of the bead width $b/2$ (mm), and height δh (mm), is,

$$\left(\frac{x-x_c}{l}\right)^2+\left(\frac{2y}{b}\right)^2+\left(\frac{z}{\delta h}\right)^2=1 \tag{16}$$

where x_c is the ellipsoid center (mm), y is the horizontal axis perpendicular to the direction of deposition, and z is the vertical axis perpendicular to the direction of deposition. Similarly, the elliptical cross-section of the solidified bead in the direction of deposition is described by,

$$\left(\frac{2y}{b}\right)^2+\left(\frac{z}{\delta h}\right)^2=1. \tag{17}$$

Thus, the *y*-*z* plane cross-sectional area of an elliptical bead in Figure 2.1 is,

$$a(x)=\begin{cases}\dfrac{\pi}{4}b\delta h & x<x_c+\delta \\ \dfrac{\pi}{4}b\delta h\left[1-\left(\dfrac{x-x_c}{l}\right)^2\right] & x_c+\delta\le x\le x_c+l+\delta \\ 0 & x>x_c+l+\delta\end{cases} \tag{18}$$

where x_f is the position of the laser and powder focus (mm) and $\delta = x_f - x_c$ is the lead of the melt pool ahead of the coaxial laser beam and powder stream focus (mm). With constant process inputs, the differential volume dV is constant and equal to the steady-state cross-section of the elliptical bead, or,

$$\mathrm{d}V(x) = \begin{cases} \frac{\pi}{4} b\delta h, & x \le x_f \\ 0, & x > x_f \end{cases}. \tag{19}$$

Remark 2.1: Certain combinations of process parameters may cause the melt pool to spatially lead (i.e., $\delta < 0$) the laser position more than others [Picasso 1994]. While some melt lead is expected in normal processing conditions, a large melt pool lead can be indicative of excessive superheat which can negatively affect final material properties [Srivastava 2001].

It remains to find the morphology kernel, f_s that relates the steady-state input (19) to the observed steady-state output (18), while also adhering to the constraints in (13) and (14). It can be verified that the only function that satisfies these requirements is,

$$f_s(x) = \begin{cases} \frac{2}{l^2}(x-\delta), & \delta \le x \le l+\delta \\ 0, & \text{otherwise} \end{cases}. \tag{20}$$

Remark 2.2: Recognizing that the laser focal point must intersect the melt pool, the spatial lead δ must be strictly less than the melt pool length l. It is interesting to note that this constraint always results in f_s support on the negative axis, and therefore, the LMD process is noncausal along the spatial axis, x.

2.3. POWDER CATCHMENT MODEL

Powder catchment efficiency, the ratio of the amount of powder captured by the melt pool to the amount of powder delivered from the powder delivery system, is typically modeled as a function of the distance between the melt pool and the nozzle [Lin 1999]. Thus,

$$\mu(x) = f_{\mu}\left(d_P(x)\right) \tag{21}$$

where d_p is the distance from the nozzle to the part (mm), as shown in Figure 2.2, and f_{μ} is a static powder distribution function. Typical powder distribution profiles for commercially available systems are Gaussian in shape, resulting from the convergence of individual powder streams to a single focal point, c.f. [Lin 1999] and the photograph of a commercial LENS print head in Figure 2.3. Therefore, the powder catchment profile is modeled as,

$$f_{\mu}\left(d_P(x)\right) = \frac{\alpha_{max}}{100}\exp\left[-\left(\frac{\left(d_P(x) - d_{max}\right)}{\alpha_{width}}\right)^2\right] \tag{22}$$

where α_{max} is the maximum powder catchment (%), d_{max} is the distance from the nozzle to the maximum powder catchment (mm), and α_{width} is the powder catchment characteristic width (mm).

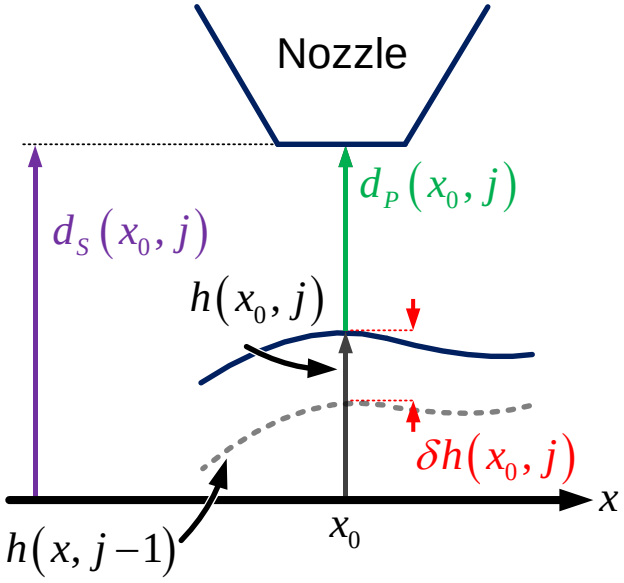

Figure 2.2. Schematic of nozzle-part interaction zone with substrate standoff d_S, part standoff distance d_P, bead height δh, and part height h.

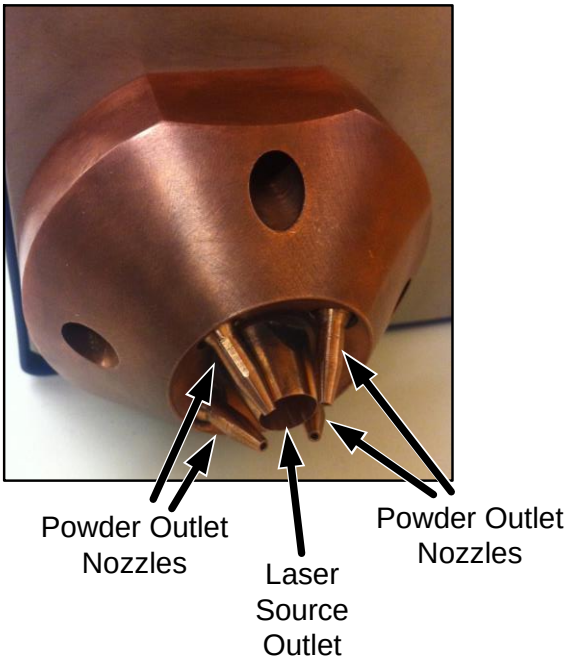

Figure 2.3. Photograph of an Optomec LENS Print Engine Head.

2.4. LAYER-TO-LAYER MODEL

In multi-layer part fabrications, the previous layer becomes the foundation for the current layer; thus, coupling the in-layer dynamics of the previous layer to those of the current layer and creating a two-dimensional dynamic system. Let the part height h (mm) at position x and layer j be given by $h(x,j)$ and let the height of the substrate be defined as $h(x,0) = 0$ such that the first layer added to the substrate is layer $j = 1$. Let d_S, the distance from the substrate to the nozzle (mm) as shown in Figure 2.2, be generated by a layer-to-layer integration process

$$d_S(x, j) = d_S(x, j-1) + \delta d_S(x, j) \tag{23}$$

where δd_S is the incremental layer-to-layer substrate standoff distance (mm). Then, the part standoff distance d_P (mm) at layer j is,

$$d_P(x, j) = d_S(x, j) - h(x, j-1). \tag{24}$$

As the melt pool in the current layer moves over the previously fabricated layer, dilution occurs, re-melting and redistributing material from the previous layer or layers [Kang 1995, Wang 1998]. As the re-melting process is an extension of the melt pool into the previous layers, it is governed by complex flow phenomena similar to the in-layer dynamic process. Therefore, the locally linear re-melt dynamics may be described with a convolution kernel, similar to the morphology kernel in Section 2.2. Let kernel describing these dynamics, the re-melt kernel, be defined as f_r. Then, the re-melted

height h_{remelt}, the previously built part height which has undergone re-melting, can be written as,

$$h_{remelt}\left(x, j-1\right) = h\left(x, j-1\right) * f_r\left(x\right) \tag{25}$$

where $\left(\bullet\right)*\left(\bullet\right)$ represents the convolution operation of the arguments. As with the morphology kernel, the re-melt kernel is constrained by the law of mass conservation,

$$\int_{-\infty}^{\infty} f_r\left(x\right)\mathrm{d}x = 1,\ f_r\left(x\right) \geq 0,\ \forall x. \tag{26}$$

However, unlike the morphology kernel, in which the melt pool is constrained on one side by the solidified bead, but free to flow in front of the solidified bead, the re-melt flow of the previous layer is bounded on both sides by solid material. Thus, it is reasonable to further assume that the re-melt kernel is symmetric and therefore, two additional constraints are added to the re-melt kernel description,

$$f_r\left(x\right) = f_r\left(-x\right)$$

$$f_r\left(x\right) = 0,\ \forall \left|x\right| > l_r$$

where l_r is the re-melt process characteristic length (mm). A kernel which satisfies the above constraints is

$$f_r(x) = \begin{cases} \frac{1}{l_r} - \left|\frac{x}{l_r^2}\right| & -l_r \le x \le l_r \\ 0 & \text{otherwise} \end{cases} . \quad (27)$$

A more detailed analytical description of the linear profile re-melt kernel is explored in the system identification experimental results in Section 3.4.

Noting the height of the part above the substrate on a given layer j and at a position x is the sum of the previous part height and the current bead height, a direct result of the mass conservation constraints on f_s and f_r, $h(x, j) = \delta h(x, j) + h_{remelt}(x, j-1)$, and combining (15) and (25), the two-dimensional LMD height dynamics are,

$$h(x, j) = \underbrace{b^{-1} \varsigma f_\mu \left(d_S(x, j) - h(x, j-1) \right) \lambda(x, j) * f_s(x)}_{\text{Melt Pool Dynamic}} + \underbrace{h(x, j-1) * f_r(x)}_{\text{Re-Melt Dynamic}} . \quad (28)$$

Equation (28) represents the two-dimensional, repetitive process description of LMD where the incremental substrate standoff distance δd_S (whose layer-to-layer integration gives d_S as in (23)) and the powder spatial flow rate λ are process inputs, and h is the process output.

2.5. GENERAL TWO-DIMENSIONAL AM PROCESS MODEL

Casting the two-dimensional model presented in (28) into a general modeling framework enables insight into the structure of the process. Because the LMD process is not a particularly special example of AM processes, it is reasonable to assume that the

structure of the LMD model presented above is applicable to many other AM processes. Here, the general framework is that presented in (9). For other freeform AM process such as Glass AM [Luo 2014], Freeze-form Extrusion Fabrication (FEF) [Deuser 2013] and Fused Deposition Modeling (FDM) [Wales 1991], the individual model blocks G_1, f, and G_2 are similar to those of LMD, i.e., a melting and solidification process occurs; therefore, little change to the model is needed in order to describe these processes. Further, the model described above may be applied to material bed processes, such as Selective Laser Sintering (SLS) [Deckard 1986] or Stereolithography (SLA) [Hull 1988], and possibly ink jet processes.

The re-melt process described by f_r in Section 2.4 can be generalized to the concept of re-treatment for other AM processes. Here, re-treatment refers to an energy exchange between the previous material and the current layer, i.e., re-melting in the case of LMD, FEF, FDM, and SLS or over-curing in SLA [Melchels 2010]. It is reasonable to assume these dynamic processes can be captured by the filtered feedthrough of the previous part height for each specific AM process.

To demonstrate how the LMD process model (28) fits the form of (9), consider the input and output signals, **u** and **y**, respectively, as,

$$\begin{aligned} \mathbf{u}(x,j) &= \begin{bmatrix} \delta d_S(x,j) & \lambda(x,j) \end{bmatrix}^T \\ \mathbf{y}(x,j) &= h(x,j) \end{aligned} . \tag{29}$$

Now, consider the layer-to-layer dynamic block G_1 containing the substrate standoff distance integration process (23),

$$d_S(x,j) = \frac{1}{\left(1-w^{-1}\right)}\delta d_S(x,j), \tag{30}$$

and the layer-to-layer delay on the feedback channel $w^{-1}h(x,j) = h(x,j-1)$, as,

$$G_1(w) = \begin{bmatrix} 1 & 0 & 0 \\ 0 & \dfrac{1}{1-w^{-1}} & -w^{-1} \\ 0 & 0 & w^{-1} \end{bmatrix}, \tag{31}$$

with intermediate states,

$$\mathbf{\upsilon}(x,j) = \begin{bmatrix} \lambda(x,j) & d_P(x,j) & h(x,j-1) \end{bmatrix}^T. \tag{32}$$

Also, consider the static nonlinearity as,

$$f\left(\mathbf{\upsilon}(x,j)\right) = \begin{bmatrix} b^{-1}\varsigma f_\mu\left(\upsilon_2(x,j)\right)\upsilon_1(x,j) \\ \upsilon_3(x,j) \end{bmatrix}, \tag{33}$$

where υ_i for i = 1,2,3 is the i^{th} element of $\mathbf{\upsilon}$. The outputs of the static nonlinearity are then $\xi(x,j) = \begin{bmatrix} b^{-1}\mathrm{d}V(x,j) & h(x,j-1) \end{bmatrix}^T$. Finally, consider the in-layer dynamic operator G_2 as,

$$G_2(s) = \begin{bmatrix} F_s(s) & F_r(s) \end{bmatrix} \tag{34}$$

where F_s and F_r are the frequency domain representations of f_s and f_r, respectively. Then, it can be verified that the Linear-Nonlinear-Linear two-dimensional structure, (9), with (29), (31), (33), and (34) describes the LMD process, (28).

3. MODEL IDENTIFICATION METHODOLOGY

In general, identification of a two-dimensional dynamic system is not a trivial task due to the potential coupling between the two sets of dynamics. Here, the coupling between the in-layer and layer-to-layer dynamics is eliminated through careful experimental design that divides the overall identification problem into several, more tractable, identification problems. The two-dimensional model presented in (27) is composed of three sets of model parameters that need to be identified; the powder catchment efficiency model f_μ parameters (22), the in-layer dynamic parameters which include area-to-height relationship b and the linear dynamic shaping process f_s parameters (15) and (20), respectively, and the linear dynamic re-melting process f_r function (27). From Figure 1.4 and the structure of the general AM repetitive process model (9), it can be seen that the elements of G_2, f_s and f_r, can be identified by exciting $\boldsymbol{\upsilon}$ and measuring the process output $\mathbf{y}$. For LMD, in-process measurement of $\boldsymbol{\xi}$ is difficult, and therefore the process of identifying the static nonlinearity, f, is performed with slowly-changing inputs $\boldsymbol{\upsilon}$, so as not to excite the in-layer dynamic, G_2.

3.1. EXPERIMENTAL SETUP

The LMD system used for the experiments conducted in this work is a commercially available Optomec LENS® MR-7 with an Optomec K-Head attached. The Optomec LENS® MR-7 consists of three computer controlled axes – an x-y table and a z-axis gantry – capable of ±0.25 mm positioning accuracy mounted inside a hermetically sealed Class I Laser Enclosure. The powder is delivered by an Optomec powder feeder and the laser source is a 500 W IPG Fiber Laser. The bead profile is measured with a

Keyence LK-H052 laser displacement sensor mounted on a separate CNC machine – a GE/FANUC-controlled Fryer 5-Axis machine tool. Measurements are acquired by scanning the laser displacement sensor over the part. The sensor averages a measurement profile over a circular 50 μm diameter spot at a standoff distance of 50 mm with a resolution of 1 μm. Using a sensor temporal sampling rate of 400 μs and a table velocity of 5.080 mm/s (12 IPM) yields a spatial sampling rate of 492 samples/mm. Experiments are conducted using 316L Stainless Steel powder on stainless steel substrates.

3.2. POWDER CATCHMENT EFFICIENCY MODEL

Here, an experiment is constructed to generate internal signals of the form, $\boldsymbol{\upsilon}(x,1)=\begin{bmatrix}\lambda_0 & d_P(x,1) & h(x,0)\end{bmatrix}$ where λ_0 is constant spatial flow rate, in order to identify the powder catchment efficiency model, f_μ. The conservation of mass constraints on the shape and re-melt kernels, (13) and (26), respectively, ensures that G_2 has low-frequency pass-through with a DC gain of 1, or $y(x,1)\approx b^{-1}\lambda_0 f_\mu\left(d_P(x,1)\right)+h(x,0)$ for signals $d_P(x,1)$ and $h(x,0)$ whose in-layer frequency content is concentrated at low frequencies. To generate the required internal signal $\boldsymbol{\upsilon}$, a wedge-shaped substrate, shown in Figure 3.1, is used with constant spatial flow rate. The powder catchment efficiency function is determined by relating the known spatial flow rate and measured bead width to the measured bead height.

Two separate powder flow rates, $\dot{m}$ = 5.6 g/min and $\dot{m}$ = 9.2 g/min, which are denoted Trial 1 and 2, respectively, are used for identification of f_μ. Powder flow rates are determined by setting the powder feeder motor speed, collecting powder for 1 min, and weighing the resulting powder output. The powder feeder motor speeds were set to 3

RPM and 5 RPM for Trials 1 and 2, respectively. The total deposition length was 101.6 mm, with an initial standoff distance of $d_P(0,1)$ = 13.97 mm at the low end of the wedge (the right side in Figure 3.1) and minimum standoff distance of $d_P(101.6,1)$ = 2.54 mm at the high end of the wedge (the left side in Figure 3.1). The inclination of the substrate, 5.71° above horizontal, allows the standoff distance to vary continuously and linearly during the deposition. The laser power was Q = 450 W and the scan speed was v = 8.47 mm/s. These process parameters are typical for 316L Stainless Steel deposition on the Optomec LENS® MR-7 system. The other depositions shown in Figure 3.1 correspond to two other powder flow rates. The data from these tests are given in Appendix B.

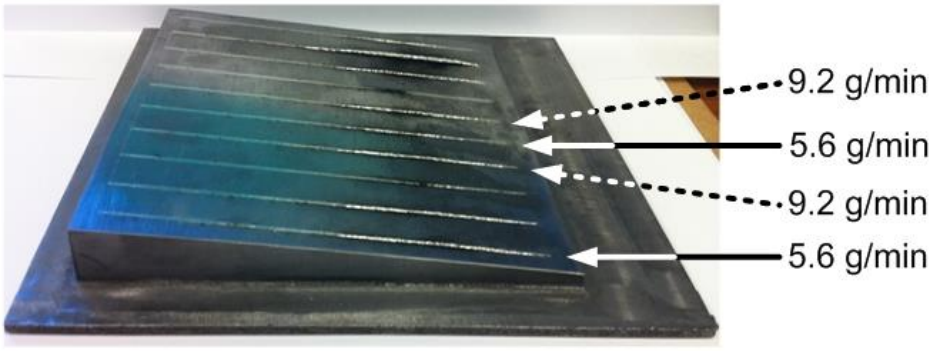

Figure 3.1. Experimental results for identification of powder catchment function, f_μ.

The experimental results for Trials 1 and 2 are shown in Figure 3.2. Both powder flow rate tests visually produce a similar powder catchment shape in this region of the parameter space. At the typical standoff distance for an Optomec LENS® MR-7 system,

d_P = 9.53 mm, the powder catchment efficiency is approximately 12% for both powder feeder motor speeds.

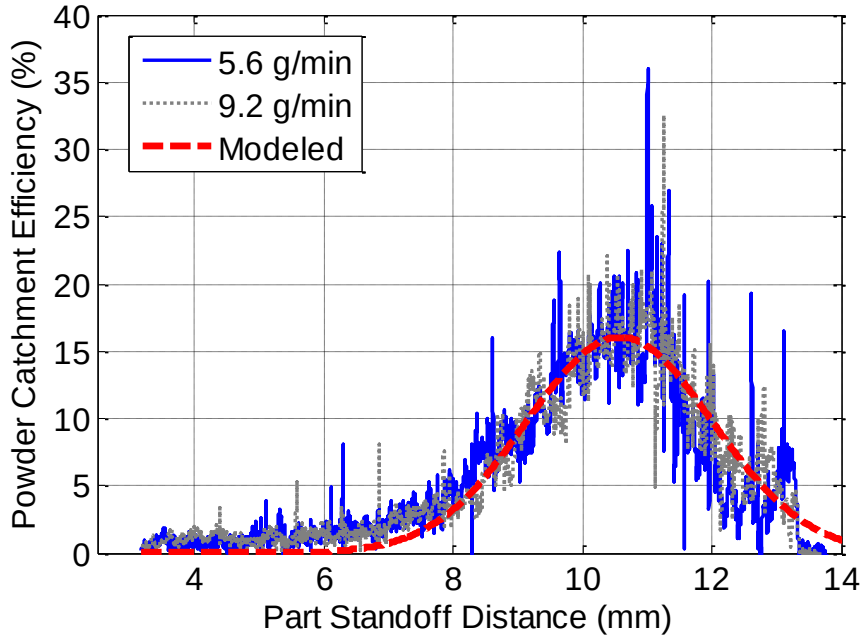

Figure 3.2. Modeled and experimental powder catchment efficiencies.

The Trial 2 data is used as the identification data while the Trial 1 data is used for validation. Minimizing the Root Mean Squared Error (RMSE) between the model and the measured data yields a RMSE of 1.71% for the identification data set and 2.40% for the validation data set, indicating good agreement between the model and the experimental system. The identified model parameters are α_{max} = 16.04%, d_{max} = 10.57 mm, and α_{width} = 2.04 mm, and the resulting model powder catchment efficiency is plotted along with the measured powder catchment efficiencies in Figure 3.2.

3.3. IN-LAYER DYNAMIC PROCESS AND BEAD WIDTH

In the derivation of the morphology kernel given in (20), two parameters are used to determine the function: a characteristic melt pool length l and a melt pool lead δ. The in-layer dynamic and characteristic bead width are identified with input signals of the form $\mathbf{v}(x,1) = \begin{bmatrix} \lambda(x,1) & d_{P,0} & h_0 \end{bmatrix}^T$ where $d_{P,0}$ and h_0 are in-layer constant part standoff distance and part height, respectively. Similar to the previous subsection, the mass conservation constraints on f_r (26) ensure that f_r has low-frequency pass-through with a DC gain of 1, or $y(x,1) \approx b^{-1}\lambda(x,1)\, f_\mu(d_{P,0}) * f_s(x) + h_0$ for low in-layer frequency h_0. Because constant part standoff distance $d_{P,0}$ contributes a constant powder catchment efficiency, which is identified in the previous subsection, the powder catchment efficiency, $f_\mu(d_{P,0})$, is taken as a known quantity. Here, the velocity component of the spatial flow rate, λ, is the channel used to excite the in-layer dynamic process because of the large bandwidth of the motion stage relative to the powder feeder system. Holding powder flow rate and laser power constant at the same levels given in the previous section, Pseudo-Random Binary Sequences (PRBSs) are commanded on the velocity channel and the resulting bead height is measured. Pseudo-Random Binary Sequences are commonly employed in system identification and consist of a set of step inputs with equal magnitudes but varying durations [Godfrey 1993, Eskinat 1991].

Alignment of the commanded velocity and the measured deposition in the spatial domain is critical since any error in the starting positions is directly interpreted as a spatial delay, corrupting the model fit. Therefore, in order to facilitate proper alignment of the velocity signal and the measured deposition, a 50 μm edge radius witness mark is machined into the substrates and the start of deposition (i.e., start of laser emission) is

delayed 0.5 seconds, hard-coded into the motion commands sent to the MR-7 (given in Appendix A), after the velocity profile starts. In doing so, the witness mark is clearly visible and undistorted when measuring the height profiles. This is schematically shown in Figure 3.3.

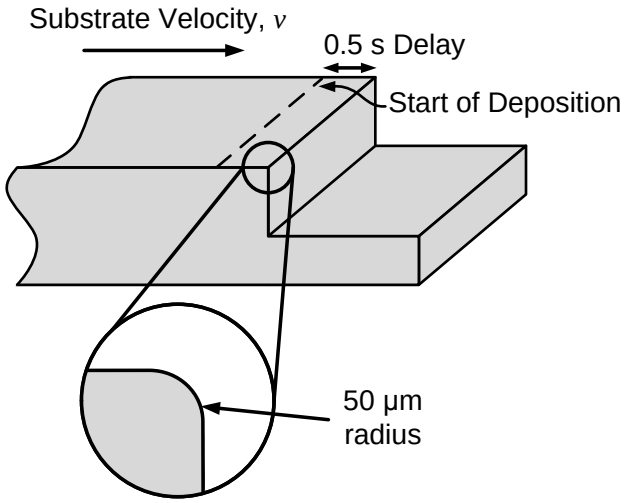

Figure 3.3. Schematic of witness mark and delayed deposition for alignment of commanded velocity and measured bead height for in-layer kernel identification.

The measured bead height and the commanded velocity are used in conjunction with a derivative-free nonlinear optimization algorithm implemented in Matlab to identify the bead width, length and shifting parameters, b, l and δ, respectively.

The step inputs are selected to excite dynamics around the nominal velocity of v = 8.5 mm/s. A low value of v = 4.2 mm/s and a high value of v = 12.7 mm/s are used, representing the typical speed range within which the Optomec LENS® MR-7 system is operated for 316L Stainless Steel. The commanded PRBS velocity profiles used for both

the identification and validation trials are shown in Figure 3.4. Two separate single layer trials were conducted with the same velocity profile; one with a powder flow rate $\dot{m}$ = 5.6 g/min and the second with a powder flow rate $\dot{m}$ = 9.2 g/min, corresponding to Trials 1 and 2, respectively, detailed in the previous subsection. Both trials were made using a commanded laser power of Q = 450 W and a standoff distance of $d_P(x,1)$ = 9.53 mm for x = 0 mm to x = 75 mm.

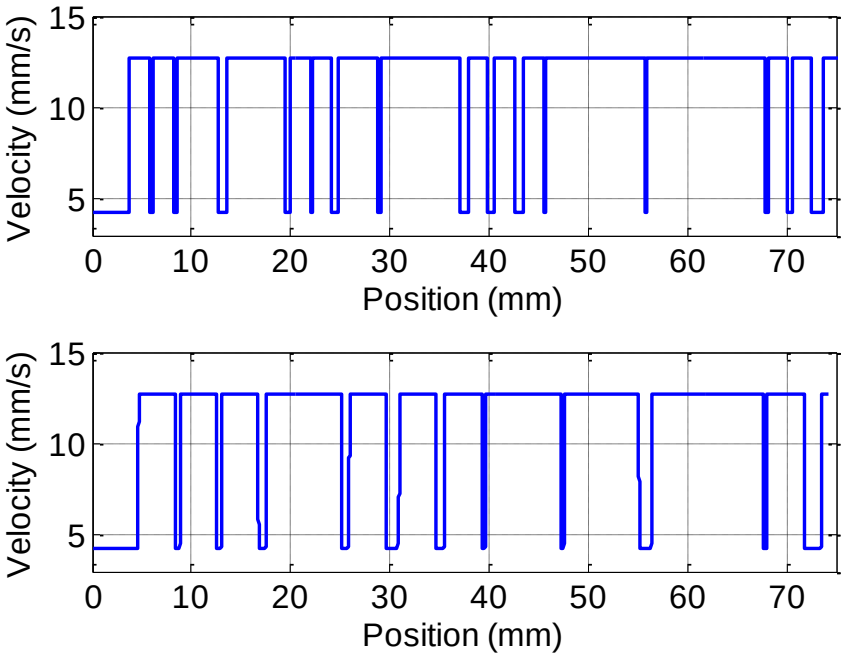

Figure 3.4. Commanded identification (top) and validation (bottom) PRBS velocity signals.

For Trial 1, where $\dot{m}$ = 5.6 g/min, the identified characteristic width, length, and shifting parameters were b = 1.03 mm, l = 0.503 mm, and δ = -0.012 mm, respectively. For Trial 2, where $\dot{m}$ = 9.2 g/min, the identified characteristic width, length, and shifting

parameters were b = 0.836 mm, l = 0.610 mm, and δ = -0.010 mm, respectively. Figures 3.5 and 3.6 show the measured bead height as a function of position for both the identification and validation tests for Trials 1 and 2, respectively, in addition to the model using the identified parameters for the respective trials. For both trials, the shifting parameters are nearly at the level of the velocity stage incremental displacement command and physically correspond to a melt pool that is centered well under the nozzle in the direction of deposition. Further, the length of the two melt pools coincide very closely with the predicted laser beam spot size, between 0.36 mm and 0.64 mm as calculated from the Optomec laser and optics settings, indicating a good balance between incident energy from the laser and bead volume. The RMSEs of the identification and validation data for Trial 1 and Trial 2 are given in Table 3.1. While the RMSE levels are smaller for Trial 1, the validation data indicates very good agreement between the model and the physical process for both trials.

Table 3.1. Identification and validation RMSE and percent error for Trials 1 and 2.

Trial Number	**Identification RMSE**	**Validation RMSE**	**Error (%)**
1	0.073	0.078	6.85
2	0.143	0.147	2.80

As stated above, at the beginning of the identification and validation sets, deposition is intentionally delayed in order to facilitate the alignment of the commanded velocity profiles and the measured height profiles. This delay contributes to the fitting error seen at the beginning of the responses in Figures 3.5 and 3.6. Additionally, the

overshoot observed in the measured responses at the beginning of the identification and validation sets and at the end of the validation sets is due to un-modeled process startup and end effects. The measurement spikes seen in Figure 3.5, and in particular Figure 3.6 at x = 42 mm in the top plot and at x = 55 mm in the bottom plot, are a result of the laser displacement sensor incident upon individual or small agglomerates of powder particles causing the laser to be reflected in a direction oblique to the feature and sensor head. This phenomenon causes measurement artifacts or data dropout.

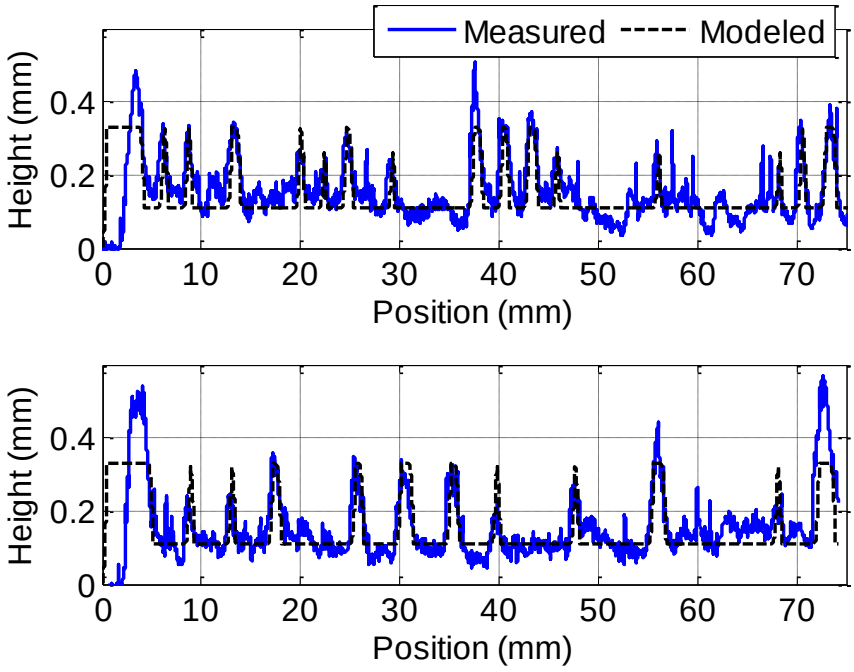

Figure 3.5. Modeled and measured bead height signals for Trial 1 identification (top) and validation (bottom).

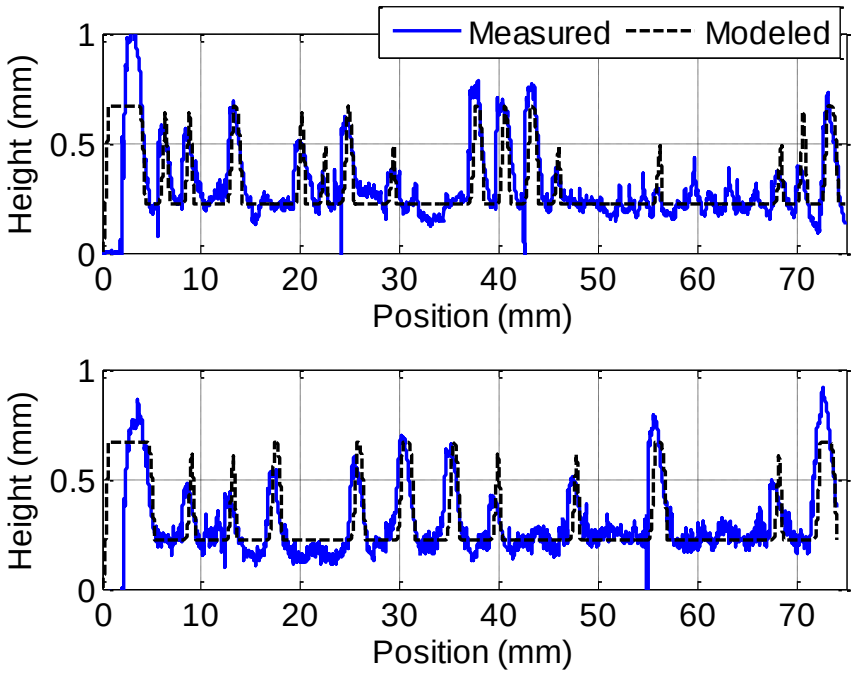

Figure 3.6. Modeled and measured bead height signals for Trial 2 identification (top) and validation (bottom).

3.4. RE-MELT DYNAMIC PROCESS

As detailed in Section 2.5, the re-melt dynamic process is excited by the height profile on the single previous layer; therefore, an internal signal of the form $\boldsymbol{\upsilon}(x,1)=\begin{bmatrix}\lambda_0 & d_{P,0} & h(x,0)\end{bmatrix}^T$, with $h(x,0)$ as the excitation source, is used here for identification. The mass conservation constraint on f_s, (13), ensures low-frequency pass-through with unity DC gain and, by constraining $h(x,0)$ to small magnitude variations, ensures the change in powder catchment efficiency is also small. Then, the process dynamics simplify to $y(x,1)\approx b^{-1}\lambda_0 f_\mu(d_{P,0})+h(x,0)*f_r(x)$ for low in-layer frequency signals λ_0 and $d_{P,0}$. Similar to the identification of f_s, an excitation signal in the form of a PRBS on the previous layer height profile is used to identify f_r. This signal is

constructed by a Wire Electric Discharge Machining (Wire-EDM) operation to precisely shape a stainless steel substrate containing a PRBS signal. The error between the modeled and measured height is minimized with respect to the re-melt model parameters, detailed below, to identify the re-melt kernel.

Two separate step heights are used; the first corresponding to the average bead height of Trial 1, 0.20 mm, and a second corresponding to the average bead height of Trial 2, 0.45 mm. The process parameters were set to Q = 450 W, v = 8.47 mm/s, and d_P = 9.53 mm for all x. Again $\dot{m}$ = 5.6 g/min for Trial 1 and $\dot{m}$ = 9.2 g/min for Trial 2. Single beads were deposited on the Wire-EDM PRBS substrates. Top and side views of the re-melt dynamic process identification substrates, before and after deposition, are shown in Figures 3.7 and 3.8, respectively.

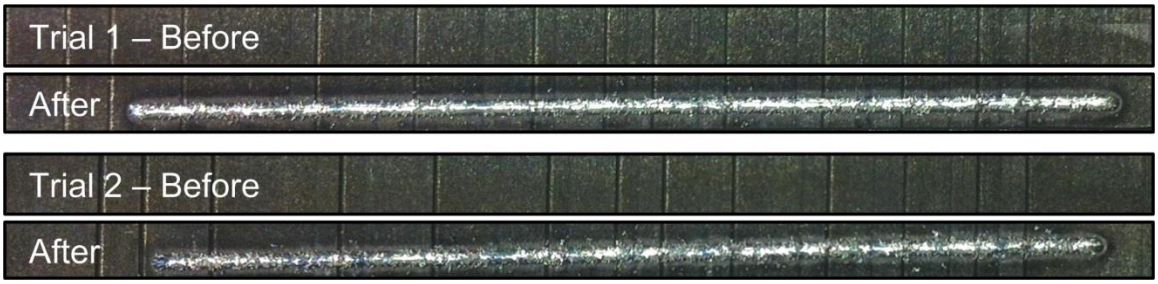

Figure 3.7. Top view of re-melt dynamic process identification substrates before and after deposition for Trial 1 (top) and Trial 2 (bottom).

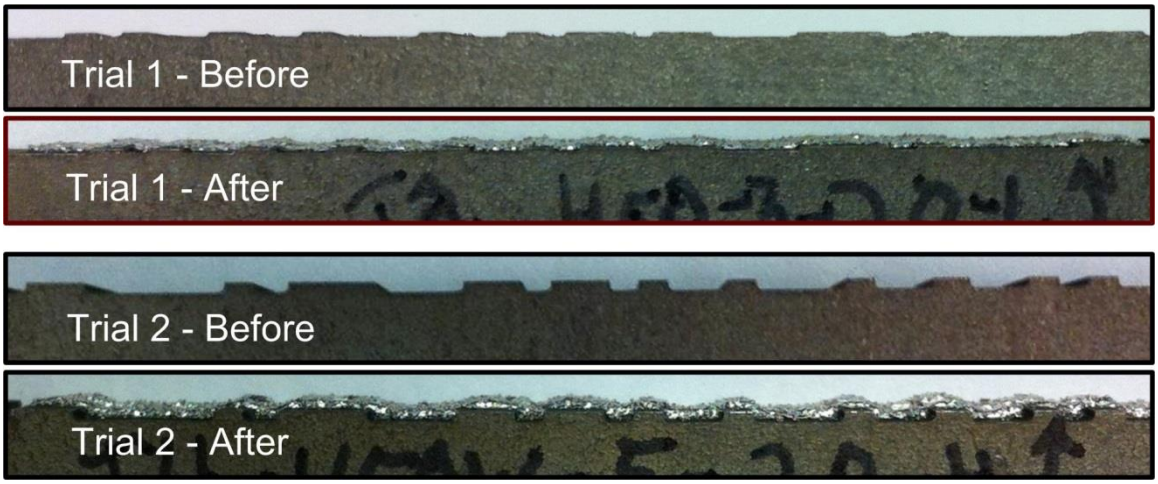

Figure 3.8. Side view of re-melt dynamic process identification substrates before and after deposition for Trial 1 (top) and Trial 2 (bottom).

As discussed in Section 2.4, the re-melt function, f_r, should be symmetric, positive, and have unit area (26). A function satisfying these requirements is given in (27) and is validated in the following exposition.

The characteristic length parameter for Trials 1 and 2 yields the re-melt characteristic lengths l_r = 0.903 mm and l_r = 1.21 mm, respectively. Figures 3.9 and 3.10 show the measured and modeled re-melt responses in addition to the measured substrate heights before deposition for Trials 1 and 2, respectively. The measurement spikes seen in both Figures 3.9 and 3.10, e.g., at x = 26 mm in the upper plot in Figure 3.10, are the result of the sensor effects described in the previous subsection.

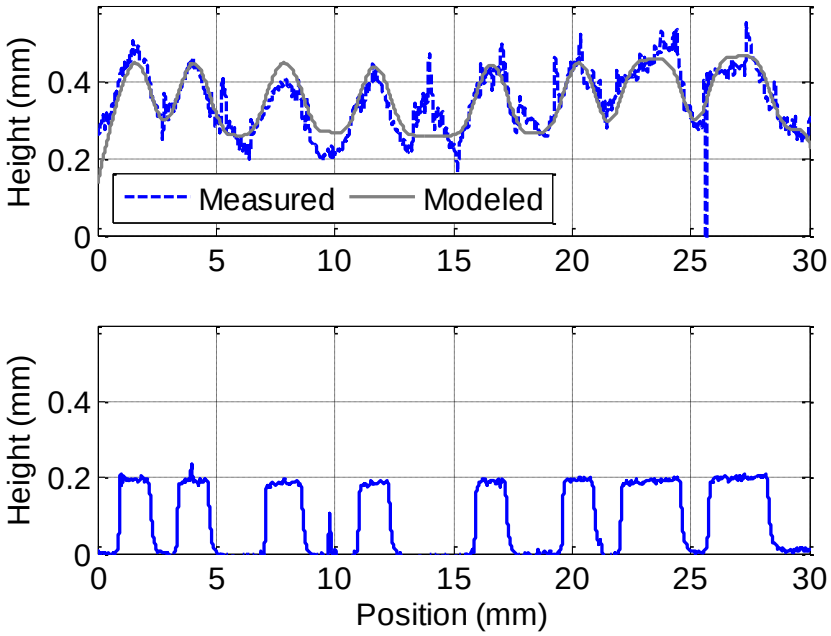

Figure 3.9. Measured and modeled height due to re-melt response (top) and measured before-deposition substrate height (bottom) for Trial 1.

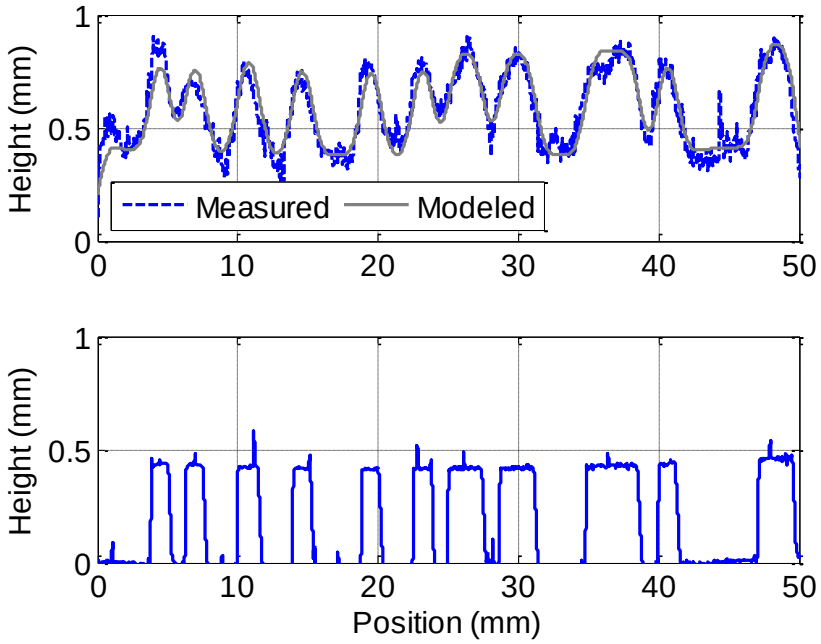

Figure 3.10. Measured and modeled height due to re-melt response (top) and measured before-deposition substrate height (bottom) for Trial 2.

An additional artifact appears around x = 14 mm in the top plot in Figure 3.10. While the exact cause of this is unknown, a test deposition was made immediately before and adjacent to the Trial 1 test on the same substrate. It is possible that a buildup of powder occurred on this section of the substrate causing the taller feature. Because this phenomenon is not seen at other locations within the same deposition nor in the Trial 2 deposition, it is reasonable to assume it is a product of process noise.

3.5. FREQUENCY DOMAIN CHARACTERISTICS

As will be demonstrated below in Section 4, the frequency domain characteristics of the kernels f_s and f_r play an important role in the layer-to-layer stability and the ability to control the process. Here, the general characteristics of f_s and f_r are presented and then the specific characteristics of these kernels, as applied to the LMD process, are presented.

3.5.1. General Frequency Domain Characteristics. The Laplace domain representations of f_s and f_r are, respectively,

$$F_s(s) = \frac{2\left(1-\left(1+sl\right)e^{-ls}\right)e^{-\delta s}}{s^2 l^2} \tag{35}$$

$$F_r(s) = \frac{e^{l_r s} + e^{-l_r s} - 2}{s^2 l_r^2}. \tag{36}$$

To examine the frequency domain properties, let $s = 2\pi i\omega_1$ in (35) and (36). When $\omega_1 = 0$, the magnitude of each kernel is unity. This is a direct consequence of the conservation of mass constraints detailed in Section 3.3 and 3.4. As $\omega_1 \to \infty$, the magnitude decays to

zero. Further examination yields the asymptotic magnitude roll of rate of (35) is -20 dB/decade due to the presence of a single zero and the two poles located at the origin. The frequency at which the magnitude of the in-layer shaping kernel F_s begins to roll of is equal to $\omega_1 = l^{-1}$. For the re-melt shaping kernel F_r, the asymptotic roll off rate is -40 dB/decade, because of the absence of any zeros in the kernel and the presences of two poles at the origin. The break frequency for F_r is located at approximately $\omega_1 = (2\pi l_r)^{-1}$ An interesting phenomenon associated with (36) is the zero magnitude associated with harmonics of $\omega_1 = k_r/l_r$ for $k_r = 1, 2, \ldots$. Plugging $\omega_1 = k_r/l_r$ for $k_r = 1, 2, \ldots$ into (36) gives,

$$\begin{aligned} \left|F_r\left(2\pi k_r/l_r i\right)\right| &= \left|\frac{e^{2\pi k_r i} + e^{-2\pi k_r i} - 2}{\left(2\pi\, k_r/l_r\, i\right)^2 l_r^2}\right| \\ &= \frac{\left|1+1-2\right|}{4\pi^2 k_r^2} \\ &= 0 \end{aligned} \tag{37}$$

Although not as clear from the frequency domain representations (35) and (36), the phase properties can also be determined. The clearest phase properties are associated with F_r. Because f_r is constrained to symmetric, it has zero phase for the entire frequency spectrum. For any ω_1, the argument of the lead component in F_r, i.e., $e^{l_r s}$, is exactly cancelled by the argument of the lag component, i.e., $e^{-l_r s}$.

Alternatively, the phase of f_s is zero near $\omega = 0$, but decreases to -180 degrees and continues to roll off as $\omega \to \infty$. The frequency at which the phase begins to decrease from zero is a function of the two parameters l and δ. In general, the phase roll off occurs approximately a decade before the frequency at which the magnitude begins to decay at a

rate of -20 dB/decade. When the shifting parameter $0 < \delta < l$, the frequency at which the phase starts to rapidly decrease due to the spatial delay is higher than the magnitude roll off frequency. In the case when $|l| > \delta < 0$, the phase loss is slower as this spatial delay adds phase after the frequency $\omega_1 = \delta^{-1}$. Figures 3.11 and 3.12 show the trend of the frequency response of F_s as the melt pool length l increases and the magnitude of the shifting parameter δ increases, respectively.

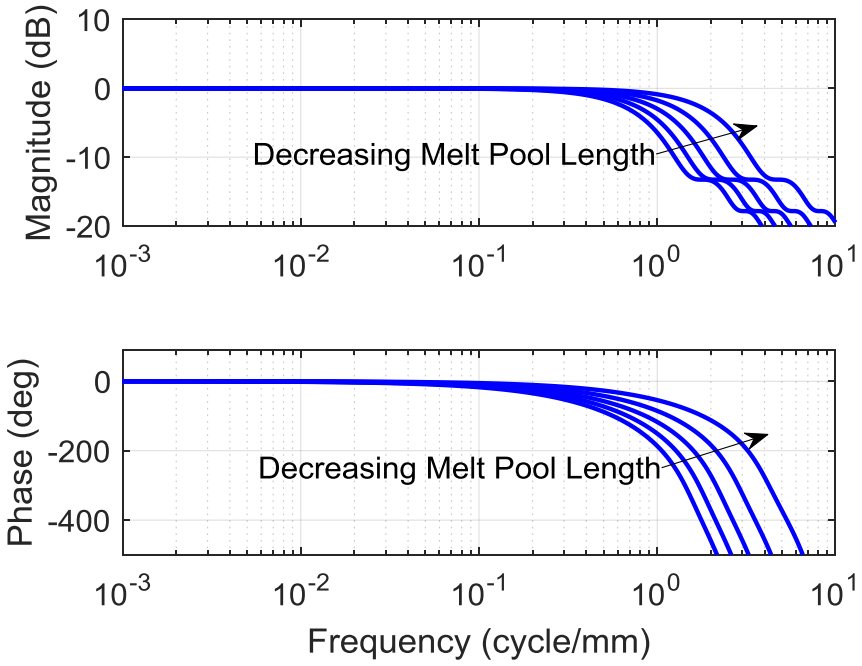

Figure 3.11. Bode diagram of F_s for increasing values of l with δ = -0.05 mm.

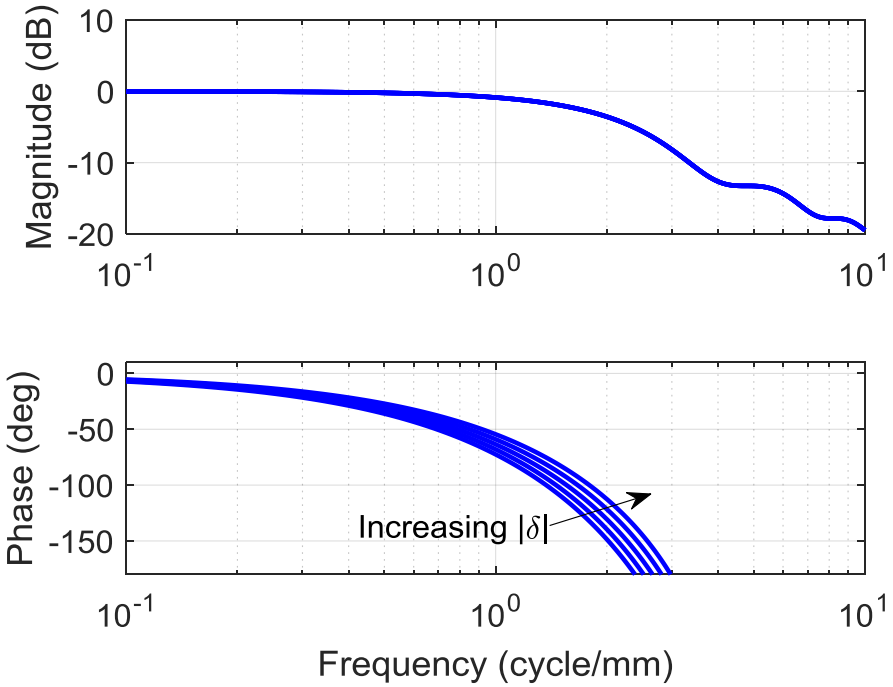

Figure 3.12. Bode diagram of F_s for increasing values of $|\delta|$ with l = 0.3 mm.

In Figure 3.11, it can be observed that the frequency at which the magnitude begins to roll off moves towards high frequencies as melt pool length decreases. The same behavior can be observed in the phase response, which begins its roll off approximately a decade before the corresponding magnitude decay. For the shifting parameter, it can be observed in Figure 3.12 that the magnitude response remains unchanged for any value of this parameter. However, the phase response moves towards zero phase as the magnitude of the shifting parameter increases.

3.5.2. Optomec Process Specific Frequency Domain Characteristics. Using the specific values of l, δ, and l_r for Trials 1 and 2 given above in Sections 3.3 and 3.4 in (35) and (36) and evaluating the frequency responses yields the Bode diagrams in Figure

3.13 and 3.14 for Trials 1 and 2, respectively. In both figures, the general trends detailed in Section 3.5.1 are present.

First, the unit magnitude of both kernels at DC is obvious. For f_s, the magnitude break frequency is positioned at the location of the melt pool length; ω_1 = 0.503 cycle/mm for Trial 1 and ω_1 = 0.610 cycle/mm for Trial 2. After this frequency, the magnitude for both trials follows the asymptotic -20 dB/decade attenuation. The phase response of both Trials 1 and 2 break from 0 degrees approximately 1 decade before the magnitude begins to roll off; ω_1 = 0.050 cycle/mm for Trial 1 and ω_1 = 0.06 cycle/mm for Trial 2.

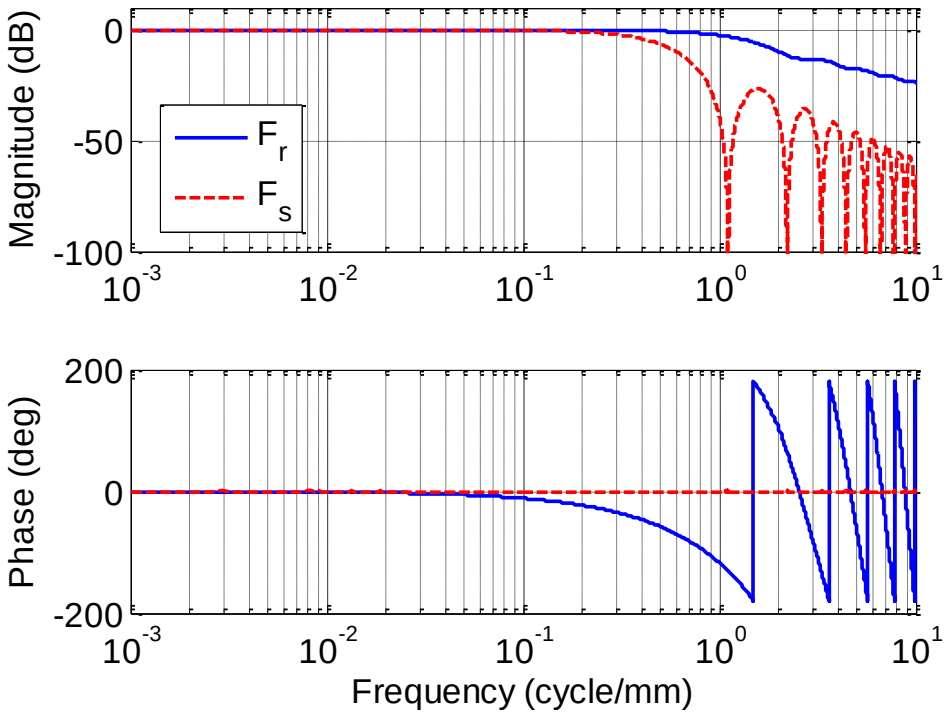

Figure 3.13. Bode diagram of the kernels f_s and f_r for Trial 1.

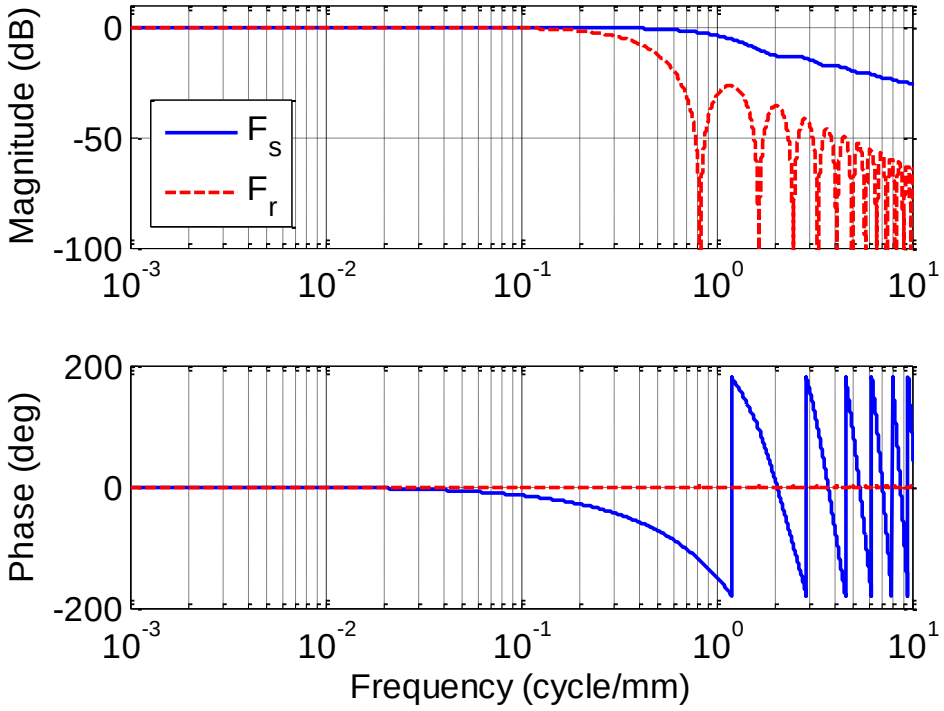

Figure 3.14. Bode diagram of the kernels f_s and f_r for Trial 2.

Again examining Figures 3.13 and 3.14, the zero phase response of the re-melt kernel is clear. Further, the magnitude begins the -40 dB/decade asymptotic attenuation when $\omega_1 = 1/2\pi l_r$. These frequencies are $\omega_1 = 0.176$ cycle/mm for Trial 1 and $\omega_1 = 0.132$ cycle/mm for Trial 2. As mentioned in the previous subsection, the magnitude drops rapidly when the spatial frequency is a harmonic of $\omega_1 = 1/l_r$.

3.6. TWO-DIMENSIONAL MODEL VALIDATION

3.6.1. Qualitative Frequency Domain Model Validation. While the PRBS tests performed in Section 3.3 successfully identify the in-layer shaping kernel parameters l and δ, it is not directly obvious that the LMD process performs as the frequency domain modeling demonstrates in Figures 3.11 and 3.12 in Section 3.5. An alternative way to identify the in-layer shaping kernel is through a series of sine wave excitations. Where each single track deposition is generated from a velocity profile which possesses a single in-layer frequency. While these depositions can be used for identification, they are time consuming. Therefore, instead of identification, these tests are used for qualitative validation purposes and are intended to demonstrate directly the frequency domain properties of the in-layer dynamic process.

The experimental setup for these tests is different from that of those performed in Sections 3.1 through 3.4. The experimental system consists of an IPG Photonics 1kW Ytterbium fiber laser, a Bay State Surface Technologies powder feeder, and an *x*-*y*-*z* motion stage actuated by stepper motors. The laser and powder feeder are regulated by their respective controllers while the motion stage is controlled by a National Instruments LabVIEW system. As with the tests conducted above, the resulting depositions are mounted on a Fryer machine tool and measured with a Keyence laser displacement sensor. The material used for these tests was H13 Tool Steel. Again, the substrates used for these tests have a 50 μm edge so that alignment of the deposition and the commanded velocity profile are reconcilable. The velocity profiles used here are of the form,

$$v(x,1) = \left(a_0 + a_1 \cos\left(2\pi\omega_1 x\right)\right)^{-1} \tag{38}$$

where a_0 is the constant offset of the cosine wave (s/mm) and a_1 is the amplitude of the cosine wave (s/mm). For each velocity profile, a_0 = 0.25 s/mm and a_1 = 0.2 s/mm. The velocity profile is an inverse cosine wave so that the resulting bead profile is sinusoidal. Due to system differences, i.e., different powder feeders, nozzles, materials, etc., for each trial below, the laser power was set to Q = 500 W and the powder feeder speed was set to 2.0 RPM. Further, because experimental tests have shown that the powder feeder used for the tests performed here is only accurate to within approximately 20% of the set point, the magnitude response is not reliable. Therefore, only the phase information of each trial is used for validation. Table 3.2 shows the frequencies used for the validation tests.

Table 3.2. Trial number and commanded velocity frequencies used for F_s characterization.

Trial	**Frequency ω_1 (cycle/mm)**
1	0.05
2	0.07
3	0.1
4	0.3
5	0.5
6	0.7
7	1.0

As mentioned above, the magnitude information of each trial is unreliable due to the large amount of uncertainty in the powder feeder motor speed. Because of this, a scaled version of the reciprocal of the velocity signal, with the correct phase, is shown in Figure 3.13 and 3.14. In addition to the scaled reciprocal velocity signal, the measured

bead height responses for each trial listed in Table 3.2 are shown in Figures 3.15 and 3.16.

Examining the behavior of the measured bead height responses as compared to the scaled reciprocal velocity signals, an obvious frequency-dependent trend emerges. At the lower frequencies shown in Figure 3.15, there is little to no spatial delay between the input signal, i.e., the velocity signal, and the output bead height. However, at the higher frequencies shown in Figure 3.16, a delay between the input and output signals appears at ω_1 = 0.3 cycle/mm and grows with increasing frequency.

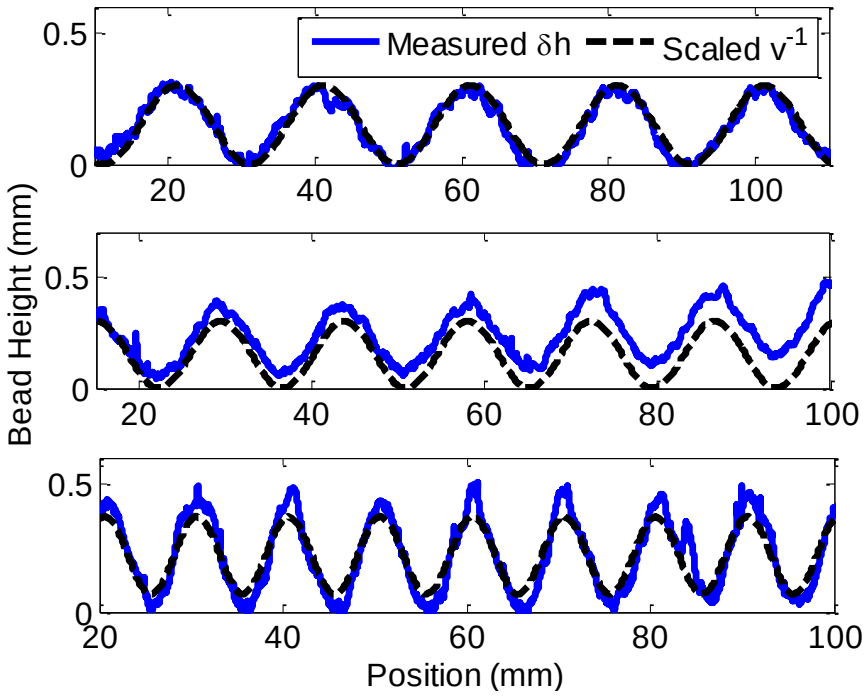

Figure 3.15. Spatial domain plot of measured bead height and scaled inverse velocity for ω_1 = 0.05 (top), 0.07 (middle), and 0.1 (bottom) cycles/mm.

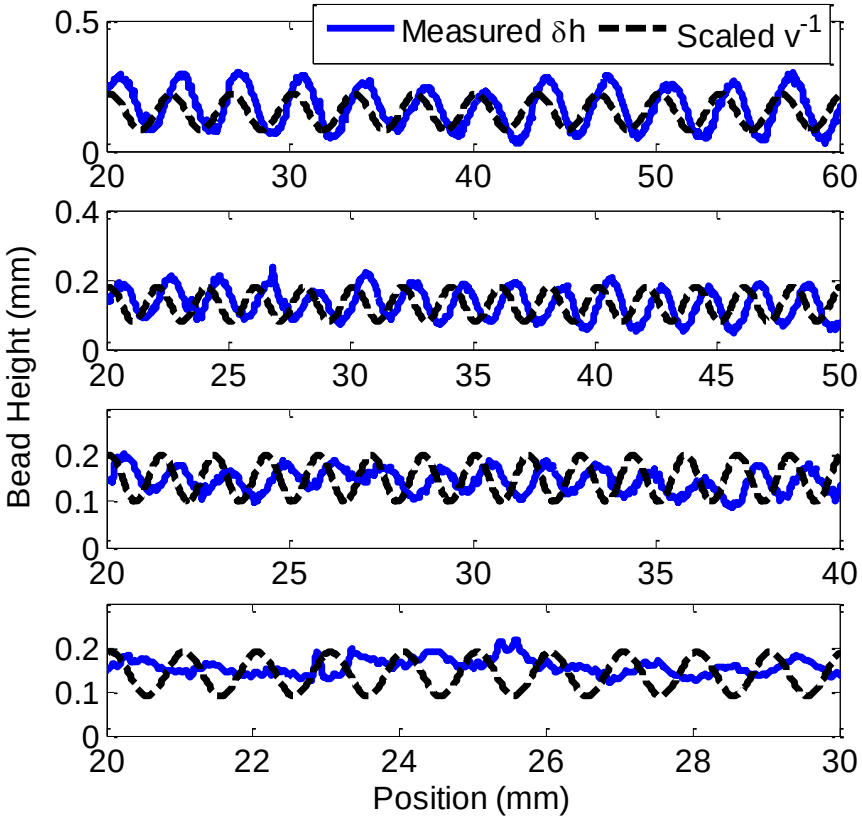

Figure 3.16. Spatial domain plot of measured bead height and scaled inverse velocity for (from top) ω_1 = 0.3 (first), 0.5 (second), 0.7 (third), and 1.0 (bottom) cycles/mm.

Using a cross-correlation technique [Knapp 1976], the spatial delay between the scaled reciprocal velocity and the measured bead height is calculated as,

$$\Delta_x(\omega_1) = \max_{\tau}\left[\frac{1}{L-\tau}\int_{\tau}^{L}\delta h_m(x)\,\mathrm{d}V(x-\tau)\,\mathrm{d}x\right] \tag{39}$$

where Δ_x is the calculated spatial delay (mm) of the test frequency ω_1, L is the total length of the measured deposit (mm), τ is a shifting parameter which ensures the best alignment of the two signals (mm), δh_m is the measured bead height (mm), and dV is the

scaled reciprocal input signal. Note, the spatial delay calculation on (39) does not depend on the magnitude of either signal. The phase delay for each response is then calculated as

$$\phi(\omega_1) = 360\omega_1\Delta_x \tag{40}$$

where ϕ is the calculated phase delay (deg) at frequency ω_1.

The spatial delays calculated for ω_1 = 0.05, 0.1, 0.5, and 1.0 cycle/mm are used to identify the melt pool length and shifting parameters l and δ, respectively, for the LMD system described above. The remaining calculated spatial delays are then used to validate the fit. The data is fit using a similar method to that described in Sections 3.3 and 3.4. Figure 3.17 shows the measured phase as well as the phase response of the modeled in-layer shaping kernel F_s. The melt pool length and shifting parameters for the system tested here were l = 1.13 mm and δ = -0.47 mm. While these values are larger than those identified for the Optomec process, there are several possible reasons for the discrepancy including material and process parameter differences. While the Optomec process parameters have been tuned specifically for the material used in those tests, the process parameters used for these test have not been optimized.

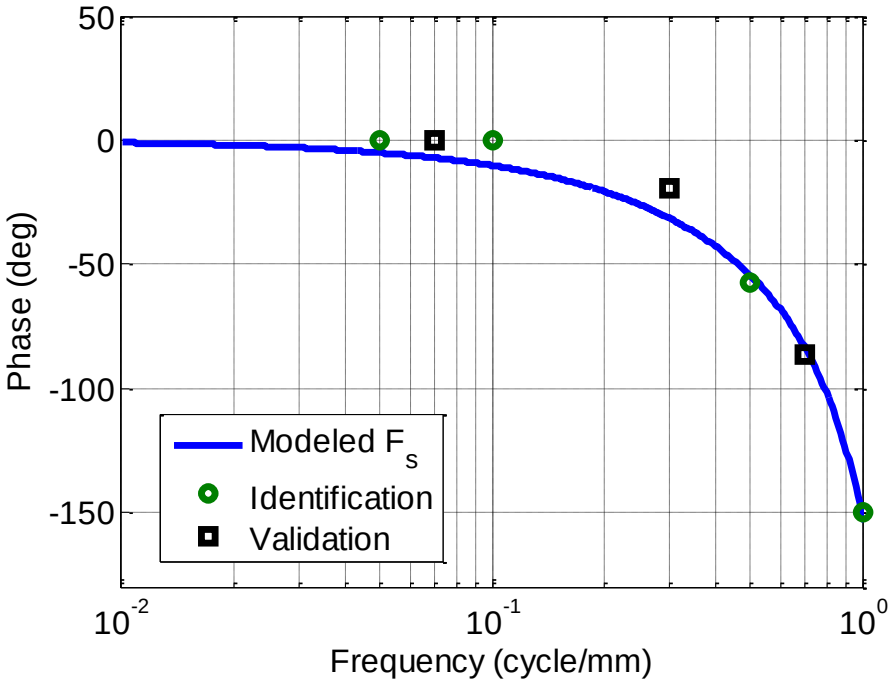

Figure 3.17. Phase plot of fitted convolution kernel f_s and experimentally determined phase lag.

Despite the differences explained above, examining the response in Figure 3.15, it can be observed that the phase of the modeled in-layer shaping kernel and the calculated phase delays agree well qualitatively with the phase response seen in the modeled processes in the previous subsection. Additionally, by examining the spatial domain responses in Figures 3.15 and 3.16, it is clear that the in-layer process is governed by a dynamic process whose phase properties change drastically over the frequency range ω_1 = 0.1 to ω_1 = 1 cycle/mm. The spatial domain delay and the phase response serve to qualitatively validate the phase response seen in the modeled responses in Figures 3.13 and 3.14.

3.6.2. Layer-to-Layer Qualitative Model Validation. To validate the qualitative behavior of the two-dimensional LMD process model, an experimental multi-layer deposition is compared to the corresponding simulation results. Constant process parameters are used in both the simulated and actual deposition and a pocket is added to the substrate, 0.60 mm deep and 25.40 mm long, to emulate surface defects that might arise in LMD process builds. The pocket and the substrate are shown in Figure 3.18 and the process parameters are given in Table 3.3. The model parameters associated with Trial 2 are used for the simulation.

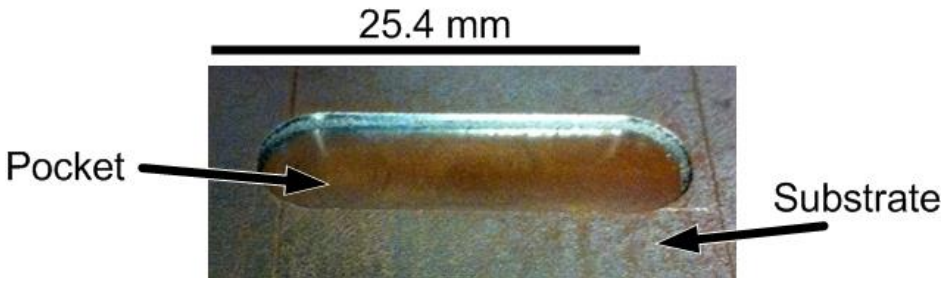

Figure 3.18. Photograph of pocket feature and substrate used in model validation.

Table 3.3. Process parameters for model validation.

Process Parameter	**Value**
Laser Power, Q (W)	350
Spatial Flow Rate, λ (kg/mm)	1.878×10^{-5}
Incremental Substrate Standoff Distance, δd_S (mm)	0.381
Part Standoff Distance, d_P (mm)	11.396

At the particular part standoff distance used in the validation build, the powder catchment efficiency decreases with respect to increasing part standoff distance, i.e., the

operating point is to the right of the maximum powder catchment efficiency in Figure 3.2. Because of this, the part of the deposition inside the pocket receives less powder than the part of the deposition that lies outside of the pocket. This phenomenon can be seen in Figure 3.19 for both the simulated and experimental depositions. The top pane in Figure 3.19 shows the height of the simulated part at every second layer between j = 0 (substrate) and j = 26 (top of the part) while the lower pane shows a photograph of the experimental deposition.

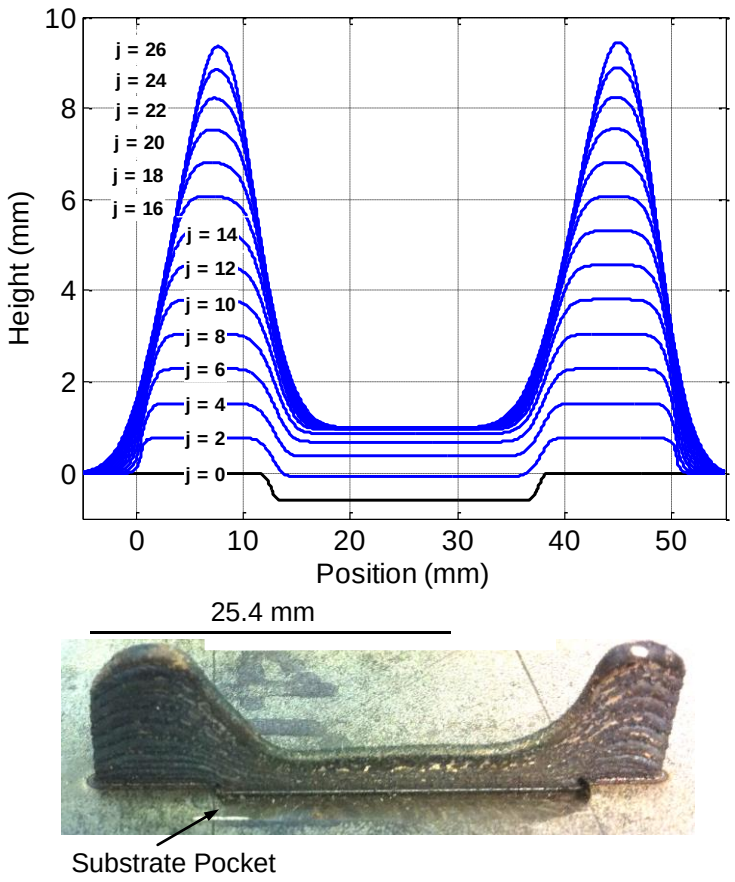

Figure 3.19. Simulation height signals for every second layer for j = 0 to j = 26 (top) and photograph of experimental deposition (bottom).

Initially, the difference between the powder catchment efficiency on top of the substrate and the powder catchment efficiency inside the pocket is relatively small, only a simulated 3.8% powder catchment efficiency difference. However, because less powder is deposited inside the pocket, the difference grows in magnitude each layer resulting in the large U-shape seen in both the simulation and experimental results. At the end of the deposit, the simulated difference between powder catchment efficiency between the tallest and lowest features is 11.8% and the low portions experience zero powder catchment efficiency. The simulated layer-to-layer powder catchment efficiency history is shown in Figure 3.20 at every fourth layer starting at layer $j = 1$, i.e., the powder catchment efficiency for the first bead deposited on top of the substrate. In normal operation, the substrate standoff distance d_S is incremented by a constant amount δd_S on each layer. When an amount of powder injected into the melt pool on a given layer results in a bead height δh less than δd_S, and the process is operating such that the powder catchment efficiency is decreasing with respect to increasing part standoff distance as in Figure 3.18, part standoff distance grows layer by layer. This phenomenon is manifested in the rapid attenuation of the powder catchment efficiency at the middle of the simulated deposit seen in Figure 3.19. Additionally, because no spatial flow rate is commanded at the very beginning and the very end of the simulated deposit, the bead height δh at those locations is much less than the layer-to-layer incremental substrate standoff distance, part standoff distance quickly grows layer by layer, and powder catchment efficiency rapidly attenuates.

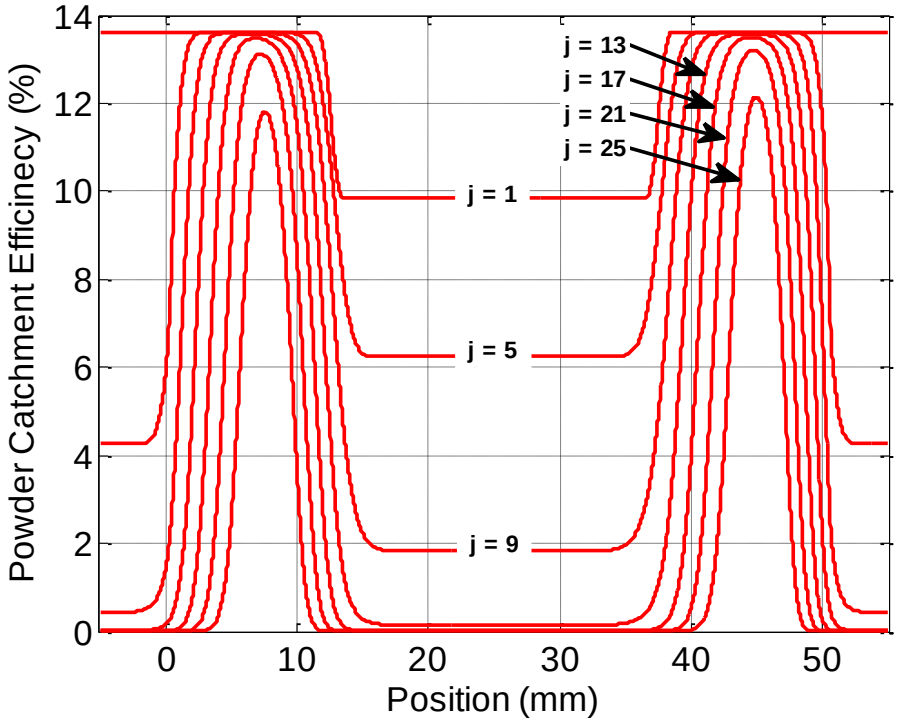

Figure 3.20. Simulated powder catchment efficiency for every fourth layer from $j = 1$ to $j = 25$.

From a control theoretic standpoint, this behavior can be classified as unstable. Because this unstable behavior is propagated in the layer-to-layer domain, i.e., the U-shaped defect grows in magnitude with each layer and not in the in-layer domain, and the LMD process model presented here describes both the layer-to-layer and in-layer dynamics, this unstable behavior can both be explained and predicted. The validated model developed here provides a foundation for layer-to-layer feedback control and, ultimately, a control-based stabilization of LMD processes. A stability analysis of AM processes and a methodology for closed-loop layer-to-layer control, along with an application to the LMD process, are presented in the following section.

4. OPEN-LOOP TWO-DIMENSIONAL PROCESS ANALYSIS

In this section, the stability of the general LNL system is analyzed and the application of the analytical tools developed in this section to the LMD process is presented. The section is organized as follows. First, the problem setup and assumptions are given. Then, conditions for the local stability of the general LNL system are given. Finally, the application to the LMD process is detailed.

4.1. PROBLEM SETUP AND ASSUMPTIONS

Consider the special case of the general LNL two-dimensional AM process description presented in Section I ((9) and shown schematically in Figure 1.3),

$$\begin{aligned} \boldsymbol{\upsilon}(x,j) &= \underbrace{\begin{bmatrix} g_{\mathbf{u}}(w) & \mathbf{D}w^{-1} \end{bmatrix}}_{G_1(w)} \begin{bmatrix} \mathbf{u}(x,j) \\ \mathbf{y}(x,j) \end{bmatrix} \\ \mathbf{y}(x,j) &= G_2(s)\, f\left(\boldsymbol{\upsilon}(x,j)\right) \end{aligned} \tag{41}$$

where again $(x,j) \in \mathbb{R} \times \mathbb{Z}_+$ is the independent variable pair representing an in-layer position x and a layer j, $\mathbf{y} \in \mathbb{R}^n$ is the output vector, $\mathbf{u} \in \mathbb{R}^m$ is the input vector containing known disturbances and control inputs, and $\boldsymbol{\upsilon} \in \mathbb{R}^p$ and $\boldsymbol{\xi} \in \mathbb{R}^r$ are vectors of internal process states. The following development assumes the following.

A1) The static nonlinearity $f : \mathbb{R}^p \to \mathbb{R}^r$ is continuously differentiable

A2) The matrix $\mathbf{D} \in \mathbb{R}^{p \times n}$ is constant and finite-valued

A3) The input partition $g_{\mathbf{u}}$ is assumed to be a finite order polynomial in w^{-1},

$$g_{\mathbf{u}} = \mathbf{B}_0 + \mathbf{B}_1 w^{-1} + \cdots + \mathbf{B}_{M_{\mathbf{T}}} w^{-M_{\mathbf{T}}} \tag{42}$$

where $\mathbf{B}_i \in \mathbb{R}^{p \times m}$ for $i = 0, 1, \ldots, M_{\mathbf{T}}$.

4.2. TWO-DIMENSIONAL STABILITY ANALYSIS

For stability analysis and control design, it is desired to know how small perturbations to the input **u** affect the output **y**. For the class of two-dimensional repetitive processes described by (41), the effect of perturbations is analyzed about an equilibrium point.

Definition 4.1: An reference point, $\Sigma(\mathbf{u}_e, \boldsymbol{\upsilon}_e, \mathbf{y}_e)$, of (41) is the set of constant inputs signals and internal states $\mathbf{u}(x, j) = \mathbf{u}_e$ and $\boldsymbol{\upsilon}(x, j) = \boldsymbol{\upsilon}_e$ and initial conditions which yield constant outputs $\mathbf{y}(x, j) = \mathbf{y}_e$ for $\forall (x, j) \in \mathbb{R} \times \mathbb{Z}_+$.

Consider the first-order Taylor series expansion about the reference point $\Sigma(\mathbf{u}_e, \boldsymbol{\upsilon}_e, \mathbf{y}_e)$,

$$f\left(\boldsymbol{\upsilon}(x, j), j\right) \approx f\left(\boldsymbol{\upsilon}_e, j\right) + D_{\boldsymbol{\upsilon}}\left(\boldsymbol{\upsilon}_e\right)\left(\boldsymbol{\upsilon}(x, j) - \boldsymbol{\upsilon}_e\right) \tag{43}$$

where

$$D_{\boldsymbol{\upsilon}}\left(\boldsymbol{\upsilon}_e\right)=\nabla f\left(\boldsymbol{\upsilon}\left(x,j\right)\right)\Big|_{\boldsymbol{\upsilon}(x,j)=\boldsymbol{\upsilon}_e}, \tag{44}$$

and $\nabla(\bullet)$ is the gradient operator. Define the input, internal state, and output incremental variables, respectively, as, $\bar{\mathbf{u}}\left(x,j\right)=\mathbf{u}\left(x,j\right)-\mathbf{u}_e$, $\bar{\boldsymbol{\upsilon}}\left(x,j\right)=\boldsymbol{\upsilon}\left(x,j\right)-\boldsymbol{\upsilon}_e$, and $\bar{\mathbf{y}}\left(x,j\right)=\mathbf{y}\left(x,j\right)-\mathbf{y}_e$. The linear approximation of the nonlinear repetitive process (41) evaluated at reference point gives the linear repetitive process *S*,

$$S\begin{cases}\bar{\boldsymbol{\upsilon}}\left(x,j\right)=\begin{bmatrix}g_{\mathbf{u}}\left(w\right) & \mathbf{D}w^{-1}\end{bmatrix}\begin{bmatrix}\bar{\mathbf{u}}\left(x,j\right)\\ \bar{\mathbf{y}}\left(x,j\right)\end{bmatrix}\\ \bar{\mathbf{y}}\left(x,j\right)=G_2\left(s\right)D_{\boldsymbol{\upsilon}}\bar{\boldsymbol{\upsilon}}\left(x,j\right)\end{cases} \tag{45}$$

where the arguments of $D_{\boldsymbol{\upsilon}}$ have been dropped for compactness. The system *S* can be transformed to the (*s*,*w*)-domain as

$$\bar{\mathbf{Y}}\left(s,w\right)=G_2\left(s\right)D_{\boldsymbol{\upsilon}}g_{\mathbf{u}}\left(w\right)\bar{\mathbf{U}}\left(s,w\right)+G_2\left(s\right)D_{\boldsymbol{\upsilon}}\mathbf{D}w^{-1}\bar{\mathbf{Y}}\left(s,w\right), \tag{46}$$

or $\bar{\mathbf{Y}}\left(s,w\right)=\mathbf{G}\left(s,w\right)\bar{\mathbf{U}}\left(s,w\right)$, where,

$$\mathbf{G}\left(s,w\right)=\left[\mathbf{I}-G_2\left(s\right)D_{\boldsymbol{\upsilon}}\mathbf{D}w^{-1}\right]^{-1}G_2\left(s\right)D_{\boldsymbol{\upsilon}}g_{\mathbf{u}}\left(w\right) \tag{47}$$

Theorem 4.1 (Open-Loop Stability): The linear repetitive process (45) is stable along the pass if $G_2(s)$ is asymptotically stable and,

$$\left\| G_2(s) D_{\mathbf{v}} \mathbf{D} \right\|_\infty < 1 \tag{48}$$

Furthermore, for the single output system, $n = 1$, (48) is necessary for stability.

Proof: From (7) and (8), the interpass operators for the linear repetitive process (15) are given by

$$\begin{aligned} \mathcal{G}(s) &= \mathbf{L}^{(1)}(s) = G_2(s) D_{\mathbf{v}} \mathbf{D} \\ \mathcal{D} &= \lim_{\omega_1 \to \infty} \mathbf{L}^{(1)}(i\omega_1) = \lim_{\omega_1 \to \infty} G_2(i\omega_1) D_{\mathbf{v}} \mathbf{D} \end{aligned} \tag{49}$$

Condition (a) of Theorem 1 is satisfied by asymptotic stability of $G_2(s)$. Conditions (b) and (c) of Theorem 1 are satisfied by (48) because the spectral radius is bounded by $\rho(\mathcal{D}) \le \left\| G_2(s) D_{\mathbf{v}} \mathbf{D}_1 \right\|_\infty$, with equality in the case of scalar systems, or $n = 1$. Thus, the result follows by Theorem 1. ■

Remark 4.1: The continuous differentiability of f, i.e., $D_{\mathbf{v}}$ is bounded, and the boundedness of $\mathbf{D}$ ensures only G_2 determines in-layer stability of the process.

Remark 4.2: Analogous to (7), the operator $G_2(s)D_{\mathbf{v}}\mathbf{D}$ describes the how output information is propagated from the single previous layers to the current layer. In addition to spatial domain information, it also describes the propagation of frequency content from the single previous output $\mathbf{y}(x,j-1)$ to the current layer $\mathbf{y}(x,j)$. When $G_2(s)D_{\mathbf{v}}\mathbf{D}$ attenuates content of $\mathbf{y}(x,j-1)$ at each frequency, layer domain asymptotic stability is achieved.

Remark 4.3: From Theorem 2 and the concept regarding stability along the pass described in Remark 6, it can be observed that a stable along the pass linear repetitive process will have final value $\bar{\mathbf{Y}}(i\omega_1, w) = 0$ only in the case when $\bar{\mathbf{U}}(i\omega_1, w) = \bar{\mathbf{U}}(i\omega_1)$ where $\bar{\mathbf{U}}(i\omega_1)$ is the in-layer frequency content of the input signal. Additionally, signals of the form $\bar{\mathbf{U}}(i\omega_1, w) = \left(1 - w^{-1}\right)^{-1} \bar{\mathbf{U}}(i\omega_1)$ (layer domain step inputs) result in non-zero, but finite final value. This scenario is analogous to a conventional one-dimensional Type 0 system. The same terminology is used here.

4.3. APPLICATION TO LMD

In order to analyze stability of the LMD process, it is necessary to establish the proper frame of reference. The height of the part, for instance, is intended to increase with each deposited layer and therefore, a more relevant frame for stability analysis is one that moves with the nozzle. In typical process operation, the nozzle is incremented each layer by the thickness of a layer (as determined by the CAM software). The growth of the part height on that layer is then expected to increase by the same amount. Thus, in stable operation, it is expected the distance from the nozzle to the part,

$$d_P(x, j) = d_S(x, j) - h(x, j-1) \tag{50}$$

where d_S is the height of the nozzle above the substrate (mm) and h is the part height (mm), to be bounded. Recall from Section 2.4 that the process dynamics are given by,

$$h(x,j) = b^{-1}\varsigma f_{\mu}\left(d_S(x,j) - h(x,j-1)\right)\lambda(x,j) * f_s(x) + h(x,j-1) * f_r(x) \qquad (51)$$

where λ is the spatial flow rate (kg/mm), b is the melt pool characteristic width (mm), ς is the material specific volume (mm^3/g), and the functions f_s, f_μ, and f_r are given in (22), (20), and (27), respectively.

In the following, the well-tuned commercial LMD process described by the model parameters for Trial 2, listed in Table 4.1, is used.

Table 4.1. Open-Loop LMD Process Parameters.

Parameter	**Value**
Characteristic Melt Pool Length, l_0 (mm)	0.61
Characteristic Melt Shift, δ (mm)	-0.01
Re-Melt Characteristic Length, l_r (mm)	1.21
Maximum Powder Catchment, α_{max} (%)	16.04
Location of Powder Catchment Maximum, d_{max} (mm)	10.57
Powder Catchment Width, α_{width} (mm)	2.04
Material Specific Volume, ς (mm^3/g)	1.25×10^{2}
Characteristic Bead Width, b_0 (mm)	0.84
Spatial Flow Rate Reference Point, λ_e (g/mm)	1.26×10^{-2}
Part Standoff Reference Point, $d_{P,e}$ (mm)	10.47
Layer-to-Layer Substrate Standoff Change, δd_S (mm)	0.30
Bead Height Reference Point, δh_e (mm)	0.30

Consider the open-loop process references $\lambda(x,j) = \lambda_e$, where λ_e is a selected constant spatial flow rate and $d_S(x,j) = d_{S,0} + j\delta d_S$, where $d_{S,0}$ is the constant initial nozzle offset and δd_S is the constant layer to layer increment in d_S. Rewriting (50) with (51) gives

$$d_P(x,j) = d_S(x,j) - b^{-1}\varsigma f_\mu\left(d_P(x,j-1)\right)\lambda(x,j-1) * f_s(x) - h(x,j-2) * f_r(x) \quad (52)$$

Recall that f_r has a DC gain of unity (according to (27), but also ensured by the law of conservation of mass). Therefore,

$$f_r(x) * d_S(x,j) = f_r(x) * \left(d_{S,0} + j\delta d_S\right) = d_{S,0} + j\delta d_S = d_S(x,j) \quad (53)$$

Using (50), (53), and d_S given above, (52) can be written as,

$$d_P(x,j) = -b^{-1}\varsigma f_\mu\left(d_P(x,j-1)\right)\lambda(x,j-1) * f_s(x) + \left(\delta d_S + d_P(x,j-1)\right) * f_r(x) \quad (54)$$

or in the form of (41) where,

$$\mathbf{u}(x,j) = \lambda(x,j) \quad (55)$$

$$\mathbf{v}(x,j) = \begin{bmatrix} \lambda(x,j) & y(x,j-1) \end{bmatrix}^T \quad (56)$$

$$\begin{aligned} G_1(w) &= \left[\begin{array}{c|c} w^{-1} & 0 \\ \hline 0 & w^{-1} \end{array}\right] \\ f\left(\mathbf{v}(x,j)\right) &= \begin{bmatrix} -b^{-1}\varsigma f_\mu\left(\upsilon_2(x,j)\right)\upsilon_1(x,j) \\ \delta d_S + \upsilon_2(x,j) \end{bmatrix} \\ G_2(s) &= \begin{bmatrix} F_s(s) & F_r(s) \end{bmatrix} \end{aligned} \quad (57)$$

The reference points for the LMD process under constant spatial flow rate λ_e and layer to layer change in standoff distance δd_S are, solutions of

$$f_\mu\left(d_{P,e}\right) = \frac{b\delta d_S}{\lambda_e \varsigma}. \tag{58}$$

The solutions of (58) can be considered in three cases as follows.

Case I (Large Layer Increments): When $\alpha_{max} < \frac{b\delta d_S}{\lambda_e \varsigma}$, no reference points exist. In this case, the layer to layer increment distance δd_S is too large for spatial flow rate λ_e. That is, the amount of powder captured by the melt pool is not enough to produce the necessary growth in part height to match the layer to layer change in substrate standoff distance.

Case II (Maximum Efficiency): When $\alpha_{max} = \frac{b\delta d_S}{\lambda_e \varsigma}$, one reference solution exists, which is given by $d_{P,e} = d_{max}$. In this case, the layer to layer increment δd_S can only be matched by part height growth when the part standoff distance is set at the most efficient location.

Case III (Low Efficiency): When $\alpha_{max} > \frac{b\delta d_S}{\lambda_e \varsigma}$, two reference solutions exist, which are given by, $d_{P,e} = d_{max} + \alpha_{width}\sqrt{-\ln\left(\frac{b\delta d_S}{\lambda_e \varsigma \alpha_{max}}\right)}$ and $d_{P,e} = d_{max} - \alpha_{width}\sqrt{-\ln\left(\frac{b\delta d_S}{\lambda_e \varsigma \alpha_{max}}\right)}$.

Linearizing *f* about a reference point, i.e., Case II or III above, yields,

$$D_{\mathbf{v}}\left(\mathbf{v}(j)\right)=\begin{bmatrix}\kappa_1 & -\kappa_2\\ 0 & 1\end{bmatrix} \tag{59}$$

where,

$$\begin{aligned}\kappa_1 &= \frac{\partial}{\partial\lambda(x,j-1)}\left(b^{-1}\varsigma f_\mu\left(d_P(x,j-1)\right)\lambda(x,j-1)\right)\Big|_{d_P(x,j-1)=d_{P,e},\lambda(x,j-1)=\lambda_e}\\ &= b^{-1}\varsigma f_\mu\left(d_{P,e}\right)\\ \kappa_2 &= \frac{\partial}{\partial d_P(x,j-1)}\left(b^{-1}\varsigma f_\mu\left(d_P(x,j-1)\right)\lambda(x,j-1)\right)\Big|_{d_P(x,j-1)=d_{P,e},\lambda(x,j-1)=\lambda_e}\\ &= b^{-1}\varsigma\lambda_e 2\frac{\left(d_{max}-d_{P,e}\right)}{\alpha_{width}} f_\mu\left(d_{P,e}\right)\end{aligned} \tag{60}$$

Theorem 4.2: The LMD process is locally open-loop stable along the pass if, and only if,

$$\sup_{\omega_1}\left|F_r(i\omega_1)-\kappa_2 F_s(i\omega_1)\right|<1 \tag{61}$$

Proof: From Part I of this paper, f_s and f_r are constrained by conservation of mass such that,

$$\int_{-\infty}^{\infty}\left|f_s(x)\right|dx=1,\ \int_{-\infty}^{\infty}\left|f_r(x)\right|dx=1 \tag{62}$$

and are of finite support which implies G_2 is asymptotically stable. The linear interpass operators are

$$\begin{aligned} \mathcal{G}(s) &= G_2(s)\begin{bmatrix} \kappa_1 & -\kappa_2 \\ 0 & 1 \end{bmatrix}\begin{bmatrix} 0 \\ 1 \end{bmatrix} = G_2(s) D_{\mathbf{v}}\mathbf{D} = F_r(s) - \kappa_2 F_s(s) \\ \mathcal{D} &= \lim_{\omega_1 \to \infty} \mathcal{G}(i\omega) = \lim_{\omega_1 \to \infty} F_r(i\omega) - \kappa_2 F_s(i\omega) \end{aligned} \tag{63}$$

Application of Theorem 2 gives the result. ■

Lemma 1: Let $\alpha_{max} \geq \dfrac{b\delta d_S}{\lambda_e \varsigma}$ and $\dfrac{\delta d_S}{\alpha_{width}} d_{max} < 1$. A necessary condition for LMD process stability is,

$$0 < d_{P,e} < d_{max}\,. \tag{64}$$

Proof: From (58) and (60), $\kappa_2 > 0$ when (64) is true. Further,

$$\begin{aligned} \kappa_2 &= b_0^{-1}\varsigma\lambda_e 2\frac{\left(d_{max} - d_{P,e}\right)}{\alpha_{width}} f_\mu\left(d_{P,e}\right) \\ &= \delta d_S 2\frac{\left(d_{max} - d_{P,e}\right)}{\alpha_{width}} \\ &< 2 \end{aligned} \quad . \tag{65}$$

Conservation of mass implies that at DC, $F_r = F_s = 1$ and thus (61) only holds for $0 < \kappa_2 < 2$. ■

In typical practical applications, the upper stability bound on κ_2 is not achieved. The LMD process described by the model parameters in Table 1, the functions (20) and (27), $\kappa_2 = 4.809\times10^{-3}$, and $d_{P,e} = 10.47$ mm, is locally stable along the pass.

Remark 4.3: Physically, Theorem 4 indicates that the shape of the powder flow out of the cladding head is extremely important for process stability as κ_2 is explicitly a function of and proportional to the powder catchment efficiency and its slope. Specifically, for open-loop stability it is necessary to have positive slope, or increasing catchment efficiency at increasing standoff distance. Therefore, it is not possible to stably operate the process at the location of maximum catchment efficiency, where the slope is zero. Thus, stabilizing process control is necessary for maximum powder catchment efficiency, or minimum powder loss, in LMD processes.

Remark 4.4: For typical (open-loop) build applications with the commercial system on which the process was identified, the nominal part standoff distance is set to $d_P = 9.53$ mm (marked with point A in Figure 4.1), corresponding to a catchment efficiency of $\mu = 0.12$. This nominal standoff distance was determined to produce satisfactory structures through extensive trial and error. However, Theorem 4 provides a theoretical explanation of the resulting build at that operating point - it lies well within the open-loop stable region ($\kappa_2 = 5.184\times10^{-2}$). Although $d_P = 9.53$ mm is a stable part standoff distance, the catchment efficiency at this standoff distance is only 75% that of the maximum catchment efficiency (marked with point B in Figure 4.1) indicating an efficiency improvement can be made.

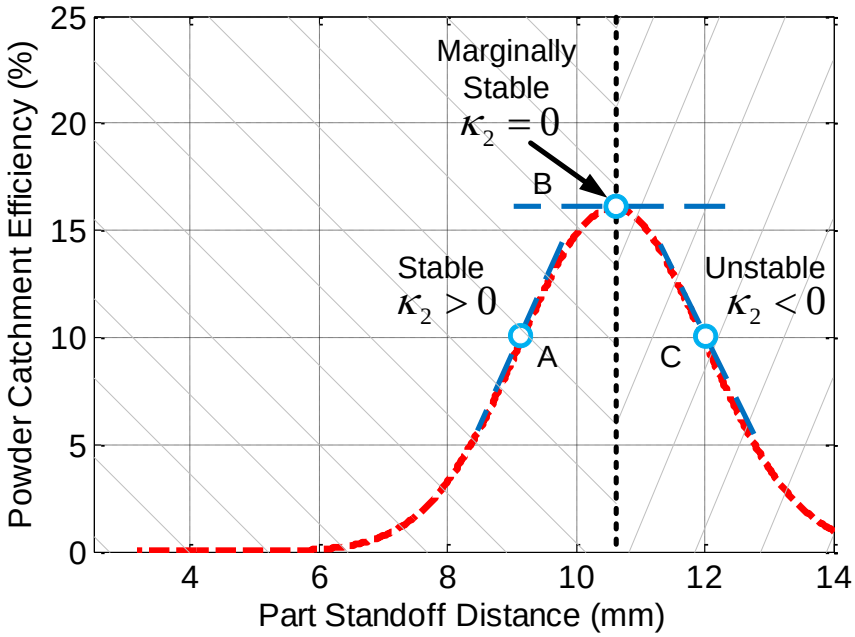

Figure 4.1. Schematic of the powder catchment efficiency function showing a stable part standoff distance (A) and the along the pass unstable maximum powder catchment efficiency (B).

Influence of Powder Catchment Efficiency on Layer-to-Layer Stability. For a physical interpretation of the stability criteria in (61), consider a structure whose top surface has a notch feature and a powder catchment function which follows the experimentally identified Gaussian shape as illustrated in Figure 3.2 and given by (22).

In typical LMD processes, the layer-to-layer change in the substrate standoff distance δd_S is a constant amount for each layer based on knowledge of the bead height δh for a given set of process parameters. If the part standoff distance $d_{P,0}$ is initially set such that the melt pool forms in Region A (upper pane in Figure 4.2), the linearization constant κ_2 in (60) which is proportional to the rate of change of powder catchment efficiency with respect to part standoff distance, is positive. That is, the powder

catchment efficiency is increasing with respect to increasing part standoff distance. In this case, the depth of the notch feature will reduce because the powder catchment efficiency is inversely proportional to feature height.

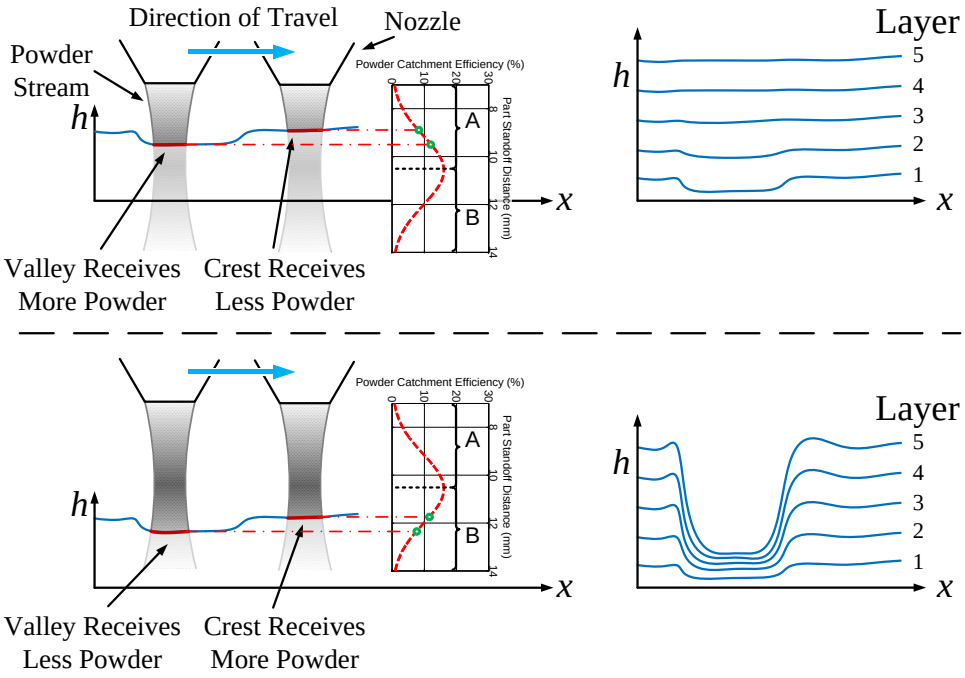

Figure 4.2. Schematic of deposition process around a stable part standoff distance (Region A, top) and around an unstable part standoff distance (Region B, bottom).

When the substrate standoff distance is incremented a constant amount, the melt pool again forms in Region A, further reducing the depth of the notch feature. If the multi-layer deposition is continued without operator intervention when the melt pool lies in Region A, evidence of the notch will continue to attenuate from layer to layer until a constant part height is achieved, as illustrated by the layer-domain schematic on the right hand side of the top pane in Figure 4.2.

Alternatively, if the part standoff distance $d_{P,0}$ is initially set such the the melt pool forms in Region B (lower pane in Figure 4.2), the linearization constant κ_2 is negative. That is, the powder catchment efficiency is decreasing with respect to increasing part standoff distance. Incrementing the substrate standoff distance a constant amount and repeating the deposition process with the part standoff distance such that the melt pool lies in Region B further amplifies the notch feature. Without operator intervention, the layer-to-layer growth will eventually lead to catastrophic defects in the deposition, as illustrated in the lower pane in Figure 4.2.

4.4. PROCESS STABILITY MAPS

While closed-loop process control is desired, in its absence, a potentially useful tool for operators is a map of the process space clearly denoting which regions will lead to layer-to-layer instability and which regions will yield a layer-to-layer stable build. In this section, a process map generated from the DC-gain properties of F_s and F_r is presented. In typical applications when uniform height structures are desired, the map, termed the DC process map, is adequate for determining processing parameters which will result in a stable build. However, because the DC process map is generated by neglecting the in-layer dynamics, a more detailed map may be needed in the case when several operating points are used throughout a build.

DC Process Map. From the frequency domain properties of the process kernels fs and fr given in Section 3.5, at DC, i.e., $\omega 1 \approx 0$, both kernels are real-valued and unit gain regardless of the values of the kernel parameters l, δ, and lr,

$$\begin{aligned} F_s(0) &= 1 \\ F_r(0) &= 1 \end{aligned}. \tag{66}$$

Thus, the two-dimensional model (54) at DC, again regardless of the kernel parameter values, is written as

$$d_P(j) = -b^{-1}\varsigma f_\mu\left(d_P(j-1)\right)\lambda(j-1) + \delta d_S + d_P(j-1) \tag{67}$$

where the explicit dependence on position is dropped as the in-layer component of the process is static. Denote the incremental variables (as in Section 4.2) as $\bar{\lambda}$ and $\bar{d}_P$. The linearized representation of (67) is

$$\bar{d}_P(j) = (1-\kappa_2)\bar{d}_P(j-1) + \kappa_1\bar{\lambda}(j-1) \tag{68}$$

where κ_1 and κ_2 are defined as in (60).

Of note is that (68) is a dynamic equation purely in the discrete domain *j*, i.e., the current part standoff distance is the previous part standoff distance plus an input. Thus, (68) is analogous to a scalar discrete time dynamic equation. Therefore, instead of applying the criterion in (61), here conventional discrete time results are used to determine the DC LMD process stability criterion.

Theorem 4.3 (DC Stability Criterion): The DC LMD process in (68) is locally layer-to-layer stable if

$$|1-\kappa_2|<1. \tag{69}$$

Proof: Application of the *w*-transform to (68) gives

$$\bar{D}_P(w)=\frac{\kappa_1 w^{-1}}{1-(1-\kappa_2)w^{-1}}\bar{\Lambda}(w) \tag{70}$$

where $\bar{D}_p$ is the *w*-domain representation of $\bar{d}_P$ and $\bar{\Lambda}$ is the *w*-domain representation of $\bar{\lambda}$. Application of discrete time system stability results to (70) gives the result. ■

Note that while (69) requires both that $0 < \kappa_2 < 2$, in practice $|\kappa_2| < 1$ due in large part to the physically limited amount of powder that can be captured by the melt pool. An order of magnitude analysis indicates that spatial flow rate must exceed roughly $\lambda = 1\times10^{-3}$ kg/mm in order to achieve the upper stability bound on κ_2. Process parameter combinations needed to achieve this spatial flow rate are not typical of LMD operations where spatial flow rates are on the order of $\lambda = 1\times10^{-5}$ kg/mm.

A map generated from (69), while only valid near a defined operating point, allows operators to quickly determine valid sets of constant process parameters which yield stable layer-to-layer LMD fabrications without laborious trial and error. Noting the inputs required to calculate κ_2 in (60), i.e., d_P and λ, a range of part standoff distances and spatial flow rates are chosen which cover a relatively broad range of the process space. These ranges of input values are used to calculate κ_2 and subsequently $|1 - \kappa_2|$. The

resulting values are plotted with respect to the part standoff distances and spatial flow rates. The model parameters identified for the Optomec MR-7 system using 316 Stainless Steel, given in Table 4.1, are used in the subsequent simulation study. Values of spatial flow rate from $\lambda = 1\times10^{-6}$ kg/mm to 1×10^{-3} kg/mm and part standoff distance between $d_P = 2$ mm and 14 mm were used to calculate the stability criterion.

The resulting process map is shown in Figure 4.3. The shaded regions labeled "Unstable Region" indicate areas where the DC stability criterion is violated, $|1 - \kappa_2| \geq 1$. The contour lines in Figure 4.3 correspond to constant levels of $|1 - \kappa_2|$. From a mathematic standpoint, the value of $(1 - \kappa_2)$ is the common ratio of a geometric series which dictates the convergence rate of the series. Additionally, from Theorem 4.3, $(1 - \kappa_2)$ is the pole location of the first order linear system in (68). Both indicate that magnitudes closer to zero yield a faster convergence rate or response time to the origin and magnitudes closer to one yield a slower convergence rate or response time to the origin. However, because the pole location itself does not convey explicit information about the system response, the response is quantified using the system setting time. Therefore, the numeric values shown on the contours in Figure 4.3 represent the layer-to-layer time settling time,

$$n = 4\left\lceil \log_{|1-\kappa_2|} e^{-1} \right\rceil \tag{71}$$

where n is the integer number of layers required to recover to within approximately 2% of the height reference, i.e., for the system in (68) to return to the origin, and $\lceil \bullet \rceil$ denotes the ceiling function.

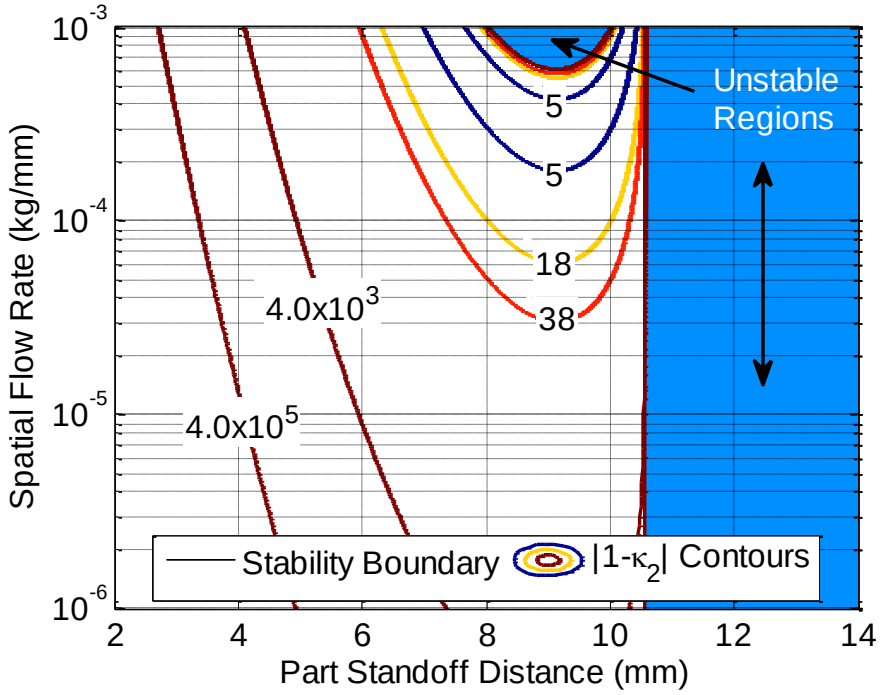

Figure 4.3. Layer-to-layer stability process map for process parameters given in Table 4.1.

Clearly, there is a very sharp boundary between the right hand Unstable Region and the stable region. This line indicates the part standoff distance d_{max} when the slope of the powder catchment efficiency is zero. The right hand side of this boundary corresponds to a negative powder catchment efficiency slope and the left hand side corresponds to a positive powder catchment efficiency slope. The second Unstable

Region, located at the top of the process map, corresponds to values of $\kappa_2 > 2$. As stated previously, this region is largely an area of infeasible combinations of process inputs.

An interesting phenomenon arises by examining the contours around the part standoff distance $d_P = 9.5$ mm. In this region, the gradient of the contours with respect to part standoff distance is approximately zero. When a specific settling time is desired, this area of the process parameter space is the most robust to changes in part standoff distance. As part standoff distance increases or decreases, it is more difficult to maintain a specific settling time due to the sensitivity of the contours in these locations. Further, it is observed that the settling time decreases steadily with increasing spatial flow rate until an inflection point in the map is reached. After which, the settling time increases extremely rapidly and the map enters the unstable region around 6×10^{-4} kg/mm.

5. TWO-DIMENSIONAL LAYER-TO-LAYER FEEDBACK CONTROL

In this section, details pertaining to pure feedback control and to combination feedback/feedforward control design are given. In LMD, it is sufficient to control part height, h, with spatial flow rate, λ. Therefore, the Single-Input Single-Output (SISO, $n = m = 1$) case is considered here. Extensions of the details given below to Multiple-Input Multiple-Output systems are omitted here for compactness of presentation. However, these extensions are straightforward.

5.1. LAYER-TO-LAYER FEEDBACK CONTROL

Consider the two-dimensional feedback loop shown in Figure 5.1 where $\mathbf{C}(s,w)$ is a to-be-designed layer-to-layer controller. In LMD processes, it is desired to deposit a uniform bead height on each layer. This scenario is best described by a layer-to-layer ramp reference signal. From Remark 4.3, a stable SISO linear repetitive process is termed a Type 0 system and application of Theorem 2 reveals that the final value of this scenario does not exist. Therefore, in order to track ramp references, which contain two pure layer-to-layer integrators, at least one layer-to-layer integrator must be placed in the forward loop of the closed loop. Thus, consider the layer-to-layer controller is of the form

$$\mathbf{C}(s,w)=\mathbf{K}(s)\frac{\prod_{k_\beta=1}^{M_\beta}\left(1+\boldsymbol{\beta}_{k_\beta}(s)w^{-1}\right)}{\left(1-w^{-1}\right)\prod_{k_\alpha=1}^{M_\beta}\left(1+\boldsymbol{\alpha}_{k_\alpha}(s)w^{-1}\right)} \tag{72}$$

where $\boldsymbol{\alpha}_{k_\alpha}$, $\boldsymbol{\beta}_{k_\beta}$, and $\mathbf{K}$ are the controller parameters and are rational transfer functions in s. Define the incremental tracking error as

$$\bar{\mathbf{e}}(x, j) = \bar{\mathbf{r}}(x, j) - \bar{\mathbf{y}}(x, j) \tag{73}$$

where $\bar{\mathbf{r}}(x, j) = \mathbf{r}(x, j) - \mathbf{y}_e$ is the layer-to-layer incremental reference signal and $\mathbf{r}(x, j)$ is the layer-to-layer reference. The input to the compensator $\mathbf{C}$ is the two-dimensional frequency domain representation of the incremental tracking error, $\bar{\mathbf{E}}(s, w) = \mathcal{LW}\{\bar{\mathbf{e}}(x, j)\}$ and the output is $\bar{\mathbf{U}}(s, w)$.

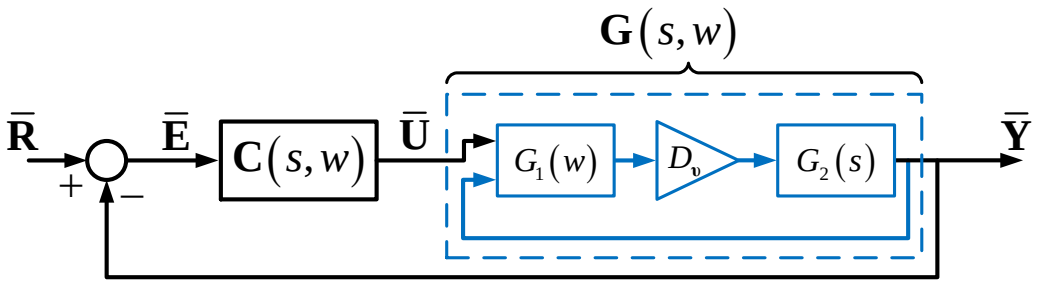

Figure 5.1. Two-dimensional (s,w)-domain block diagram of general linearized AM process with feedback control.

The closed-loop equation is,

$$\bar{\mathbf{Y}}(s, w) = \left[1 + \mathbf{G}(s, w)\mathbf{C}(s, w)\right]^{-1} \mathbf{G}(s, w)\mathbf{C}(s, w)\bar{\mathbf{R}}(s, w) \tag{74}$$

where the closed-loop interpass operators (6) are denoted as $\mathbf{L}^{(k_{\mathbf{L},CL})}$ for $k_{\mathbf{L},CL} = 1, \ldots, M_{\mathbf{L},CL}$ and $\mathbf{T}^{(k_{\mathbf{T},CL})}$ for $k_{\mathbf{T},CL} = 1, \ldots, M_{\mathbf{T},CL}$. This procedure provides guidelines, based on Theorem 1.1, for designing a stabilizing layer-to-layer SISO controller.

A Pole Placement Procedure. As stated above, the procedure presented in this subsection leverages Theorem 1.1 to design a stabilizing layer-to-layer feedback controller. The procedure is as follows.

1. Select a desired two-dimensional compensator structure **C** (e.g., Select a desired two-dimensional compensator structure **C** (e.g., desired number of denominator and numerator parameters, $M_{\boldsymbol{\alpha}}$ and $M_{\boldsymbol{\beta}}$, respectively).
2. Let $\boldsymbol{\eta}_{\mathcal{G},d} = \boldsymbol{\eta}_{\mathcal{D},d} = \left\{\eta_{k_{CL},d}\left(i\omega_1\right)\right\}_{k_{\mathbf{L},CL}=1}^{M_{\mathbf{L},CL}}$ be a set of $M_{\mathbf{L},CL}$ desired interpass matrix ((7) and (8)) eigenvalues, each as a function of in-layer frequency ω_1, which satisfy the requirements for stability along the pass in Theorem 1.
3. Compute the desired layer-to-layer operators $\mathbf{L}_d^{(k_{CL})}$ corresponding the set of eigenvalues,

$$\prod_{k_{CL}=1}^{M_{CL}}\left(1+\eta_{k_{CL},d}\left(i\omega_1\right)w^{-1}\right)=1-\mathbf{L}_d^{(1)}w^{-1}-\cdots-\mathbf{L}_d^{(M_{CL})}w^{-M_{CL}} \tag{75}$$

4. Equate like coefficients of (75) and the closed-loop operators in (74) to determine the controller layer-to-layer parameters $\boldsymbol{\alpha}_{k_{\boldsymbol{\alpha}}}$, $\boldsymbol{\beta}_{k_{\boldsymbol{\beta}}}$, and **K**.

Remark 5.1: There are at least two possible methods for calculating an implementable control signal $\mathbf{u}(x,j)$ as the output of the compensator $\mathbf{C}$. The first is achieved by finding or fitting closed-form expressions for each compensator parameters $\boldsymbol{\alpha}_{k_\alpha}$, $\boldsymbol{\beta}_{k_\beta}$, and $\mathbf{K}$. and applying the inverse Laplace transform to obtain a differential equation with respect to x for $\mathbf{u}(x,j)$. To employ this first method, the transfer function representations need to be realizable which requires they be at least proper. This condition is not true in general, as the controller pole, gain, and zero are calculated using the process filters and the possibly frequency dependent closed-loop characteristic equation coefficients. However, in certain cases, with the careful selection of the desired closed-loop equation, the compensator parameters can be shown to be proper. The second method requires the compensator parameters and the measured signals $\overline{\mathbf{u}}$ and $\overline{\mathbf{e}}$ be converted into the discrete in-layer frequency domain using the forward Fourier transform. The implementable control signal is then acquired using the inverse Fourier transform. This second method for implementation – using the forward and inverse Fourier transforms – is preferred as it allows for more design freedom in that each parameter of the compensator is always realizable. An explicit formula for an implementable control signal is given in the next subsection.

5.2. APPLICATION TO THE LMD PROCESS

Layer-to-Layer Feedback Control. The control problem formulated here is that of a tracking problem where the controller input is the error between the actual incremental part standoff distance and the desired incremental part standoff distance $\overline{\mathbf{e}}(x, j)$. The linear, spatially-invariant repetitive process description is then

$$\bar{\mathbf{Y}}(s,w)=\frac{\kappa_1 F_s(s)w^{-1}}{1-\left(F_r(s)-\kappa_2 F_s(s)\right)w^{-1}}\bar{\mathbf{U}}(s,w) \tag{76}$$

with $\mathbf{L}^{(1)}(s)=F_r(s)-\kappa_2 F_s(s)$ and $\mathbf{T}(s,w)=\mathbf{T}^{(0)}(s)=\kappa_1 F_s(s)$. In order to track part standoff distance references with zero error, a layer-to-layer integrator is needed in the forward loop of the closed-loop. Therefore, the compensator used here is of the form in (72) with $M_{\boldsymbol{\alpha}} = 2$, $M_{\boldsymbol{\beta}} = 2$, $\boldsymbol{\beta}_1 = 0$, and $\boldsymbol{\alpha}_1$ and $\boldsymbol{\beta}_2$ are design parameters,

$$\mathbf{C}(s,w)=\mathbf{K}(s)\frac{w^{-1}\left(\boldsymbol{\beta}_2(s)+w^{-1}\right)}{\left(1-w^{-1}\right)\left(1+\boldsymbol{\alpha}_1(s)w^{-1}\right)}. \tag{77}$$

Following the development in Section III.A and the Pole Placement Procedure, the compensator parameters are determined by first selecting a set of stable, desired closed-loop interpass matrix eigenvalues. A set of eigenvalues which exhibit near deadbeat response in the layer domain is $\boldsymbol{\eta}=\begin{bmatrix}\eta_{1,d} & \eta_{2,d} & \eta_{3,d}\end{bmatrix}=\begin{bmatrix}1\times10^{-3} & 1\times10^{-3} & 5\times10^{-3}\end{bmatrix}$, $\forall\omega_1\in\mathbb{R}_+$. These eigenvalues clearly satisfy Theorem 3 and the desired layer-to-layer operators are

$$\begin{aligned}\mathbf{L}_d^{(1)}&=-\left(\eta_{1,d}+\eta_{2,d}+\eta_{3,d}\right)\\ \mathbf{L}_d^{(2)}&=-\left(\eta_{1,d}\eta_{3,d}+\eta_{3,d}\eta_{2,d}+\eta_{1,d}\eta_{2,d}\right)\\ \mathbf{L}_d^{(3)}&=-\eta_{1,d}\eta_{2,d}\eta_{3,d}\end{aligned} \tag{78}$$

Equating like coefficients gives the compensator parameters, in terms of the process dynamics,

$$\begin{aligned}
\boldsymbol{\alpha}_1(\omega) &= \left[\mathbf{L}^{(1)}(\omega)\right]^{-1}\mathbf{L}_d^{(3)} \\
\mathbf{K}(\omega) &= \mathbf{T}^{-1}(\omega, w)\left(\mathbf{L}_d^{(1)} - \left[\mathbf{L}^{(1)}(\omega)\right]^{-1}\mathbf{L}_d^{(3)} + \mathbf{L}^{(1)}(\omega) + 1\right) \\
\boldsymbol{\beta}_2(\omega) &= \frac{\left[\mathbf{L}^{(1)}(\omega)\right]^{-1}\mathbf{L}_d^{(3)} - \mathbf{L}_d^{(1)} - 1 - \mathbf{L}^{(1)}(\omega)}{\left(1 + \left[\mathbf{L}^{(1)}(\omega)\right]^{-1}\right)\mathbf{L}_d^{(3)} - \mathbf{L}_d^{(2)} - \mathbf{L}^{(1)}(\omega)}
\end{aligned} \tag{79}$$

The closed-loop LMD process description can be written in the form of (1) as

$$\bar{\mathbf{y}}(x, j) = \sum_{k_{CL}=1}^{3} \mathbf{L}_{CL}^{(k_{CL})}\bar{\mathbf{y}}(x, j - k_{CL}) + \mathbf{T}_{CL}^{(1)}\bar{\mathbf{r}}(x, j-1) + \mathbf{T}_{CL}^{(2)}\bar{\mathbf{r}}(x, j-2) \tag{80}$$

with

$$\begin{aligned}
\mathbf{L}_{CL}^{(1)}(s) &= -\left(\boldsymbol{\alpha}_1(s) - 1 - \mathbf{L}^{(1)}(s) + \mathbf{K}(s)\boldsymbol{\beta}_2(s)\mathbf{T}^{(0)}(s)\right) \\
\mathbf{L}_{CL}^{(2)}(s) &= -\left(\boldsymbol{\alpha}_1(s) - \mathbf{L}^{(1)}(s)\left(\boldsymbol{\alpha}_1(s) - 1\right) + \mathbf{K}(s)\mathbf{T}^{(0)}(s)\right), \\
\mathbf{L}_{CL}^{(3)}(s) &= -\mathbf{L}^{(1)}(s)\boldsymbol{\alpha}_1(s)
\end{aligned} \qquad \begin{aligned}
\mathbf{T}_{CL}^{(1)}(s) &= \mathbf{T}^{(0)}(s)\mathbf{K}(s)\boldsymbol{\beta}_2(s) \\
\mathbf{T}_{CL}^{(2)}(s) &= \mathbf{T}^{(0)}(s)\mathbf{K}(s)
\end{aligned} \tag{81}$$

In the following simulation result, the control law is implemented using the second method described in the previous section. That is, the previous two error signals $\mathbf{e}(x, j-1)$ and $\mathbf{e}(x, j-2)$ are converted to the frequency domain using the forward Fourier transform, the frequency domain control signal is calculated via the compensator

and compensator parameters in (77) and (79) and the spatial domain signal is calculated using the inverse Fourier transform to yield $\lambda(x, j)$.

Open- and Closed-Loop Simulation. Two sets of simulations are presented in this section: an open- and closed-loop simulation showing a uniform height deposition and an open- and closed-loop simulation showing the sensitivity of the open-loop process to small initial features at maximum process efficiency.

For the first simulation scenario, the goal is to build a thin-walled structure (i.e., one bead in width) of uniform height starting at x_s = 0 mm and ending at x_e = 50 mm in increments of δd_S = 0.3 mm at a desired part standoff of $d_{P,0}$ = 10.47 mm with a final part height of 15 mm. The build reference is

$$r(x, j) = (j+1)\xi(x) \tag{82}$$

where r is the two-dimensional part height reference (mm) and ξ is the in-layer reference height profile (mm),

$$\xi(x) = \delta d_S \left(f_{ref}(x) * \text{rect}(x_s, x_e) \right) \tag{83}$$

and

$$f_{ref}(x) = \begin{cases} 1-|x| & -1 \le x \le 1 \\ 0 & \text{otherwise} \end{cases} \tag{84}$$

$$\mathrm{rect}\left(x_1, x_2\right) = \begin{cases} 1 & x_1 \le x \le x_2 \\ 0 & \text{otherwise} \end{cases}. \tag{85}$$

While the open-loop process solution trajectory is stable, the performance is not desirable for uniform structure builds. This is demonstrated by the height signals resulting from the open-loop nonlinear simulation shown in Figure 5.2.

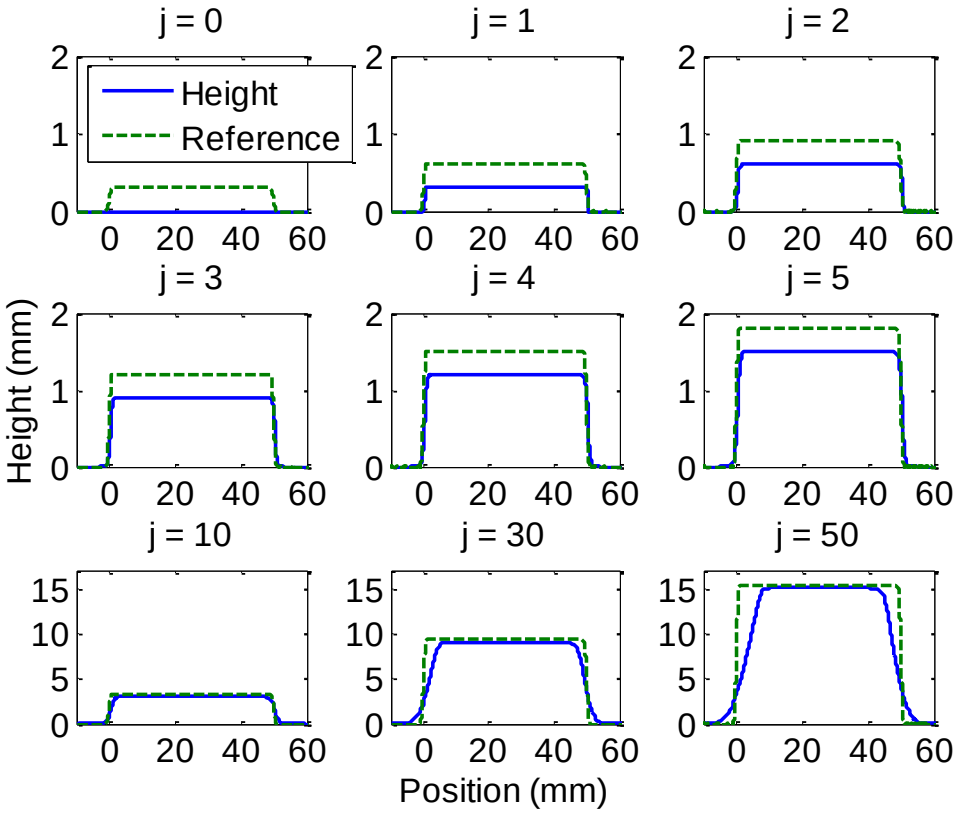

Figure 5.2. Height h and reference r signals at j = 0, 1, 2, 3, 4, 5, 10, 30, and 50 for open-loop ($\lambda_e = 1.26\times10^{-2}$ g/mm) simulation of Scenario 1.

For each layer, constant spatial flow rate $\lambda_e = 1.26\times10^{-2}$ g/mm is commanded to start at $x_s = 0$ and end at $x_e = 50$ mm. The substrate standoff distance is incremented by δd_S each layer with an initial standoff equal to $d_{P,0}$. As the part height increases, the wall narrows due to both the re-melt dynamics f_r and the exponential decay of the catchment in the vertical direction near the beginning and end of the deposition.

The simulated height signals with control applied at layers j = 0, 1, 2, 3, 4, 5, 10, 30, and 50, as well as the corresponding reference signals, are shown in Figure 5.3.

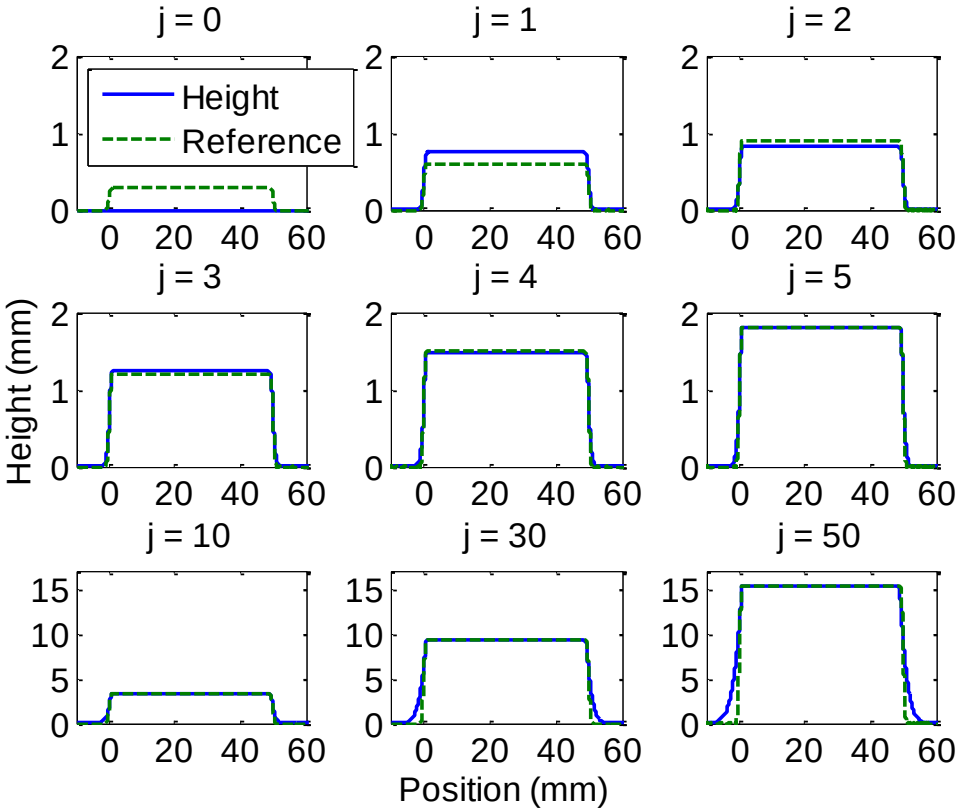

Figure 5.3. Height h and reference r signals at j = 0, 1, 2, 3, 4, 5, 10, 30, and 50 for closed-loop control simulation of Scenario 1.

Because the process is purely additive and negative control action indicates material removal, the control signals shown in Figure 5.4 are lower saturated at zero. The control signals are not upper saturated.

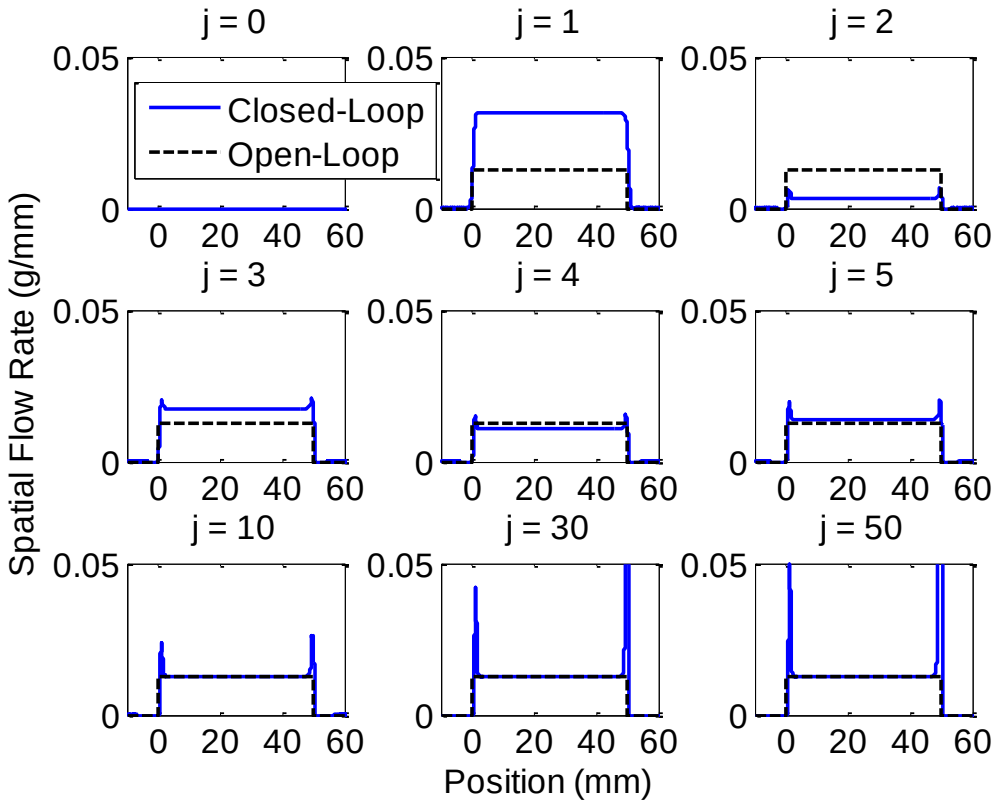

Figure 5.4. Spatial flow rate λ signals at layers j = 0, 1, 2, 3, 4, 5, 10, 30, and 50 for open-loop and closed-loop control simulation of Scenario 1.

The large control signals seen on layers j = 30 and j = 50 near the end of the deposition are a result of the mismatch between the linearized controller and the nonlinear system. The actual powder catchment efficiency in the region where the control is largest is decaying to zero in the vertical direction at a rate proportional to α_{max}.

The controller, which is designed for the linear system and provides constant catchment everywhere along the track, commands a large spatial flow rate in an attempt to deposit material in a location that is not feasible in the physical process.

As the layer index increases, the open-loop system has a constant error of approximately 0.30 mm between $x_s = 0$ and $x_e = 50$ mm while the tails of the deposit, those areas near the beginning and end of the commanded deposition, increase and reach a maximum of 10.90 mm at the beginning of the deposit by $j = 50$. Alternatively, the closed-loop system error decays to an error of approximately 0.03 mm between $x_s = 0$ and $x_e = 50$ mm by layer $j = 3$ and $e = 2.20\times10^{-7}$ mm when $j = 50$ with smaller tails – a maximum of 7.20 mm at the beginning of the deposit when $j = 50$. Error still exists at the tails of the closed-loop deposition for two reasons. First, because the compensator is designed with only a single layer-to-layer integrator, the steady-state in-layer error is finite, but non-zero, when fabricating layers of constant height. Secondly, because the compensator is designed based on the linearized process, negative control signals are sometimes generated. Since negative control corresponds to a negative spatial flow rate, or alternatively a positive material removal rate, and the LMD process is purely additive, these control signals are not feasible. Therefore, because the closed-loop layer-to-layer dynamics contain some overshoot, and the closed-loop nonlinear process contains effects not accounted for in the compensator design, over build at the edges remains, and possibly grows, as it cannot be removed with the additive process.

As demonstrated in Section 3.6.2, the open-loop process is sensitive to substrate features, e.g. Figure 3.19. In the second scenario, a tall feature is built over a pocket of

depth 0.60 mm, twice that of the desired bead height δd_S, and 25 mm long below the zero-datum of the to-be-deposited feature. The initial part standoff distance profile is

$$d_P(x,0) = d_{P,e} + 2\delta d_S\left(f_{ref}(x) * \text{rect}(12.5, 37.5)\right) \tag{86}$$

and the reference signal is

$$r(x, j) = j\left(\delta d_S - \xi(x)\right) + d_{P,e} \tag{87}$$

where ξ is given in (83)

$$\xi(x) = \delta d_S\left(f_{ref}(x) * \text{rect}(x_s, x_e)\right) \tag{88}$$

and

$$f_{ref}(x) = \begin{cases} 1-|x| & -1 \le x \le 1 \\ 0 & \text{otherwise} \end{cases} \tag{89}$$

$$\text{rect}(x_1, x_2) = \begin{cases} 1 & x_1 \le x \le x_2 \\ 0 & \text{otherwise} \end{cases}. \tag{90}$$

Using the relationship (50), Figure 5.5 shows the resulting open-loop simulation height signals at layers j = 0, 1, 2, 3, 4, 5, 10, 30, and 50. For each layer, constant spatial flow rate $\lambda_e = 1.26\times10^{-2}$ g/mm is commanded to start at x_s = 0 and end at x_e = 50 mm.

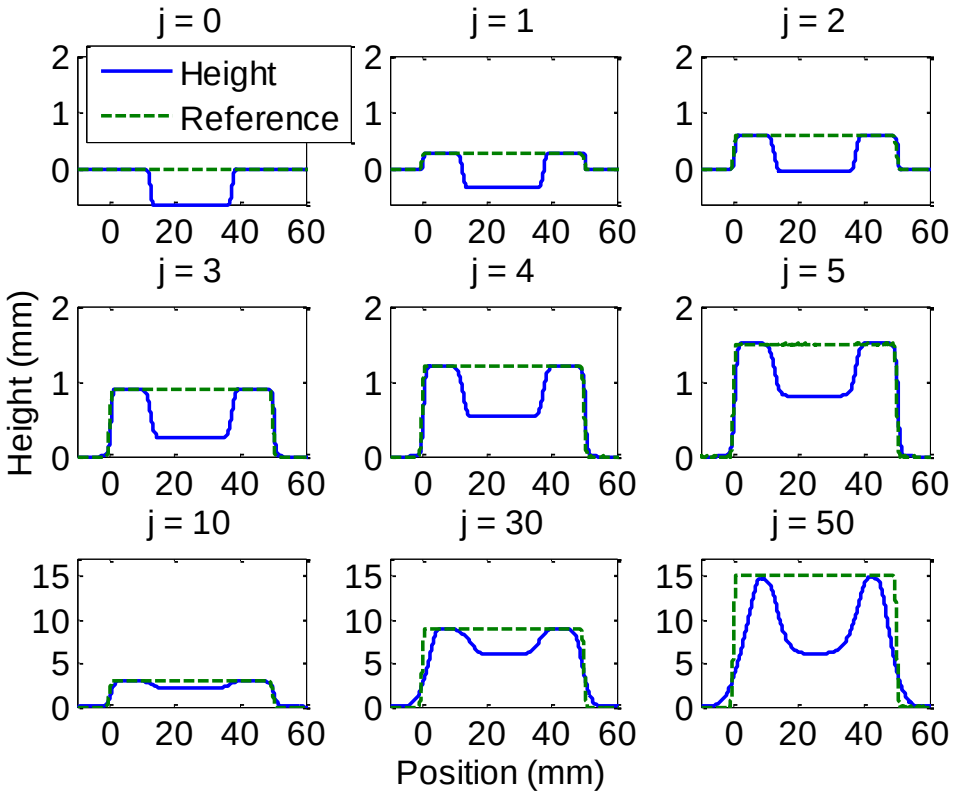

Figure 5.5. Height h and reference r signals at j = 0, 1, 2, 3, 4, 5, 10, 30, and 50 for open-loop ($\lambda_0 = 1.26\times10^{-2}$ g/mm) simulation of Scenario 2.

Because the powder catchment efficiency spans the pocket feature in the vertical direction, the nonlinear process operates in two regimes. A stable regime, mentioned in Section 4, occurs for sections of the build that starts on top of the substrate. However, within the pocket when d_P = 11.07 mm $\kappa_2 = -2.359\times10^{-2}$ and the process is is operating within a locally unstable regime. Because the lower section receives less powder than the taller sections, the part standoff distance increases from the desired value $d_{P,e}$ = 10.47 mm set to the zero-datum (top of the substrate) of the part and the small pocket feature is propagated from layer-to-layer and grows in magnitude. Examining the individual subplots in Figure 5.5, it can be seen that by layer j = 50, the small initial defect has been

magnified by a factor of 14.8. The actual open-loop process would not be allowed to continue as far as layer $j = 50$ and operator intervention would be required to choose different operating conditions such that the small initial height defect does not continue to grow.

Alternatively, using the designed controller, the closed-loop system shows little sensitivity to the small height defect on the initial layer and tracks the uniform part standoff distance reference prescribed by (87). By layer $j = 3$, the defect no longer affects the remaining deposition. The closed-loop height and reference signals at layers $j = 0$, 1, 2, 3, 4, 5, 10, 30, and 50 are shown in Figure 5.6. The controlled deposition exhibits significant improvement over the open-loop deposition with an error of 2.03×10^{-7} mm at $x = 25$ mm. However, some error still exists on the side of the depositions. This phenomena is mainly attributable to both the locally linear nature of the model from which the controller was synthesized and the redistribution of material in the physical process. A secondary cause of this effect lies in the fact that the forward loop of the process only contains a single layer-to-layer integrator while the reference is a ramp signal. Therefore, non-zero steady state error is expected.

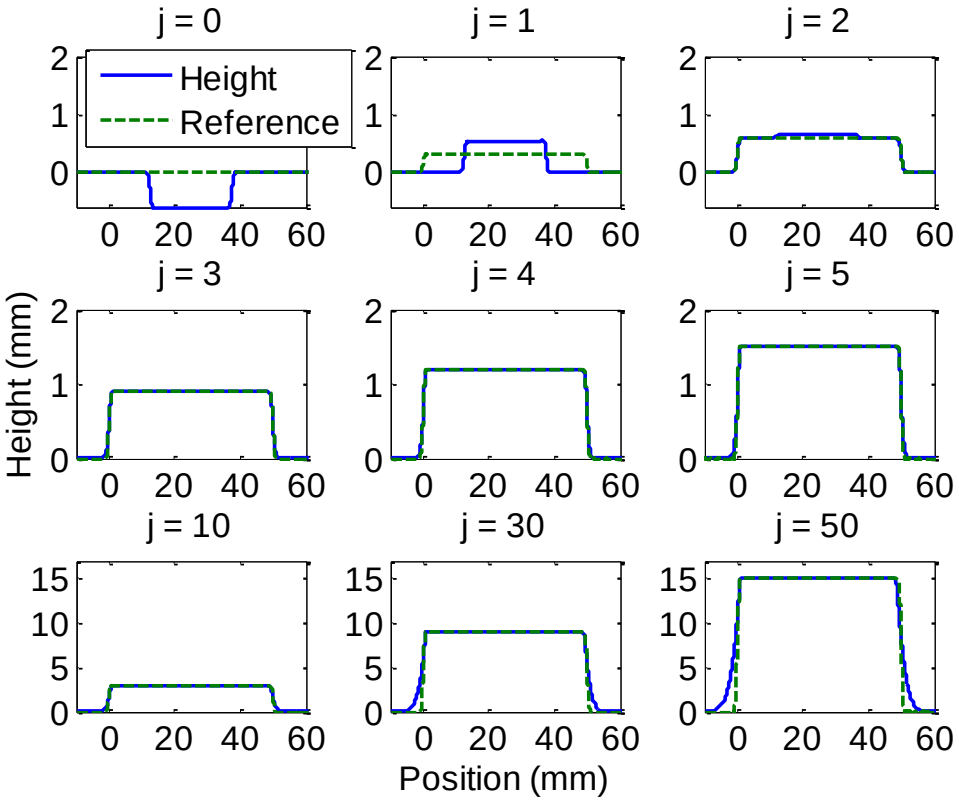

Figure 5.6. Height h and reference r signals at j = 0, 1, 2, 3, 4, 5, 10, 30, and 50 for closed-loop control of Scenario 2.

The layer-to-layer spatial domain control signals, which are saturated below at zero, are shown in Figure 5.7 at the corresponding layers in Figure 5.6. On layer j = 1, the controller commands a large spatial flow rate in the region where the defect occurs, due to the error between the initial reference and height profiles. As the layer index increases, the portion of the control signals between x = 0 and x = 50 mm converge to equilibrium value of spatial flow rate. However, in order to track the corners of the reference, sharp increases in spatial flow rate are needed near x = 0 and x = 50 mm.

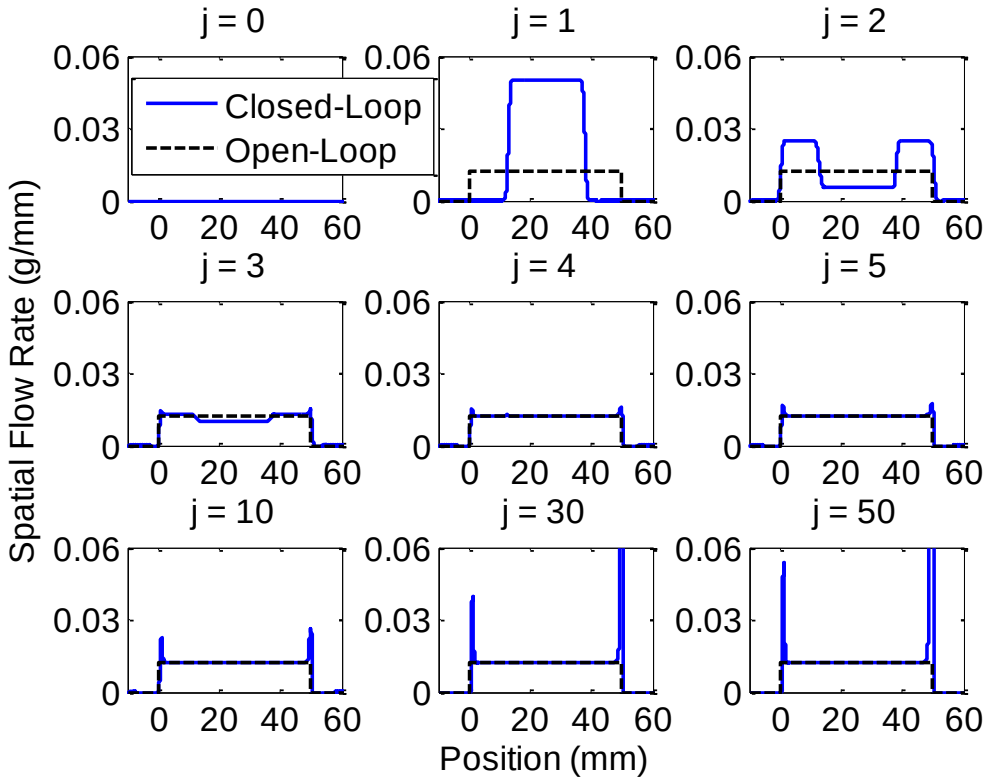

Figure 5.7. Spatial flow rate λ signals at layers j = 0, 1, 2, 3, 4, 5, 10, 30, and 50 for open-loop and closed-loop control simulation of Scenario 2.

6. TWO-DIMENSIONAL LAYER-TO-LAYER FEEDFORWARD/FEEDBACK CONTROL

Consider now the two-dimensional block diagram shown in Figure 6.1. For the feedforward/feedback layer-to-layer control, model predictive control (MPC) is used. In MPC, a model of the plant, the "Estimator" in Figure 6.1, is used to predict future values of the output. Then, an optimization problem is solved to minimize a cost function. The output of the optimization is then the control action to be applied to the actual plant. The resulting measurement of the plant is then used as an initial condition for the "Estimator" and the loop is closed.

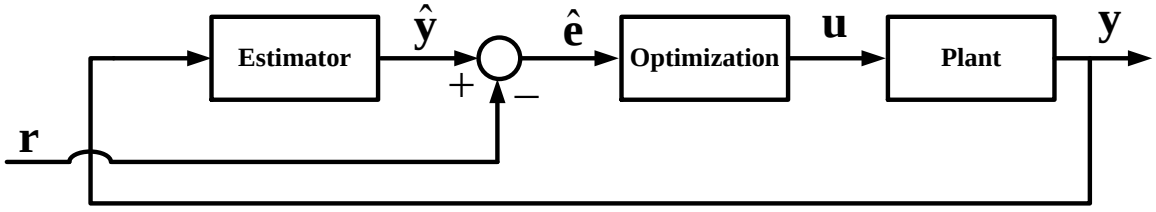

Figure 6.1. Two-dimensional block diagram for combination feedforward/feedback layer-to-layer control.

Again, consider the general LMD process description (41), with signals and operators defined as before and assumptions A1-A3 Further, it is assumed the nonlinearity f in (41), with the internal states partitioned as $\boldsymbol{\upsilon}(x,j)=\left[\boldsymbol{\upsilon}_{\mathbf{u}}(x,j)\quad \boldsymbol{\upsilon}_{\mathbf{y}}(x,j)\right]^T=\left[g_{\mathbf{u}}(w)\mathbf{u}(x,j)\quad \mathbf{D}\mathbf{y}(x,j-1)\right]^T$, can be written as

$$f\left(\boldsymbol{\upsilon}(x,j)\right)=\begin{bmatrix}\vartheta_1\left(\boldsymbol{\upsilon}_{\mathbf{y}}(x,j-1)\right)\boldsymbol{\upsilon}_{\mathbf{u}}(x,j)\\ \boldsymbol{\upsilon}_{\mathbf{y}}(x,j-1)+\mathbf{b}\end{bmatrix} \tag{91}$$

where ϑ_1 is a static nonlinear function and $\mathbf{b}$ is a constant.

6.1. FEEDBACK LINEARIZATION

The repetitive process in (41) is nonlinear in the internal states $\boldsymbol{\upsilon}$ as they appear as an argument to the static nonlinearity. In order to make the control design methodology more tractable, it is advantageous to have a linear repetitive process. Instead of attempting to linearize the entire model, the notion of feedback linearization is used to transform the original nonlinear system description into a linear form.

Definition 6.1: The static nonlinearity in (91) is said to be feedback linearized if there exists a set of inputs of the form $\boldsymbol{\upsilon}_{\mathbf{u}}(x,j)=\boldsymbol{\varphi}_1\left(\boldsymbol{\upsilon}_{\mathbf{y}}(x,j)\right)+\boldsymbol{\varphi}_2\left(\boldsymbol{\upsilon}_{\mathbf{y}}(x,j)\right)\mathbf{v}(x,j)$ such that the static nonlinearity f can be written as

$$f\left(\boldsymbol{\upsilon}(x,j)\right)=\begin{bmatrix}\mathbf{H}\mathbf{v}(x,j)\\ \boldsymbol{\upsilon}_{\mathbf{y}}(x,j)+\mathbf{b}\end{bmatrix} \tag{92}$$

where $\mathbf{H}\in\mathbb{R}^{p\times m}$ is a constant matrix and $\mathbf{v}$ is an auxiliary internal state. Individual elements of $\mathbf{H}$ are referenced as η_{ik} where a is element in the $_i^{\text{th}}$ row and k^{th} column of $\mathbf{H}$.

Suppose there exists an input signal $\boldsymbol{\upsilon}_2$ such that the static nonlinearity in (41) is feedback linearized. Then, the feedback linearized two-dimensional process is given as

$$\mathbf{y}(x, j) = G_2(s)\begin{bmatrix} \mathbf{H}\mathbf{v}(x, j) \\ \boldsymbol{\upsilon}_{\mathbf{y}}(x, j) + \mathbf{b} \end{bmatrix}. \tag{93}$$

6.2. LIFTED REPRESENTATION AND ERROR DYNAMICS

In operation of AM processes, and specifically the LMD process, the in-layer domain is finite. On each layer, the process is commanded to begin at a starting location x_s and finish at an ending location x_e. This property of the operation of AM process allows the transformation of the two-dimensional feedback linearized process (93) into an equivalent multiple input, multiple output (MIMO) one-dimensional system. In order to consider the system in (93) as a finite dimensional MIMO system, let the in-layer domain be discretized as $x = k\Delta x$, where k is the sample index and Δx is the spatial sampling period (mm). Suppose the spatial domain has support on the interval $k \in [-N, N]$ where $N \in \mathbb{Z}_+$. Then, after discretization and partitioning the in-layer dynamic operator $G_2[z] = \begin{bmatrix} g_{21}[z] & g_{22}[z] \end{bmatrix}$, the linearized process is

$$\mathbf{y}[k, j] = g_{21}[z]\mathbf{H}\mathbf{v}[k, j] + g_{22}[z]\left(\mathbf{D}\mathbf{y}[k, j-1] + \mathbf{b}\right). \tag{94}$$

where the in-layer linear dynamic operator has been discretized and z is the in-layer shift operator $z\mathbf{y}[k, j] = \mathbf{y}[k+1, j]$. Using a lifted representation [Bristow 2006], the spatially

discrete two-dimensional system (94) can be converted into a MIMO system. Define the lifted vectors

$$\begin{aligned}\mathbf{N}_j &= \begin{bmatrix}\mathbf{v}^T[-N, j] & \mathbf{v}^T[-N+1, j] & \cdots & \mathbf{v}^T[N, j]\end{bmatrix}^T \in \mathbb{R}^{2Nm\times 1} \\ \mathbf{Y}_j &= \begin{bmatrix}\mathbf{y}^T[-N, j] & \mathbf{y}^T[-N+1, j] & \cdots & \mathbf{y}^T[N, j]\end{bmatrix}^T \in \mathbb{R}^{2Nn\times 1}\end{aligned}, \tag{95}$$

the lifted constant static terms $\bar{\mathbf{H}}$, $\bar{\mathbf{D}}$, and $\bar{\mathbf{b}}$

$$\begin{aligned}\bar{\mathbf{H}} &= \operatorname{diag}(\mathbf{H}) \in \mathbb{R}^{2Nn\times 2Nm} \\ \bar{\mathbf{b}} &= \operatorname{diag}(\mathbf{b}) \in \mathbb{R}^{2Nn\times 2Nn} \\ \bar{\mathbf{D}} &= \operatorname{diag}(\mathbf{D})\end{aligned} \tag{96}$$

where diag(•) places the arguments along the main diagonal of an appropriately sized matrix with zeros everywhere off of the main diagonal, and the lifted representations of the partitions of G_2, as

$$\begin{aligned}\mathbf{g}_{21} &= \begin{bmatrix} g_{21}[0] & g_{21}[-1] & \cdots & 0 \\ g_{21}[1] & g_{21}[0] & \cdots & 0 \\ \vdots & \vdots & \ddots & \vdots \\ 0 & 0 & \cdots & g_{21}[0] \end{bmatrix} \in \mathbb{R}^{2Nn\times 2Np} \\ \mathbf{g}_{22} &= \begin{bmatrix} g_{22}[0] & g_{22}[-1] & \cdots & 0 \\ g_{22}[1] & g_{22}[0] & \cdots & 0 \\ \vdots & \vdots & \ddots & \vdots \\ 0 & 0 & \cdots & g_{22}[0] \end{bmatrix} \in \mathbb{R}^{2Nn\times 2Np}\end{aligned}. \tag{97}$$

Finally, defining $\mathbf{G_H} = \mathbf{g}_{21}\bar{\mathbf{H}}$ and $\mathbf{G_Y} = \mathbf{g}_{22}\mathbf{D}$, re-writing (94) in the lifted representation gives,

$$\mathbf{Y}_j = \mathbf{G_H}\mathbf{N}_j + \mathbf{G_Y}\mathbf{Y}_{j-1} + \bar{\mathbf{b}} \tag{98}$$

and is an equivalent MIMO discrete system of (94). In order to ensure offset-free tracking and to reject layer-to-layer disturbances, integral action is desired. Following [Pannocchia 2005, Maeder 2009], integral action can be incorporated by penalizing the incremental output. Therefore, define the incremental lifted input and output as $\Delta\mathbf{N}_j = \mathbf{N}_j - \mathbf{N}_{j-1}$ and $\Delta\mathbf{Y}_j = \mathbf{Y}_j - \mathbf{Y}_{j-1}$, respectively. Combining the two terms in (98) and forming the incremental lifted dynamics gives,

$$\Delta\mathbf{Y}_j = \mathbf{G_H}\Delta\mathbf{N}_j + \mathbf{G_Y}\Delta\mathbf{Y}_{j-1} \tag{99}$$

As in Section 5.1, let **r** be a layer-to-layer reference signal. The lifted representation of **r** is denoted as **R** and is formed as in (95). The layer-to-layer tracking error again is $\mathbf{E}_j = \mathbf{Y}_j - \mathbf{R}_j$. The tracking error dynamics are then

$$\mathbf{E}_j = \mathbf{E}_{j-1} + \mathbf{G_H}\Delta\mathbf{N}_j + \mathbf{G_Y}\Delta\mathbf{Y}_{j-1} - \Delta\mathbf{R}_j \tag{100}$$

Compactly, (99) and (100) are

$$\underbrace{\begin{bmatrix}\mathbf{E}_j\\ \Delta\mathbf{Y}_j\end{bmatrix}}_{\mathbf{x}_j}=\underbrace{\begin{bmatrix}\mathbf{I} & \mathbf{G}_\mathbf{H}\\ 0 & \mathbf{G}_\mathbf{H}\end{bmatrix}}_{\mathcal{A}}\begin{bmatrix}\mathbf{E}_{j-1}\\ \Delta\mathbf{Y}_{j-1}\end{bmatrix}+\underbrace{\begin{bmatrix}\mathbf{G}_\mathbf{Y}\\ \mathbf{G}_\mathbf{Y}\end{bmatrix}}_{\mathcal{B}}\Delta\mathbf{N}_j+\underbrace{\begin{bmatrix}-\mathbf{I}\\ 0\end{bmatrix}}_{\mathcal{I}}\Delta\mathbf{R}_j\,. \tag{101}$$

6.3. REPETITIVE PROCESS MODEL PREDICTIVE CONTROL

In AM process fabrications, the total number of layers to build is typically large, but is always finite. Further, the class of disturbances or references in the lifted framework presented above for AM processes generally does not admit a tractable generating autonomous exosystem, e.g., a simple ramp or sinusoidal layer-to-layer reference. Therefore, it is not feasible to design an optimal controller that attempts to predict the entire build sequence, nor is it appropriate to use an infinite-horizon optimal controller with an internal model for tracking performance. Here, a model predictive-type optimal controller based on the repetitive process model (101) is developed to control AM processes. Let the cost functional be quadratic,

$$V_{j|N_\varepsilon}=\sum_{i=0}^{N_\varepsilon}\mathbf{x}_{j+i-1}^T\mathbf{Q}\mathbf{x}_{j+i-1}+\bar{\mathbf{U}}_{j+i-1}^T\mathbf{S}\bar{\mathbf{U}}_{j+i-1} \tag{102}$$

where $V_{j|N_\varepsilon}$ is the cost associated with prediction from the current layer j to the prediction horizon N_ε, $\mathbf{Q_f}$, $\mathbf{Q}$, and $\mathbf{S}$ are positive semi-definite, symmetric weighting error matrices on the final prediction errors, the intermediate layer errors, and the control action, respectively. Input constraints are imposed in order to ensure physically realizable control signals are generated from the optimization of (102),

$$\mathbf{M}\bar{\mathbf{U}}_{j+i-1}\geq\mathbf{b},\ i=1,\ldots,N_\varepsilon \tag{103}$$

where **M** is a constant matrix and **b** is a constant vector. Here, as is typical with model predictive schemes, only the first control signal, $\bar{\mathbf{U}}^*_{j+1}$, from the computed optimal control sequence is applied to the system.

Remark 6.1: The closed-loop operation of the finite horizon optimal control process is as follows. The optimal control signal $\bar{\mathbf{U}}^*_{j+1}$, which is the entire current layer control sequence, is applied to the system. After the control signal is implemented, the process output $\mathbf{Y}_j$ is measured and the tracking error $\boldsymbol{\varepsilon}_j$ is calculated. The current measured tracking error is then used to calculate again the optimal control signal to be applied to the system. The optimization procedure is carried out between layers.

Remark 6.2: The computational cost of the finite horizon optimal control formulation presented varies significantly with the number of states in the system and the sampling rate chosen over the in-layer interval. Because the optimization is carried out between layers, the calculation speed is not of supreme importance and it may be possible to reduce the computational burden by leveraging the structure of the matrices in (97). Here, however, no further investigation into the computational requirements or cost is made.

6.4. APPLICATION TO THE LMD PROCESS

Recall the general LMD process model given in (41) and the operator specific to the LMD process given in (55)-(57). The nonlinearity is written as

$$f\left(\boldsymbol{\upsilon}(x,j)\right)=\begin{bmatrix}\vartheta_1\left(\boldsymbol{\upsilon}_{\mathbf{y}}(x,j)\right)\boldsymbol{\upsilon}_{\mathbf{u}}(x,j)\\ \boldsymbol{\upsilon}_{\mathbf{y}}(x,j)+\mathbf{b}\end{bmatrix}$$
$$=\begin{bmatrix}-b^{-1}\varsigma f_{\mu}\left(d_P(x,j-1)\right)\lambda(x,j-1)\\ d_P(x,j-1)+\delta d_S\end{bmatrix} \tag{104}$$

where $\vartheta_1\left(\boldsymbol{\upsilon}_{\mathbf{y}}(x,j)\right)=-b^{-1}\varsigma f_{\mu}\left(d_P(x,j-1)\right)$ and $\mathbf{b}=\delta d_S$.

In LMD processes, it is typical to have very good knowledge of the powder catchment efficiency function f_{μ} as its structure is typically known and is easily measureable [Sammons 2015]. Therefore, a feedback linearizing set of inputs $\boldsymbol{\upsilon}_{\mathbf{u}}(x,j)$ for the LMD process model is

$$\boldsymbol{\upsilon}_{\mathbf{u}}(x,j)=\frac{\mu_D}{-b^{-1}\varsigma f_{\mu}\left(d_P(x,j-1)\right)}\mathbf{v}(x,j) \tag{105}$$

where μ_D is a tuning parameter. The two-dimensional LMD process description is then written as (93) with $\mathbf{H} = \mu_D$ and is

$$d_P(x,j)=\mu_D\mathbf{v}(x,j)*f_s(x)+\left(d_P(x,j-1)+\delta d_S\right)*f_r(x). \tag{106}$$

As stated above in Section 5.2.2, the LMD process in-layer domain is finite. Thus, let the in-layer domain be discretized as $x = k\Delta x$ and the spatial domain have finite support on the interval $k\in[-N,N]$ where $N\in\mathbb{Z}_+$. The discretized feedback linearized process is then,

$$d_P[k,j] = F_s[z]\mu_D v[k,j] + F_r[z]\left(d_P[k,j-1] + \delta d_S\right). \tag{107}$$

where $g_{21} = F_s$ and $g_{22} = F_r$ in (94). With the lifted vectors defined in (95) and operators $\bar{\mathbf{H}}$, $\bar{\mathbf{b}}$, $\bar{\mathbf{D}}$, $\mathbf{g}_{21}$, and $\mathbf{g}_{22}$ defined in (96) and (97) are

$$\mathbf{g}_{21} = \begin{bmatrix} f_s[0] & f_s[-1] & \cdots & 0 \\ f_s[1] & f_s[0] & \cdots & 0 \\ \vdots & \vdots & \ddots & \vdots \\ 0 & 0 & \cdots & f_s[0] \end{bmatrix}, \mathbf{g}_{22} = \begin{bmatrix} f_r[0] & f_r[-1] & \cdots & 0 \\ f_r[1] & f_r[0] & \cdots & 0 \\ \vdots & \vdots & \ddots & \vdots \\ 0 & 0 & \cdots & f_r[0] \end{bmatrix},. \tag{108}$$
$$\bar{\mathbf{H}} = \text{diag}(\mu_D), \bar{\mathbf{b}} = \text{diag}(\delta d_S), \bar{\mathbf{D}} = \mathbf{I}$$

the lifted representation, with $\mathbf{G_H}$ and $\mathbf{G_Y}$ defined in Section 6.2, is

$$\mathbf{Y}_j = \mathbf{G_H}\mathbf{N}_j + \mathbf{G_Y}\mathbf{Y}_{j-1} + \bar{\mathbf{b}}. \tag{109}$$

The error dynamics are defined as in (100) and the augmented lifted system is given in (101).

Remark 6.3: The matrices $\mathbf{g}_{21}$ and $\mathbf{g}_{22}$ in (108) are given as square matrices. Because they represent convolution operations, edge effects may occur. To help minimize those effects, the output vector **Y** can be defined over a longer interval than the control signals **N**. In doing so, any transients are allowed to go to zero and therefore not be propagated between layers. In this case, $\mathbf{g}_{21}$ and $\mathbf{g}_{22}$ would be non-square.

Open- and Closed-Loop Simulation. As before, the system used is the Optomec MR-7 LENS system. The model parameters are given in Table 4.1. In each of the following simulation scenarios, let the reference be,

$$\mathbf{R}_j = \begin{cases} \mathbf{F}_{ref}\left[0.3j\mathbf{p}[0,50]\right] & j < 4 \\ \mathbf{r}_{j-1} + \mathbf{F}_{ref}\,0.3\left(\mathbf{p}[0,50] - \mathbf{p}[15,35]\right) & j = 4 \\ \mathbf{r}_{j-1} + \mathbf{F}_{ref}\,0.3\left(\mathbf{p}[0,50] - \mathbf{p}[10,40]\right) & j \geq 5 \end{cases} \tag{110}$$

where $\mathbf{F}_{ref}$ is a lifted convolution matrix, i.e., the same structure as the matrices in (108), whose kernel is given by (89) with l_r = 0.5 mm, and $\mathbf{p}$ is a square pulse defined as

$$\mathbf{p}[k_1, k_2] = \begin{cases} 1 & k_1 \leq k \leq k_2 \\ 0 & \text{otherwise} \end{cases} \tag{111}$$

The reference trajectory in (110) is shown in Figure 6.2 for every second layer between j = 1 and j = 25. The trajectory generated by (110) poses a problem for the purely layer-to-layer feedback control methodology presented in Section 5.1 because the trajectory changes rapidly from one layer to the next.

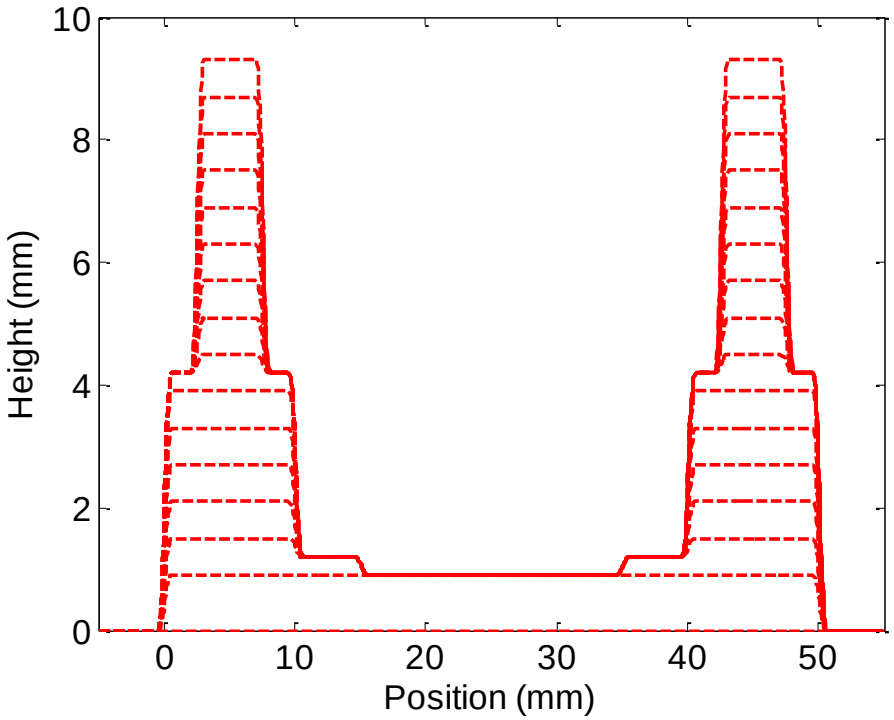

Figure 6.2. Height reference trajectory.

For each of the simulation scenarios, the total number of layers to build is $L = 25$. Further, a constant multiplicative unmeasured disturbance is introduced on the input channel such that

$$\hat{\mathbf{N}}_j = 0.95\mathbf{N}_j^* \tag{112}$$

where $\hat{\mathbf{N}}$ is the control applied to the system. Because the powder flow rate in LMD processes is dependent on several variables including the carrier gas flow rate, the powder particle size, and the powder feeder motor speed, the disturbance in (112) emulates a mismatch in the commanded and actual powder flow rate in LMD processes. Beginning at layer $j = 0$, the optimal control is calculated and the nonlinear system is

simulated. Then, the error between the simulated height and reference is calculated and fed back into the optimal controller. This process is repeated at each layer until the final layer is reached.

The baseline open-loop height profile is shown in Figure 6.3 along with the final reference signal.

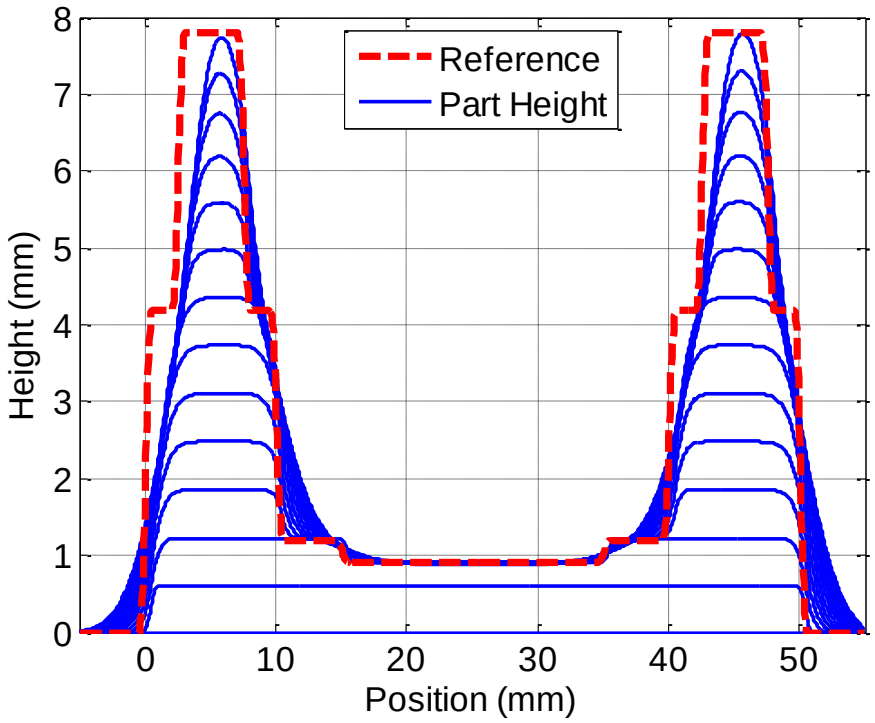

Figure 6.3. Open-loop height profile.

In the open-loop case, the process is not feedback linearized and is carried out with a constant *substrate standoff distance* as opposed to a constant *part standoff distance*, which is the mode for the feedback linearized process. As can be observed in Figure 2, the open-loop performance is relatively poor. This is caused by two major

phenomena. First, because there is no layer-to-layer feedback and the control signal applied to the system is perturbed by the constant multiplicative disturbance, the part standoff distance d_P grows each layer, moving the process from a high powder catchment efficiency to a low powder catchment efficiency. Secondly, because of the smoothing effects of the re-melt dynamics f_r, the sharp features in the reference cannot be achieved without a better choice of spatial flow rate.

In the simulation study, the effect of weighting matrices, $\mathbf{Q_f}$, $\mathbf{Q}$, and $\mathbf{S}$ in (102), will be investigated in the purely additive process, i.e., the control signals are constrained such that the actual original control signal is saturated to zero,

$$-\mathbf{N}_j^* \geq 0 \tag{113}$$

where $\mathbf{M} = -\mathbf{I}$ and $\mathbf{b} = -\mathbf{U_r}$ and $\mathbf{U_r}$ is the lifted representation of $\mathbf{u_r}$. While the framework described in the previous section provides for a wide variety of weighting schemes, i.e., layer- and spatially-varying weights, here the weighting matrices are chosen as layer-to-layer constant but with different levels for the error state $\mathbf{E}$ and the integrator state $\mathbf{\Omega}$. The weighting matrices are selected to be of the form

$$\mathbf{Q} = \begin{bmatrix} q\mathbf{I} & \mathbf{0} \\ \mathbf{0} & q_\Omega \mathbf{I} \end{bmatrix}, \mathbf{Q_f} = \begin{bmatrix} q_f \mathbf{I} & \mathbf{0} \\ \mathbf{0} & q_{\Omega,f} \mathbf{I} \end{bmatrix}, \mathbf{S} = s\mathbf{I} \tag{114}$$

where q, q_Ω, q_f, $q_{\Omega,f}$, and s are scalar weights on the current error, the current error integration, the final error, the final error integration, and the control action, respectively. Three total weighting schemes are chosen and are listed in Table 6.1. For each of the

weight selections, the prediction horizon is set to N_{ε} = 2 in order to reduce the computational cost.

Table 6.1. Weighting matrix selections.

	Case 1	**Case 2**	**Case 3**
Current Error Weight, q	1	1	500
Current Error Integration Weight, q_{Ω}	100	100	50×10^{3}
Control Effort Weight, s	1	100	.01
Final Error Weight, q_f	500	100	5000
Final Error Integration Weight, $q_{\Omega,f}$	50×10^{3}	10×10^{3}	500×10^{3}

Figure 6.4 shows the part height of the closed-loop simulated depositions at layers j = 1, 5, 10, 15, 20, and 25 as well as the reference signals. At the beginning of each deposit, the tracking performance is improved over the open-loop deposit and there is not a discernible difference between the weighting cases. However, as layer number increases, the tracking performance degrades for Cases 1 and 2 because the control effort weighting is significant with respect to both the current error and integral error and the final error and integral weightings. Additionally, because the control signals are saturated to zero, edge tracking, those regions where the reference signal transitions rapidly, is degraded. However, because saturation results in overbuild in these regions, a post-processing operation can be used to remove the excess material easier than attempting to add more material as in the open-loop case.

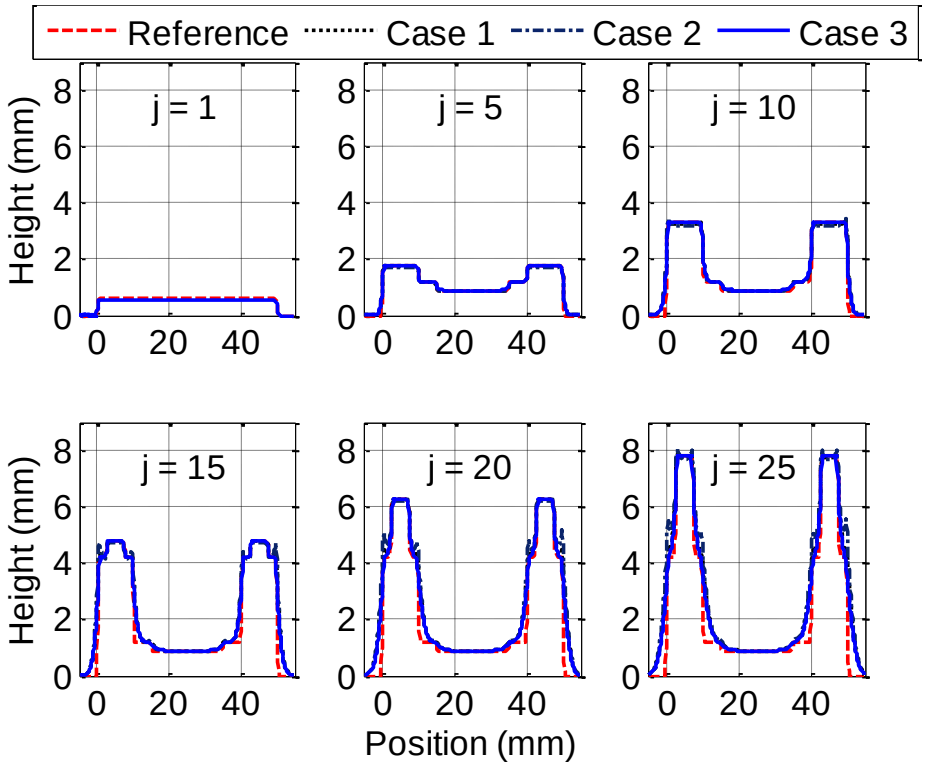

Figure 6.4. Part height for simulation Case 1 at every second layer from $j = 2$ to $j = 25$ and reference trajectory at $j = 25$.

For Case 3, tracking performance remains relatively constant throughout the build and the tracking error is largely attributable to the saturation of the control signals. A detail view of the spatial locations where the reference signal transitions rapidly is shown in Figure 6.5. As mentioned above, Cases 1 and 2 experience tracking performance degradation at higher layer numbers while Case 3 does not appear to experience the same phenomenon – except in that the control signals are saturated to zero.

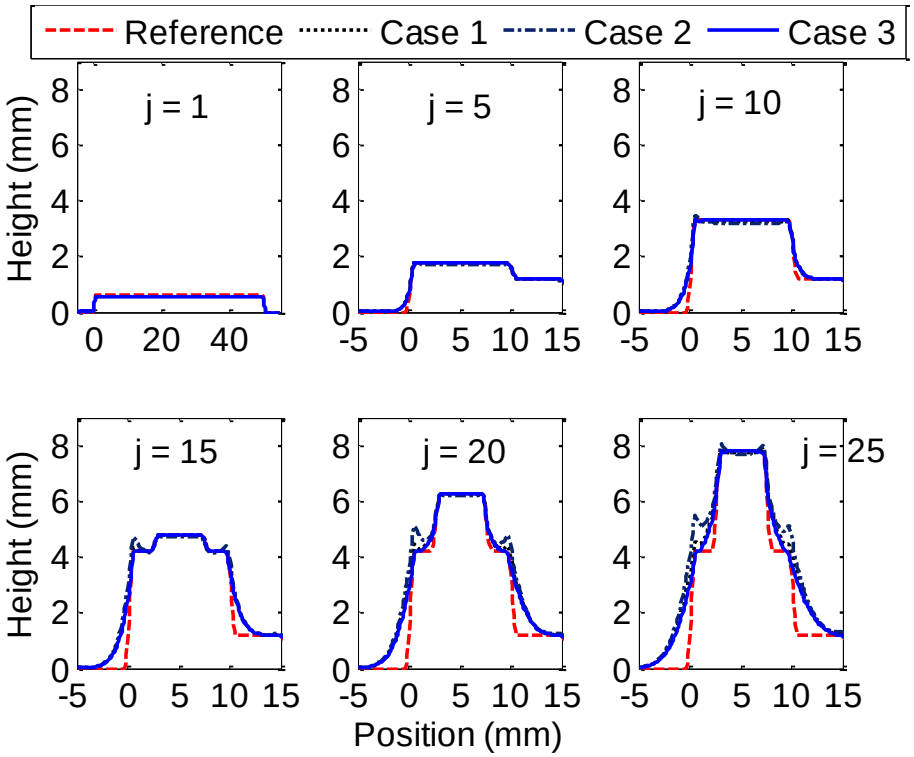

Figure 6.5. Part height for simulation Case 2 at every second layer from $j = 2$ to $j = 25$ and reference trajectory at $j = 25$.

7. SUMMARY AND CONCLUSIONS

A major obstacle in the automation of AM processes is the lack of proper process control. Because AM processes are repetitive in nature, the dependency of the formation of the current layer on the previous layer's morphology can cause significant problems when attempting to control the process using only in-layer feedback control. To enable the use of repetitive process controllers, where the control methods explicitly account for the layer-to-layer dynamics, models incorporating both the in-layer and the layer-to-layer dynamics are needed. In this work a framework for modeling and identifying AM processes as repetitive processes was given. The framework includes the dominant in-layer and layer-to-layer dynamics, resulting in a two-dimensional dynamic process description and a methodology for identifying the model parameters. The model structure, a linear layer-to-layer dynamic element cascaded into a static nonlinearity cascaded into a linear in-layer dynamic element, provides a compact, yet general, framework for modeling AM processes and aids in choosing appropriate process model parameter identification experiments. The identification framework provides a method for choosing appropriate signals for straightforward identification of model parameters in the static nonlinearity and in-layer dynamic process. Extension of the methodology could treat processes whose layer-to-layer dynamics are characterized by unknown parameters. The specific experimental application to the LMD process indicates that the proposed model can describe the process dynamics well, both quantitatively and qualitatively.

Using the repetitive process model developed in Section 2 of this dissertation for AM processes, a criterion based on one-dimensional discrete-time stability requirements is developed to determine layer-to-layer stability properties. Then, posing the two-

dimensional dynamics inherent in AM processes as a two-dimensional analog of a conventional discrete-time system, a method for designing a layer-to-layer stabilizing compensator is given. The stability criterion is calculated for a commercial LMD process near its maximum operating efficiency indicating the process operating point lies just within the stable region. A stabilizing layer-to-layer controller is then designed for the LMD process and two simulation studies are performed; a simulation to fabricate a part of uniform height with zero initial conditions and a simulation to fabricate a part of uniform height with non-zero initial conditions. The designed layer-to-layer compensator stabilizes the layer-to-layer process in both simulations, increases tracking performance over open-loop depositions, and is robust to initial conditions. However, some constant steady state error remains due to both the mismatch between the linear models on which the controller is based and the actual nonlinear system and the inclusion of only a single layer-to-layer integrator in the process. More sophisticated compensator designs may alleviate both of these issues.

To increase tracking performance over the layer-to-layer feedback controller designed in Section 5, the general AM repetitive process model is used to formulate a Finite Horizon Optimal control problem where tracking error and the integral of tracking error are regulated. Because the reference signal is assumed to be known *a priori*, the method presented here projects forward the modeled process and calculates an optimal control signal based on a quadratic cost function. Application to the LMD process model shows closed-loop tracking performance is sensitive to the effects of control effort weight and error integral weight. However, the closed-loop simulation results show improved

tracking performance and robustness to multiplicative uncertainty as compared to the open-loop process.

The general linear dynamic-static nonlinearity-linear dynamic model structure potentially admits a wide range of process descriptions, including those of many AM processes. Therefore, leveraging the structure and utilizing the methodology for designing and implementing layer-to-layer repetitive process controllers given in Sections 5 and 6 could allow for closed-loop repetitive process control of a wide variety of AM processes.

APPENDIX A

SOFTWARE

DMC MOTION COMMAND CODE

In this section of Appendix A, the DMC motion code used to generate the velocity profiles for the depositions used in Section 3 are given.

Powder Catchment Slope DMC

```
AC 2000000,2000000,2000000
DC 2000000,2000000,2000000
SP 600000,600000,60000
VA 3000000
VD 3000000
VS 45000
CAS
CSS
DP 0,0,0
VM XY
VP 240000,0
VE
SB 1
WT 20
BG S
AM
CB 1
VS 100000
VM XY
VP -240000,30000
VE
BG S
AM
UI 3
EN
```

PRBS Identification DMC

```
AC 2000000,2000000,2000000
DC 2000000,2000000,2000000
SP 10000,30000,4000
VA 3000000
VD 3000000
VS 10000
CAS
CSS
DP 0,0,0
T=1
SPEED = 0
VM
```

```
VP 180000,0
VE
BG S
WT  500
SB 1
WT 420
VS  30000
WT  157
VS  10000
WT  105
VS  30000
WT  157
VS  10000
WT  105
VS  30000
WT  315
VS  10000
WT  210
VS  30000
WT  472
VS  10000
WT  105
VS  30000
WT  157
VS  10000
WT  52
VS  30000
WT  157
VS  10000
WT  157
VS  30000
WT  315
VS  10000
WT  52
VS  30000
WT  630
VS  10000
WT  210
VS  30000
WT  157
VS  10000
WT  157
VS  30000
WT  157
VS  10000
WT  210
VS  30000
WT  157
VS  10000
WT  52
VS  30000
WT  787
VS  10000
WT  52
```

```
VS  30000
WT  945
VS  10000
WT  52
VS  30000
WT  157
VS  10000
WT  105
VS  30000
WT  157
VS  10000
WT  262
VS  30000
WT  315
VS  10000
WT  105
VS  30000
WT  157
VS  10000
WT  157
VS  30000
AM
CB 1
VS 60000
VM XY
VP -180000,12000
VE
BG S
AM
UI 3
EN
```

PRBS Validation DMC

```
AC 2000000,2000000,2000000
DC 2000000,2000000,2000000
SP 10000,30000,4000
VA 3000000
VD 3000000
VS 10000
CAS
CSS
DP 0,0,0
T=1
SPEED = 0
VM
VP 180000,0
VE
BG S
WT  500
SB 1
WT 591
```

```
VS 30000
WT 295
VS 10000
WT 98
VS 30000
WT 295
VS 10000
WT 98
VS 30000
WT 295
VS 10000
WT 197
VS 30000
WT 591
VS 10000
WT 197
VS 30000
WT 295
VS 10000
WT 295
VS 30000
WT 295
VS 10000
WT 197
VS 30000
WT 295
VS 10000
WT 98
VS 30000
WT 591
VS 10000
WT 98
VS 30000
WT 591
VS 10000
WT 295
VS 30000
WT 886
VS 10000
WT 98
VS 30000
WT 295
VS 10000
WT 394
VS 30000
WT 591
VS 10000
WT 98
VS 30000
WT 295
VS 10000
WT 98
VS 30000
WT 886
```

```
VS 10000
WT 197
VS 30000
WT 1181
VS 10000
WT 98
VS 30000
AM
CB 1
VS 60000
VM XY
VP -18,000,012,000
VE
BG S
AM
UI 3
EN
```

Pole Placement Procedure Matlab Code

```
clear all
warning('off','all')
%Model Parameters
%Optomec Trial 1; l0 = 0.49, delta = -0.01, l1 = 0.903, b0 = 1.03, m0 =
5.6
%Optomec Trial 1; l0 = 0.61, delta = -0.01, l1 = 1.213, b0 = 0.84, m0 =
9.2
%Unstable Process; l0 = 0.95, delta = -0.01, l1 = 0.200, b0 = 0.54, m0
=
%9.2, mu0 = 0.07

rho = 7.99e-6;                          %material density [kg/mm3]
l0 = 0.61;                              %characteristic melt pool length
[mm]
delta = -0.01;                          %shifting parameter [mm]
l1 = 1.100;                             %Re-melt char. length 1 [mm]
l2 = l1;                                %Re-melt char. length 2 [mm]
lref = 1;
w0 = 0.84;                              %characteristic melt pool width
[mm]
m0 = 9.2/(1000*60);                     %powder flow rate [kg/s]
v0 = 8.47;                              %frequency velocity parameter 1
alphaL = 50;                            %track length [mm]
a1 = 0.01*16.04;                        %catchment function parameter 1 [%]
a2 = 10.57;                             %c.f. parameter 2, max catchment
position [mm]
a3 = 2.04;                              %c.f. parameter 3, function width
param [mm]
dx = 0.002;                             %spatial simulation step size [mm]
dt = 0.004;                             %time step required for commanded
velocity [s]
M = 100;                                %total number of layers to build
OL = 0;
```

```
%Solution Points
dS0 = 0.3;                                  %Incremental Nozzle Shift
Sol. Input [mm]
dh0 = dS0;                                  %Bead Height Solution Point
[mm]
mu0 = 0.16;                                 %Catchment Sol. Point [kg/kg]
dP0 = a2 - a3*sqrt(-log(mu0/a1));           %Part standoff sol. point
[mm]
lambda0 = w0*dh0*rho/mu0;                   %Spatial Dep. Rate Sol. Point
[kg/mm]


%Gradients
c11 = -2*lambda0*a1*((dP0-a2)/a3)*Fmu(a1,a2,a3,dP0)/(w0*rho);
c2 = Fmu(a1,a2,a3,dP0)/(w0*rho);

fs = fshape(l0,delta,dx);                     %Shape filter
[xr,fr] = fremelt([l1 l2],dx);                %Re-melt filter
[xr1,fr1] = fremelt([lref lref],dx);          %Reference kernel

x = -250:dx:(300-dx);                       %position vector [mm]
L = max(size(x));                           %length of position vector

FsFFT = fft(fs,L);                          %FFT of the in-layer kernel
FrFFT = fft(fr,L);                          %FFT of the re-melt kernel

w = linspace(1e-6,1e2,L);                   %frequency vector [cycles/mm]

for i = 1:(max(size(w)))
    s = 2*pi*1i*w(i);
    Fs(i) = 2*(1-(1+s*l0)*exp(-l0*s))/(s^2*l0^2)*exp(-delta*s);
%Continuous domain frequency rep of in-layer kernel
    Fr(i) = 2/((l1+l2)*l1*s^2)*(exp(l1*s)-1) +
2/(s^2*l2*(l1+l2))*(exp(-l2*s)-1);       %Continuous domain frequency
rep of re-melt kernel
    GpFFT(i) = s*FrFFT(i) - c11*FsFFT(i);
%FFT of the layer-to-layer plant filter
    GcFFT(i) = c2*lambda0/dh0*FsFFT(i);
%FFT of the layer-to-layer controller filter
end

Gcmap = GcFFT;
Gpmap = GpFFT;

for ii = 1:max(size(w))
    %Layer-to-layer poles
    eig1(ii) = 1*1e-3;
    eig2(ii) = 1*1e-3;
    eig3(ii) = 0.5;

    %Layer-to-layer desired characteristic equation
    chard(ii,:) = conv(conv([1 eig1(ii)],[1 eig2(ii)]),[1 eig3(ii)]);
```

```
    %Calculation of the layer-to-layer pole, gain, and zero
    p1freq(ii) = -chard(ii,end)/(Gpmap(ii)*1);
    kfreq(ii) = (-chard(ii,2) - Gpmap(ii) - 1*(1+p1freq(ii)))/(-
Gcmap(ii)*1);
    z1freq(ii) = (chard(ii,3)/1 - p1freq(ii) -
Gpmap(ii)*(1+p1freq(ii)))/(-kfreq(ii)*Gcmap(ii));
end

%Spatial flow rate IC
lambda(:,1) = -1*ones(size(x,2),1);
lact(:,1) = (lambda0*(lambda(:,1)+1));

%Spatial domain reference and height IC
refC(:,1) = conv(fr1,[zeros(size(x(x<=0),2),1);ones(size(x(x>0 &
x<=(50)),2),1);zeros(size(x(x>(50)),2),1)]);
hC(:,1) = conv(fr1,[zeros(size(x(x<=0),2),1);0.0*ones(size(x(x>0 &
x<=12.5),2),1);0.00*ones(size(x(x>12.5 &
x<=37.5),2),1);0.0*ones(size(x(x>37.5 &
x<=50),2),1);zeros(size(x(x>50),2),1)]);

ref(:,1) = (refC((lref)/dx:end-lref/dx,1));
refS(:,1) = ref(:,1)*dh0;

dS(:,2) = (dP0)*ones(size(x,2),1);
hrNL(:,1) = hC((lref)/dx:end-lref/dx,1);

%Frequency domain reference and height IC
Rf(:,1) = (fft(ref(:,1),L) - fft(ones(size(x,2),1),L));
Rfs(:,1) = dh0*(Rf(:,1) + fft(ones(size(x,2),1),L));

Lfnl(:,1) = fft(lambda,L);

Enl(:,1) = fft(ref(:,1),L);

for j = 2:(M+1)

    ref(:,j) = (j)*(refC((lref)/dx:end-lref/dx,1));
    Rf(:,j) = (fft(ref(:,j),L) - fft(j*ones(size(x,2),1),L));

    %Frequency domain representation calculation of control signals
    if j == 2
        Lfnl(1:L/2,j) = ((1+p1freq(1:L/2))'.*Lfnl(1:L/2,j-1) +
kfreq(1:L/2)'.*Enl(1:L/2,j-1));

        Rfs(:,j) = dh0*(Rf(:,j) + fft(j*ones(size(x,2),1),L));%
    else
        Lfnl(1:L/2,j) = ((1+p1freq(1:L/2)').*(Lfnl(1:L/2,j-1)) -
p1freq(1:L/2)'.*(Lfnl(1:L/2,j-2)) + kfreq(1:L/2)'.*(Enl(1:L/2,j-1)) -
kfreq(1:L/2)'.*z1freq(1:L/2)'.*(Enl(1:L/2,j-2)));

        Rfs(:,j) = dh0*(Rf(:,j) + fft(j*ones(size(x,2),1),L));

    end
```

```
    %Frequency-to-Spatial Domain Transformation
    lNL(:,j) = ifft(Lfnl(:,j),'symmetric');
    lact(:,j) = (lambda0*(lNL(:,j)+1));
    lact(:,j) = lact(:,j) - lact(1,j);

    %Part Standoff Distance and Catchment Calculation
    dP(:,j) = dS(:,j) - (hrNL(:,j-1));
    mu(:,j) = Fmu(a1,a2,a3,dP(:,j));

    if OL == 1
        %Open-Loop Simulation
        lin(:,j) = [zeros(size(x(x<=0),2),1);lambda0.*ones(size(x(x>0 &
x<=50),2),1);zeros(size(x(x>50),2),1)];%
        dV(:,j) = lin(:,j);
        dpb(:,j) = (conv((fs),(dV(:,j).*mu(:,j))/rho/w0));
        dhb((x>=(delta) & x<=alphaL-(-l0)),j) = dpb((x>=(delta) &
x<=alphaL-(-l0)),j);
    else
        %Closed-Loop Simulation
        dV(:,j) = max(zeros(size(x,2),1),lact(1:end,2));
        dpb(:,j) = flipud(conv((fs),flipud(dV(:,j).*mu(:,j))/rho/w0));
        dhb(:,j) = dpb((l0+delta)/dx:(end+delta/dx-1),j);
    end

    hremeltNL(:,j) = (conv(fliplr(fr),hrNL(:,j-1)));
    if j == 2
        hpl(:,j) = hremeltNL((l1)/dx:end-l1/dx,j)/((j-1)*dh0);
        hrNL(:,j) =  dhb(:,j) + (hremeltNL((l1)/dx:end-l1/dx,j));

    else
        hpl(:,j) = hremeltNL((l1)/dx:end-l1/dx,j)/((j-1)*dh0);
        hrNL(:,j) =  dhb(:,j) + (hremeltNL((l1)/dx:end-l1/dx,j));

    end
    hrNL(:,j) =  ([hrNL(7:end,j);zeros(6,1)]);

    dS(:,j+1) = dS(:,j) + dh0;

    Enl(:,j) = (1/dh0)*(Rfs(:,j) - (fft(hrNL(:,j),L)));

end
```

Open-Loop Simulation

```
clear all
%Model Parameters
%Optomec Trial 1; l0 = 0.49, delta = -0.01, l1 = 0.903, b0 = 1.03, m0 =
5.6
%Optomec Trial 1; l0 = 0.61, delta = -0.01, l1 = 1.213, b0 = 0.84, m0 =
9.2
%Unstable Process; l0 = 0.95, delta = -0.01, l1 = 0.200, b0 = 0.54, m0
=
%9.2, mu0 = 0.07
```

```
rho = 7.99e-6;                          %material density [kg/mm3]
l0 = 0.61;                              %characteristic melt pool length
[mm]
delta = -0.01;                          %shifting parameter [mm]
l1 = 1.213;                             %Re-melt char. length 1 [mm]
l2 = l1;                                %Re-melt char. length 2 [mm]
lref = 1;                               %Reference Filter Characteristic
Lenght [mm]
w0 = 0.84;                              %characteristic melt pool width
[mm]
m0 = 9.2/(1000*60);                     %powder flow rate [kg/s]
v0 = 8.47;                              %velocity [mm/s]
alphaL = 50;                            %track length [mm]
padx = 5;                               %length padding [mm]
a1 = 0.01*16.04;                        %catchment function parameter 1 [%]
a2 = 10.57;                             %c.f. parameter 2, max catchment
position [mm]
a3 = 2.04;                              %c.f. parameter 3, function width
param [mm]
dx = 0.02;                              %spatial simulation step size [mm]
M = 10/(0.3);                           %total number of layers to build

%%Solution Points
dS0 = 0.3;                              %Incremental Nozzle Shift Sol.
Input [mm]
dh0 = dS0;                              %Bead Height Solution Point [mm]
mu0 = 0.12;                             %Catchment Sol. Point [kg/kg]
dP0 = a2 - a3*sqrt(-log(mu0/a1));       %Part standoff sol. point [mm]
lambda0 = w0*dh0*rho/mu0;               %Spatial Dep. Rate Sol. Point
[kg/mm]

%%Linearization Coefficients
c1 = -2*lambda0*a1*((dP0-a2)/a3)*Fmu(a1,a2,a3,dP0)/(w0*rho);    %Ds and
H lin. constant
c2 = Fmu(a1,a2,a3,dP0)/(w0*rho);                                %Lambda
lin. constant

[xs,fs] = fshape(l0,delta,dx);                                  %Shape
filter
[xr,fr] = fremelt([l1 l2],dx);                                  %Re-
melt filter
[xr1,fr1] = fremelt([lref lref],dx);
%Reference Filter

x = -padx:dx:(alphaL+padx-dx);
%Position vector
L = max(size(x));                                               %FFT
size

%Find "zero" index
[z1,xgpc] = min(abs(xr));
[z1,xgcc] = min(abs(xs));

%Determine the needed amount of zero padding
```

```
padxb = round((min(xs)-min(xr))/dx);
padxa = round((max(xr)-max(xs))/dx);

%Calculate the composite filters
gp = fr - c1*[zeros(1,padxb) fs zeros(1,padxa)];
gpbar = sum(gp);
gc = c2*lambda0/dh0*fs;
gcbar = sum(gc);

%Form Toeplitz matrices
Fr1 = toeplitz([fr(xgpc:end) zeros(1,L-
max(size(fr(xgpc:end))))],[fr(xgpc) zeros(1,L-1)]);
Fr2 = toeplitz([0 fr(xgpc-1:-1:1) zeros(1,L-max(size(fr(xgpc-1:-1:1)))-
1)],zeros(1,L));
Fr = Fr1 + Fr2';

Fs1 = toeplitz([fs(xgcc+1:end) zeros(1,L-
max(size(fs(xgcc+1:end))))],[fs(xgcc+1) zeros(1,L-1)]);
Fs2 = toeplitz([fs(xgcc:-1:1) zeros(1,L-max(size(fs(xgcc:-
1:1))))],zeros(1,L));
Fs = Fs1 + Fs2';

%%Initial Conditions
hC(:,1) = conv(fr1,[zeros(size(x(x<=0),2),1);0*ones(size(x(x>0 &
x<=12.5),2),1);-2*0.3*ones(size(x(x>12.5 &
x<=37.5),2),1);0*ones(size(x(x>37.5 &
x<=50),2),1);zeros(size(x(x>50),2),1)]);
hnl(:,1) = hC((lref)/dx:end-lref/dx,1);
dS(:,1) = (dP0 - dS0)*ones(size(x,2),1);
lambda(:,1) = lambda0.*[zeros(size(x(x<=0),2),1);...
            1*ones(size(x(x>0 & x<=(alphaL)),2),1);...
            zeros(size(x(x>(alphaL)),2),1)];

%Generate Reference Signals
for j = 1:M
    dS(:,j+1) = dS(:,j) + dS0;

    munl(:,j+1) = Fmu(a1,a2,a3,dS(:,j+1) - hnl(:,j));
    lambda(:,j+1) = lambda(:,j);
    hnl(:,j+1) = Fs*(munl(:,j+1).*lambda(:,j+1)/rho/w0) + Fr*hnl(:,j);
end
```

Powder Catchment Efficiency

```
function mu = Fmu(a1,a2,a3,dp)

    mu = a1.*exp(-((dp-a2)./a3).^2);

end
```

In-Layer Shaping Kernel

```
function [x,fs] = fshape(l,T,dx)
    x = T:dx:(l+T);
    fs = (2/l^2*(x-T).*[zeros(size(x((x-T)<0))) ones(size(x((x-
T)>=0)))] - ...
    2/l^2*(x-l-T).*[zeros(size(x((x-l-T)<0))) ones(size(x((x-l-
T)>=0)))] - ...
     2/(l)*[zeros(size(x((x-l-T)<0))) ones(size(x((x-l-T)>=0)))])*dx;
end
```

Re-Melt Kernel

```
function [x,fr] = fremelt(lengths,dx)
    l1 = lengths(1);
    l2 = lengths(2);
    x = -l1:dx:(l2-dx);

%     D = diag(coeff);

%     fr = D*ones(size(coeff,1),1);

    fr = ((2/((l1+l2)*l1))*(x).*([zeros(size(x((x+l1)<0)))
ones(size(x((x+l1)>=0)))] - ...
        [zeros(size(x((x)<0))) ones(size(x((x)>=0)))]) + ...
        (2/(l1+l2))*([zeros(size(x((x+l1)<0)))
ones(size(x((x+l1)>=0)))] - ...
        [zeros(size(x((x-l2)<0))) ones(size(x((x-l2)>=0)))]) + ...
        (2/(l2*(l1+l2)))*x.*([zeros(size(x((x-l2)<0))) ones(size(x((x-
l2)>=0)))] - ...
        [zeros(size(x((x)<0))) ones(size(x((x)>=0)))]))*dx;
end
```

Stability Region Plot

```
clear all
warning('off','all')
%Model Parameters
%Optomec Trial 1; l0 = 0.49, delta = -0.01, l1 = 0.903, b0 = 1.03, m0 =
5.6
%Optomec Trial 2; l0 = 0.61, delta = -0.01, l1 = 1.213, b0 = 0.84, m0 =
9.2
%Unstable Process; l0 = 0.95, delta = -0.01, l1 = 0.200, b0 = 0.54, m0
=
%9.2, mu0 = 0.07

rho = 7.99e-6;                          %material density [kg/mm3]
l0 = 0.49;                              %characteristic melt pool length
[mm]
delta = -0.01;                          %shifting parameter [mm]
l1 = 0.903;                             %Re-melt char. length 1 [mm]
l2 = l1;                                %Re-melt char. length 2 [mm]
w0 = 1.03;                              %characteristic melt pool width
[mm]
```

```
m0 = 5.6/(1000*60); %powder flow rate [kg/s]
v0 = 8.47;                          %frequency velocity parameter 1
a1 = 0.01*16.04;                    %catchment function parameter 1 [%]
a2 = 10.57;                         %c.f. parameter 2, max catchment
position [mm]
a3 = 2.04;                          %c.f. parameter 3, function width
param [mm]
dx = 0.001;

[xr,fr] = fremelt([l1 l2],dx);          %Re-melt filter
fs = fshape(l0,delta,dx);           %Shape filter

x = -10:dx:60;
L = max(size(x));
w = linspace(1e-6,1e2,L);

for i = 1:max(size(w))
    s = 2*pi*1i*w(i);
    Fs(i) = 2*(1-(1+s*l0)*exp(-l0*s))/(s^2*l0^2)*exp(-delta*s);
    Fr(i) = 2/((l1+l2)*l1*s^2)*(exp(l1*s)-1) +
2/(s^2*l2*(l1+l2))*(exp(-l2*s)-1);
end

%Solution Points
dh0 = 0:0.01:5;                                     %Bead Height
Solution Point [mm]
dP0 = 2:0.01:14;                                    %Part standoff
sol. point [mm]
lambda0 = linspace(1e-8,1e-3,100);

for k = 1:max(size(lambda0))

    for j = 1:max(size(dP0))
        mu0 = Fmu(a1,a2,a3,dP0(j));
        c(k,j) = -2*lambda0(k)*a1*((dP0(j)-a2)/a3)*mu0/(w0*rho);
        cond = Fr - c(k,j)*Fs;
        stable(k,j) = max(abs(cond));
        ustable(k,j) = stable(k,j);
        if stable(k,j) > 1.01
            stable(k,j) = 1.01;
        end
    end
end

Idh0S = find((dh0 == (0.380)));
IdP0S = find((dP0 == (9.8)));
IdP0U = find((dP0 == (11.4)));

StabilityPlot(dP0,lambda0,stable,[0:0.4:0.8 0.9 0.999 0.99999],[IdP0S
Idh0S IdP0U Idh0S],lambda0);
```

APPENDIX B

DATA

This Appendix presents data gathered on the Optomec MR-7 LENS, but not used in the exposition above. Several other operating points were tested and models fit to the data. However, in general, these results are not as clean as those presented in the main body of the work and possessed a small Signal to Noise Ratio (SNR). Each operating point is characterized by a set of process parameters listed first, then spatial domain plots of the in-layer and the re-melt response are given. Finally, Bode diagrams of the modeled responses and a table of the identified model parameters are presented.

MODEL B1

Table B.1 lists the process parameters used to conduct the depositions for Model 1. Figures B.1 and B.2 show the spatial domain in-layer and re-melt measured and modeled responses, respectively. Figure B.3 shows the frequency domain responses of the modeled kernels. Finally, Table B.2 lists the identified model parameters.

Table B.1. Process parameters for Model B1.

Process Parameter	**Value**
Laser Power, Q (W)	600
Scan Speed, v (mm/s)	23.3
Powder Flow Rate, m (g/min)	9.2
Substrate Standoff, d_S (mm)	9.525

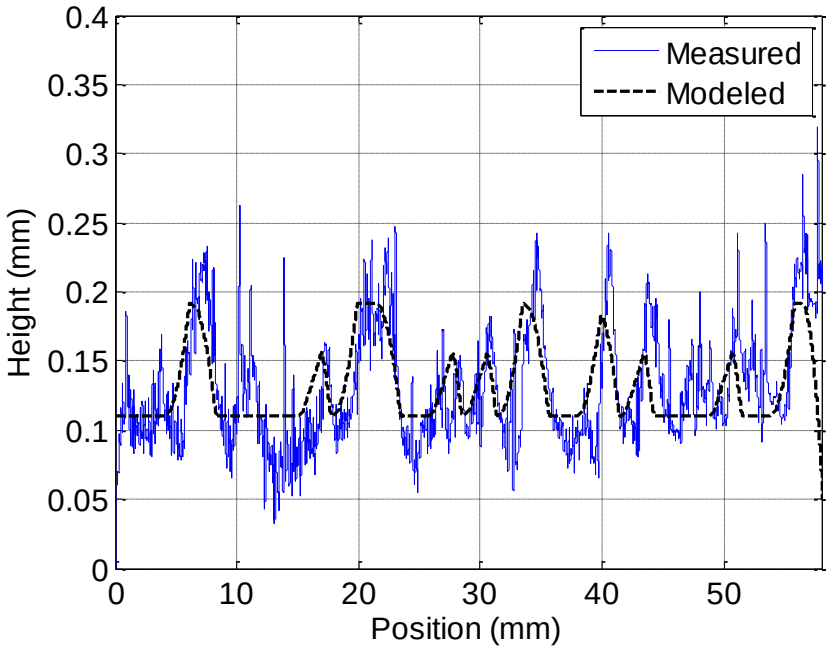

Figure B.1. Spatial domain measured and modeled in-layer dynamic response for Model B1.

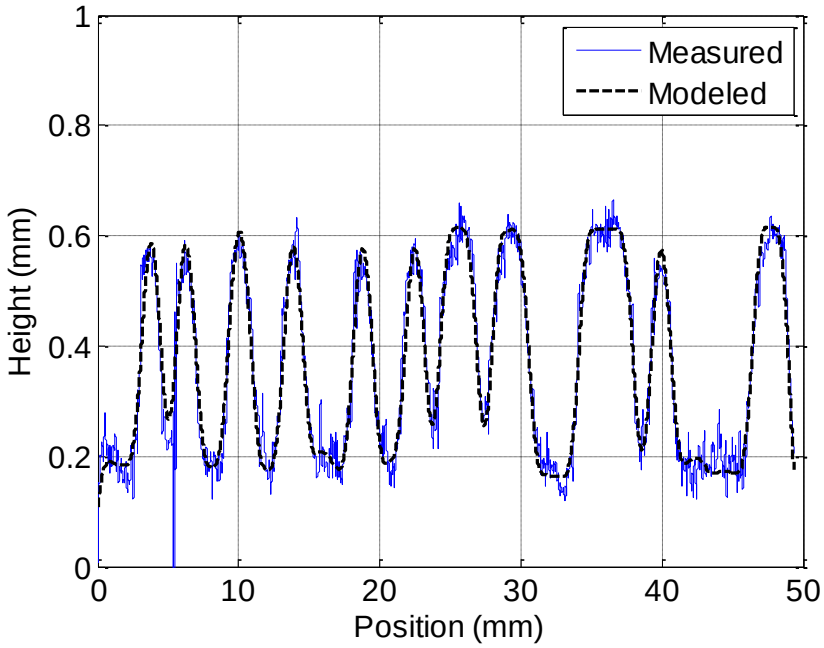

Figure B.2. Spatial domain measured and modeled re-melt dynamic response for Model B1.

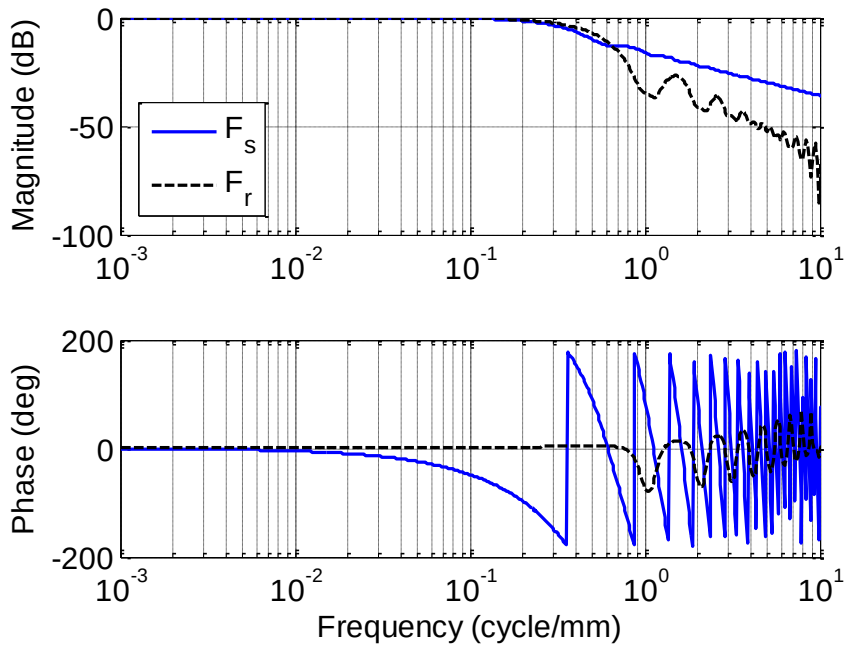

Figure B.3. Bode diagram of both identified dynamic processes for Model B1.

Table B.2. Model parameters identified for Model B1.

Model Parameter	**Value**
Characteristic Melt Pool Length, l_0 (mm)	2.00
Lead Parameter, δ (mm)	-.001
Re-Melt Lead Parameter, l_1 (mm)	1.01
Re-Melt Lag Parameter, l_2 (mm)	0.91

MODEL B2

Table B.3 lists the process parameters used to conduct the depositions for Model 2. Figures B.4 and B.5 show the spatial domain in-layer and re-melt measured and modeled responses, respectively. Figure B.6 shows the frequency domain responses of the modeled kernels. Finally, Table B.4 lists the identified model parameters.

Table B.3. Process parameters for Model B2.

Process Parameter	**Value**
Laser Power, Q (W)	600
Scan Speed, v (mm/s)	10.6
Powder Flow Rate, m (g/min)	7.4
Substrate Standoff, d_S (mm)	9.525

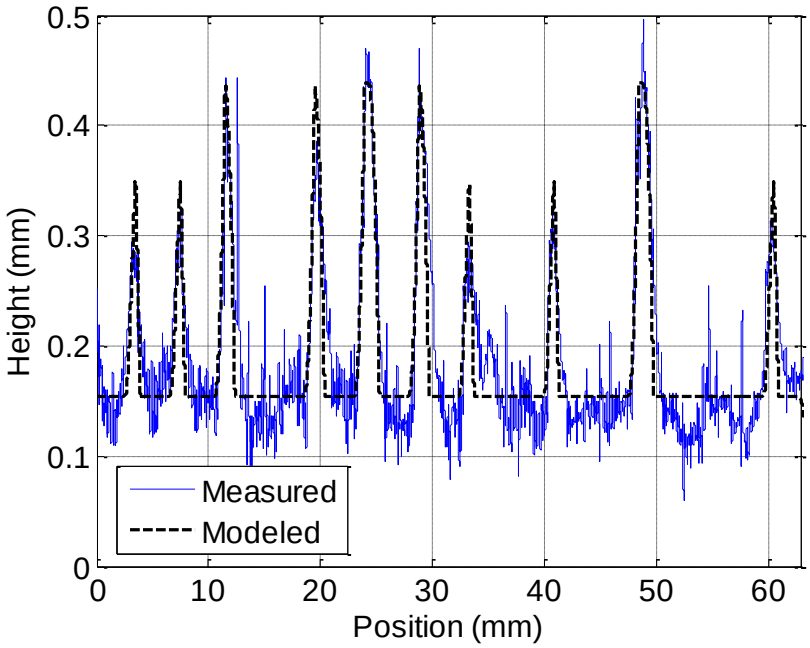

Figure B.4. Spatial domain measured and modeled in-layer dynamic responses for Model B2.

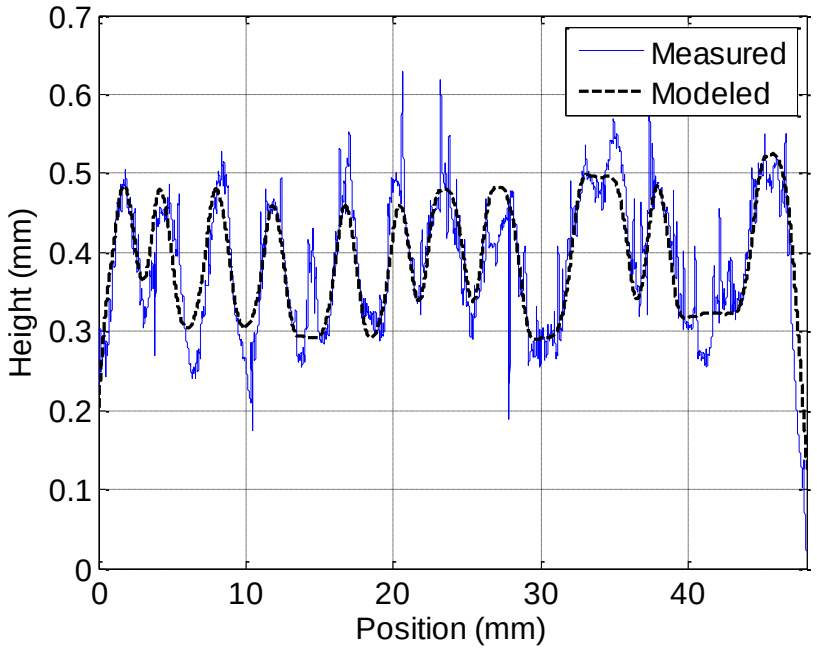

Figure B.5. Spatial domain measured and modeled re-melt dynamic responses for Model B2.

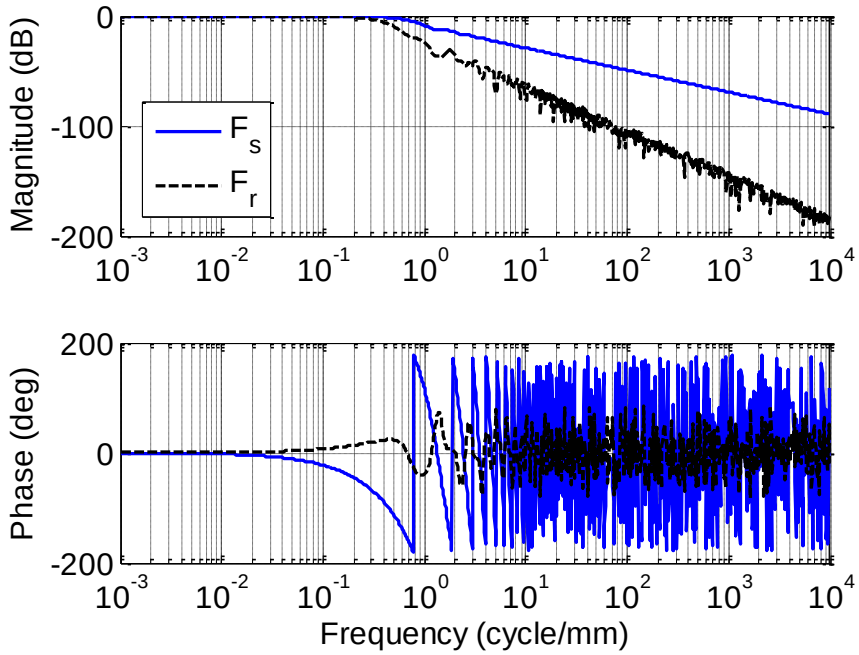

Figure B.6. Bode diagram of both identified dynamic processes for Model B2.

Table B.4. Model parameters identified for Model B2.

Model Parameter	**Value**
Characteristic Melt Pool Length, l_0 (mm)	0.927
Lead Parameter, δ (mm)	-0.001
Re-Melt Lead Parameter, l_1 (mm)	1.378
Re-Melt Lag Parameter, l_2 (mm)	0.795

MODEL B3

Table B.5 lists the process parameters used to conduct the depositions for Model 3. Figures B.7 and B.8 show the spatial domain in-layer and re-melt measured and modeled responses, respectively. Figure B.9 shows the frequency domain responses of the modeled kernels. Finally, Table B.6 lists the identified model parameters.

Table B.5. Process parameters for Model B3.

Process Parameter	**Value**
Laser Power, Q (W)	550
Scan Speed, v (mm/s)	10.6
Powder Flow Rate, m (g/min)	7.4
Substrate Standoff, d_S (mm)	9.525

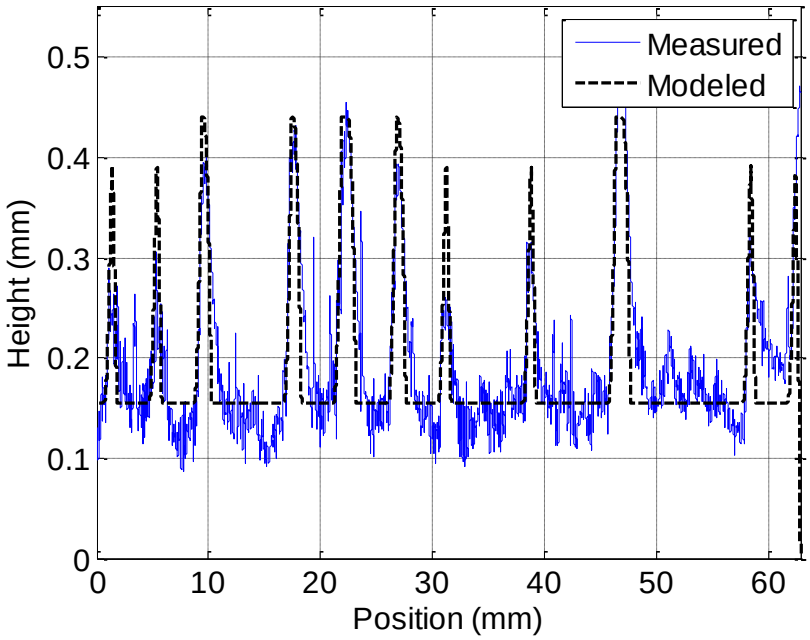

Figure B.7. Spatial domain measured and modeled in-layer dynamic responses for Model B3.

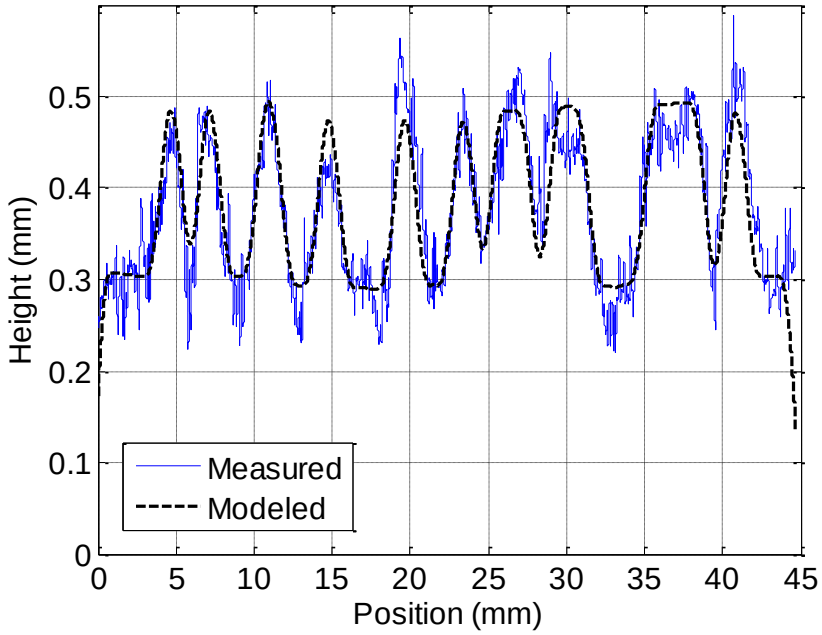

Figure B.8. Spatial domain measured and modeled re-melt dynamic responses for Model B3.

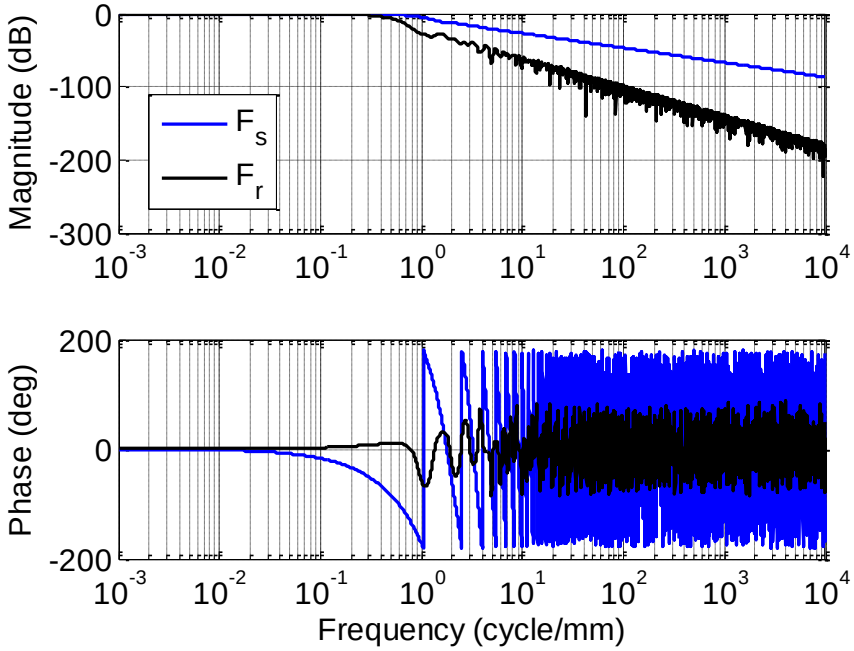

Figure B.9. Bode diagram of both identified dynamic processes for Model B3.

Table B.6. Model parameters identified for Model B3.

Model Parameter	**Value**
Characteristic Melt Pool Length, l_0 (mm)	0.691
Lead Parameter, δ (mm)	-5×10^{-4}
Re-Melt Lead Parameter, l_1 (mm)	1.023
Re-Melt Lag Parameter, l_2 (mm)	0.809

MODEL B4

Table B.7 lists the process parameters used to conduct the depositions for Model B4. Figures B.10 and B.11 show the spatial domain in-layer and re-melt measured and modeled responses, respectively. Figure B.12 shows the frequency domain responses of the modeled kernels. Finally, Table B.8 lists the identified model parameters.

Table B.7. Process parameters for Model B4.

Process Parameter	**Value**
Laser Power, Q (W)	550
Scan Speed, v (mm/s)	23.3
Powder Flow Rate, m (g/min)	3.8
Substrate Standoff, d_S (mm)	9.525

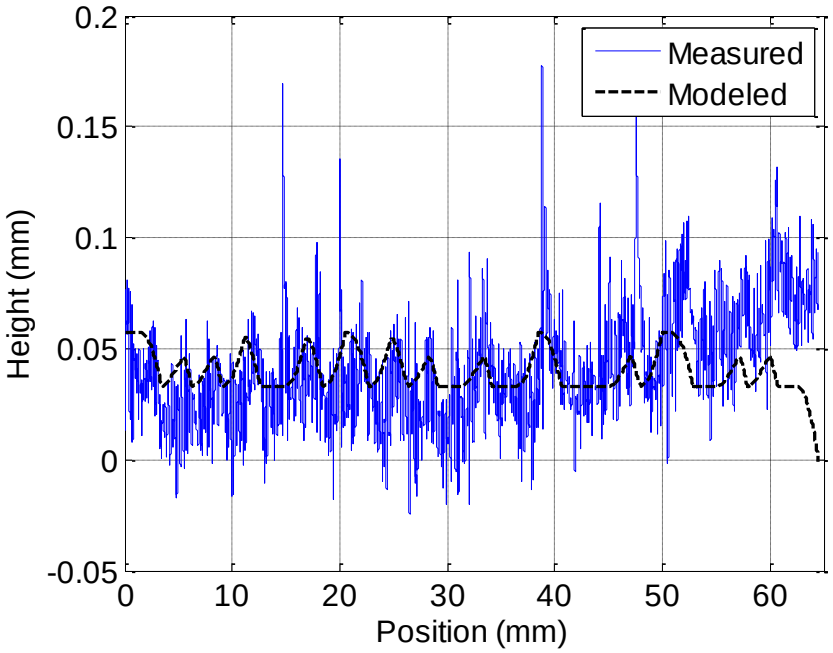

Figure B.10. Spatial domain measured and modeled in-layer dynamic responses for Model B4.

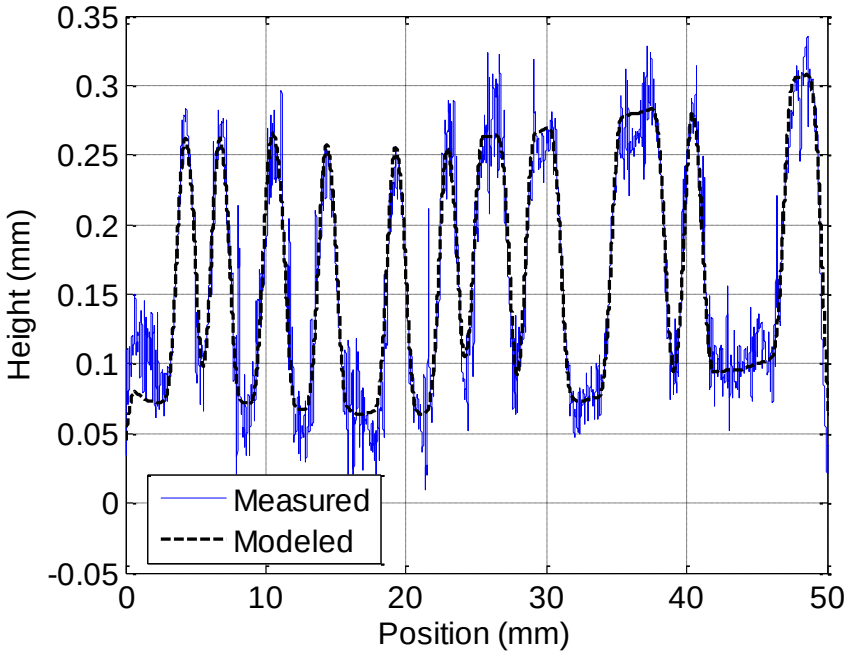

Figure B.11. Spatial domain measured and modeled in-layer dynamic responses for Model B4.

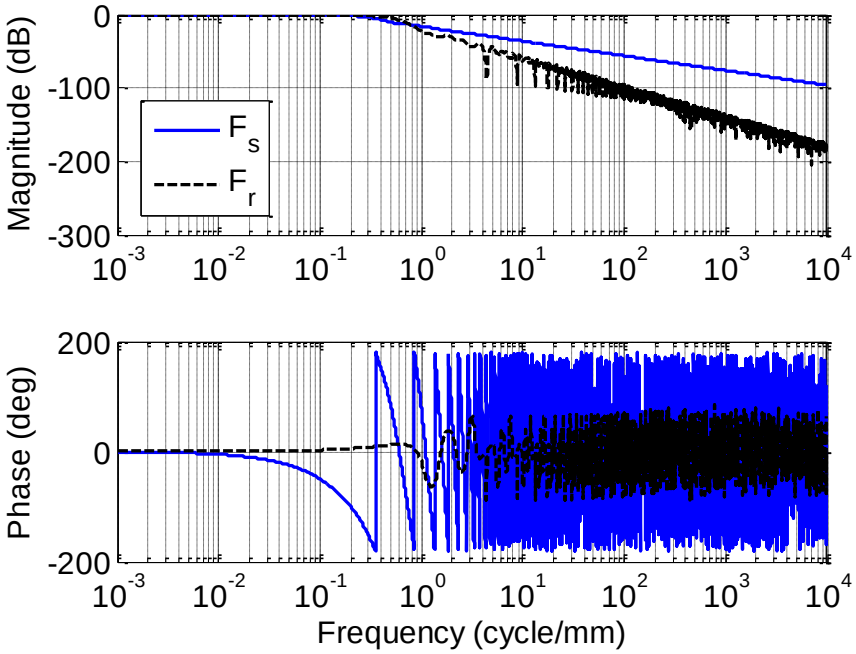

Figure B.12. Bode diagram of both identified dynamic processes for Model B4.

Table B.8. Model parameters identified for Model B4.

Model Parameter	**Value**
Characteristic Melt Pool Length, l_0 (mm)	2.037
Lead Parameter, δ (mm)	-.001
Re-Melt Lead Parameter, l_1 (mm)	0.911
Re-Melt Lag Parameter, l_2 (mm)	0.683

MODEL B5

Table B.9 lists the process parameters used to conduct the depositions for Model B5. Figures B.13 and B.14 show the spatial domain in-layer and re-melt measured and modeled responses, respectively. Figure B.15 shows the frequency domain responses of the modeled kernels. Finally, Table B.10 lists the identified model parameters.

Table B.9. Process parameters for Model B5.

Process Parameter	**Value**
Laser Power, Q (W)	600
Scan Speed, v (mm/s)	23.3
Powder Flow Rate, m (g/min)	3.8
Substrate Standoff, d_S (mm)	9.525

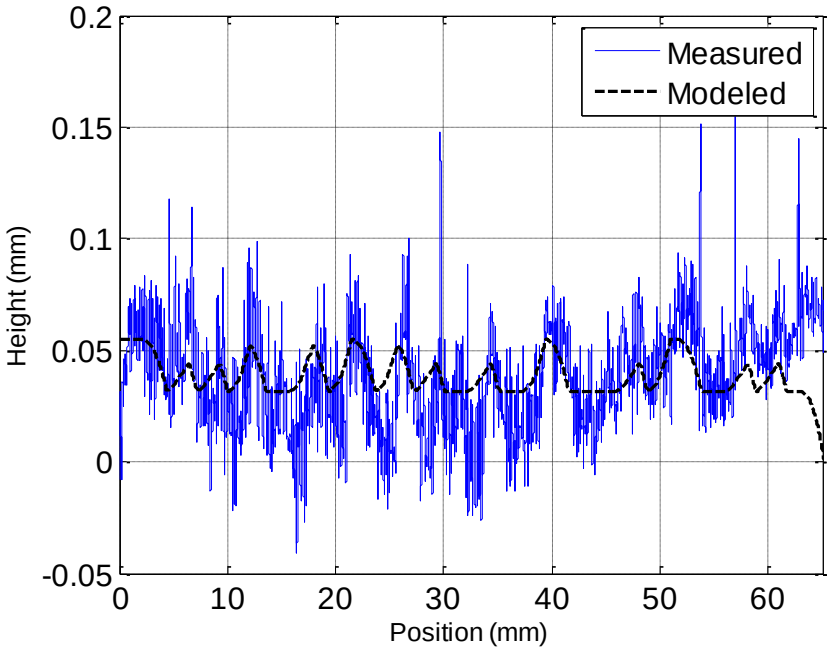

Figure B.13. Spatial domain measured and modeled in-layer dynamic responses for Model B5.

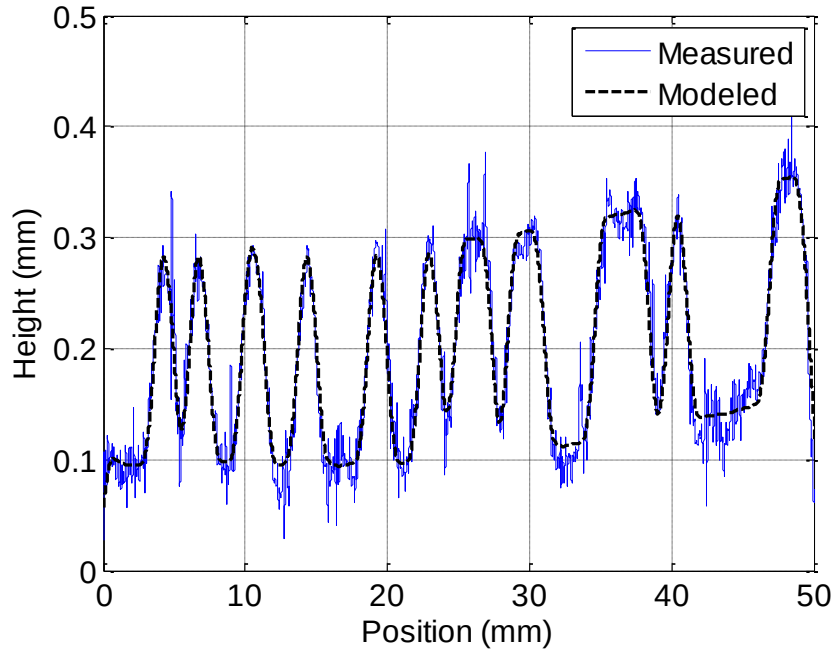

Figure B.14. Spatial domain measured and modeled in-layer dynamic responses for Model B5.

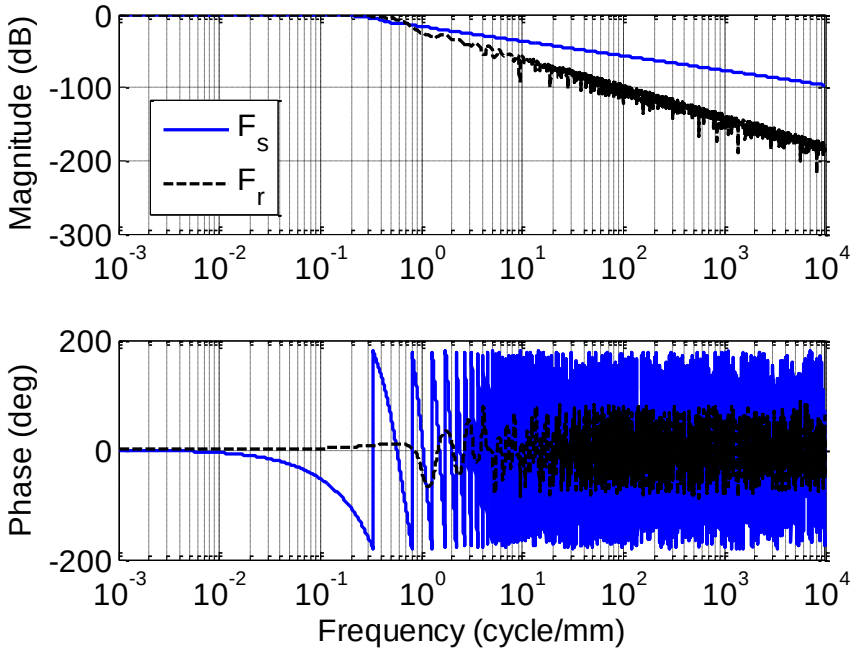

Figure B.15. Bode diagram of both identified dynamic processes for Model B5.

Table B.10. Model parameters identified for Model B5.

Model Parameter	**Value**
Characteristic Melt Pool Length, l_0 (mm)	2.162
Lead Parameter, δ (mm)	-.001
Re-Melt Lead Parameter, l_1 (mm)	0.957
Re-Melt Lag Parameter, l_2 (mm)	0.743

POWDER CATCHMENT EFFICIENCY

In this subsection of Appendix B, data for two other powder feeder motor speeds is presented. These deposited tracks are shown in Figure 3.1, though the individual tracks are not highlighted. Table B.11 givens the motor speeds and measured powder flow rates for the extra trials. Note that the 10 RPM powder feeder motor speed does not follow the linear increase in powder flow rate observed at the other set points.

Table B.11. Powder feeder motor speed command and measured powder flow rates for powder catchment efficiency characterization.

Powder Feeder Motor Speed (RPM)	Powder Flow Rate (g/min)
1	1.6
10	8.5

Figures B.16 and B.17 show the measured powder catchment distributions for the 1 RPM and 10 RPM powder feeder motor speeds, respectively. The trial numbers correspond the tracks shown in Figure 3.1, where Trial 1 is located at the bottom of the photograph. As with the powder catchment efficiency identification, the measurements are noisy. In particular, the 1 RPM tests do not agree past approximately d_P = 9 mm and Trial 3 is exhibits more noise relative to Trial 7.

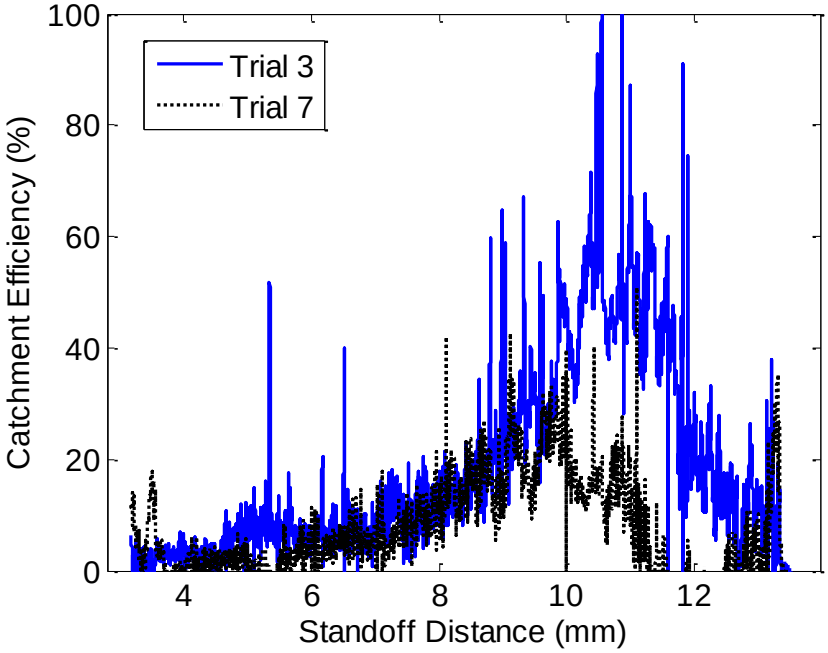

Figure B.16. Measured catchment efficiency as a function of standoff distance for powder feeder motor speed 1 RPM.

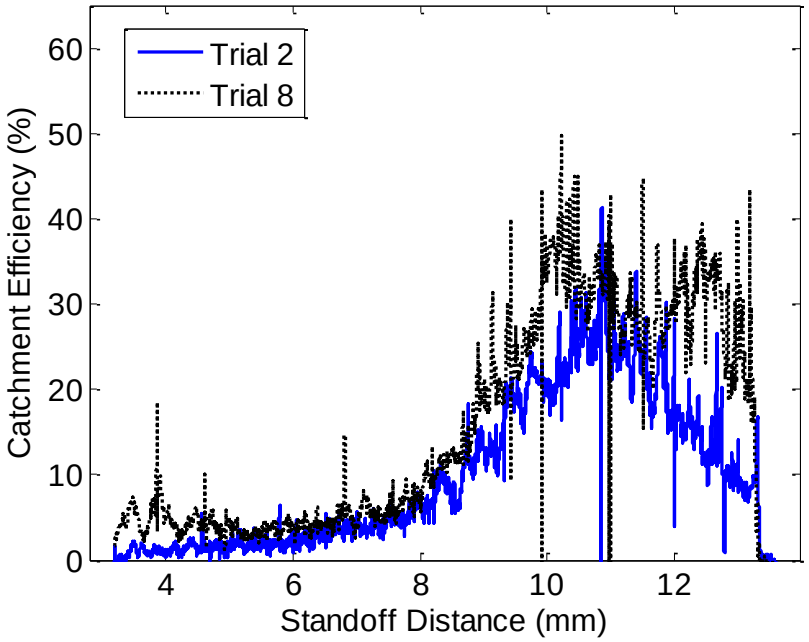

Figure B.17. Measured catchment efficiency as a function of standoff distance for powder feeder motor speed 10 RPM.

BIBLIOGRAPHY

[1] Huang, Y. and Leu, M.C., "Frontiers of Additive Manufacturing Research and Education," 2014, University of Florida, Center for Manufacturing Innovation, Gainesville, FL.

[2] Pandey, P.M., Reddy, N.V., Dhande, S.G., 2003, "Slicing Procedures in Layered Manufacturing: A Review," *Rapid Prototyping Journal*, vol. 9, no. 5, pp. 274-288.

[3] "Measurement Science Roadmap for Metal-Based Additive Manufacturing," 2013, Energetics Incorporated, National Institute of Standards and Technology, Columbia, MD.

[4] "Roadmap for Additive Manufacturing: Identifying the Future of Freeform Processing," 2009, The University of Texas at Austin, Laboratory of Freeform Fabrication, Austin, TX.

[5] Optomec, "LENS Process Monitoring and Controls," www.optomec.com/datasheets-additive-manufacturing, accessed 28 October 2015.

[6] Sammons, P.M., Bristow, D.A., Landers, R.G., 2013, "Height Dependent Laser Metal Deposition Process Modeling," *ASME Journal of Manufacturing Science and Engineering*, vol. 135, no. 5, pp. 054501:1-7.

[7] Ruan, J., Tang, L., Liou, F.W., Landers, R.G., 2010, "Direct Three-Dimensional Layer Metal Deposition," *ASME Journal of Manufacturing Science and Engineering*, vol. 132, no. 6, pp. 064502:1-6.

[8] Mazumder, J., Choi, J., Nagarathnam, K., Koch, J., Hetzner, D., 1997, "The Direct Metal Deposition of H13 Tool Steel for 3-D Components," *Journal of Materials*, vol. 49, no. 5, pp. 55-60.

[9] Mazumder, J., Dutta, D., Kikuchi, N., Ghosh, A., 2000, "Closed Loop Direct Metal Deposition: Art to Part," *Optics and Lasers in Engineering*, vol. 34, no. 4-6, pp. 397-414.

[10] Atwood, C., Griffith, M., Harwell, L., Schlienger, E., Ensz, M., Smugeresky, J., Romero, T., Greene, D., Reckaway, D., 1998, "Laser Engineered Net Shaping (LENS (TM)): A Tool for Direct Fabrication of Metal Parts," *17th International Congress on Applications of Lasers and Electro-Optics*, Orlando, FL, Nov. 16-19.

[11] Baufelt, B. and Van der Biest, O., 2009, "Mechanical Properties of Ti-6Al-4V Specimens Produced by Shaped Metal Deposition," *Science and Technology of Advanced Materials*, vol. 10, no. 1, pp. 015008:1-10.

[12] Paul, C.P., Ganesh, P., Mishra, S.K., Bhargava, P., Negi, J., Nath, A.K., 2007, "Investigating Laser Rapid manufacturing for Inconel-625 Components," *Optics and Laser Technology*, vol. 39, no. 4, pp. 800-805.

[13] Peyre, P., Aubry, P., Fabbro, R., Longuet, A., 2008, "Analytical and Numerical Modeling of the Direct Metal Deposition Laser Process," *Journal of Physics D: Applied Physics*, vol. 41, no. 2, pp. 025403:1-10.

[14] Doumanidis, C. and Kwak, Y-M., 2001, "Geometry Modeling and Control by Infrared and Laser Sensing in Thermal Manufacturing with Material Deposition," *ASME Journal of Manufacturing Science and Engineering*, vol. 123, no. 1, pp. 45–52.

[15] Pinkerton, A. and Li, L., 2004, "Modelling the Geometry of a Moving Laser Melt Pool and Deposition Track via Energy and Mass Balances," *Journal of Physics D: Applied Physics*, vol. 37, no. 14, pp. 1885-1895.

[16] Munjuluri, B.N.R., 2001,"Process Modeling, Monitoring and Control of Laser Metal Forming," MS Thesis, University of Missouri, Rolla.

[17] Fathi, A., Khajepuor, A., Toyserkani, E., Durali, M., 2007, "Clad Height Control in Laser Solid Freeform Fabrication using a Feedforward PID Controller," *International Journal of Advanced Manufacturing Technology*, vol. 35, no. 3-4, pp. 280-292.

[18] Boddu, M.R., Musti, S., Landers, R.G., Agarwal, S., Liou, F.W., 2001, "Empirical Modeling and Vision Based Control for Laser Aided Metal Deposition Process," *Solid Freeform Fabrication Symposium*, Austin, TX, Aug. 6-8.

[19] Sammons, P.M., Bristow, D.A., Landers, R.G., 2014, "Frequency Domain Identification of a Repetitive Process Control Oriented Model for Laser Metal Deposition Processes," *International Symposium on Flexible Automation*, Awaji-Island, Hyogo, Japan, July 14-16.

[20] Sammons, P.M., Bristow, D.A., Landers, R.G., 2014, "Control-Oriented Modeling of Laser Metal Deposition as a Repetitive Process," *American Control Conference*, Portland, OR, June 4-6.

[21] Rogers, E., Galkowski, K., Owens, D.H., *Control Systems Theory and Applications for Linear Repetitive Processes*, Berlin, Springer, 2007.

[22] Edwards, J.B., 1974, "Stability Problems in the Control of Multipass Processes," *Proceedings of the Institution of Electrical Engineers*, vol. 121, no. 11, pp. 1425-1432.

[23] Galkowski, K., Rogers, E., Owens, D.H., 1999, "New 2D Models and a Transition Matrix for Discrete Linear Repetitive Processes," *International Journal of Control*, vol. 72, no. 15, pp. 1365-1380.

[24] Dymkov, M., Gaishun, I., Galkowski, K., Rogers, E., Owens, D.H., 2002, "Exponential Stability of Discrete Linear Repetitive Processes," *International Journal of Control*, vol. 75, no. 12, pp. 861-869.

[25] Rocha, P., Rogers, E., Owens, D.H., 1996, "Stability of Discrete Non-Unit Memory Linear Repetitive Processes – A Two-Dimensional Systems Interpretation," *International Journal -of Control*, vol. 63, no. 3, pp. 457-482.

[26] Sulikowski, B., Galkowski, K., Rogers, E., Owens, D.H., 2006, "PI Control of Discrete Linear Repetitive Processes," *Automatica*, vol. 42, no. 5, pp. 877-880.

[27] Galkowski, K., Rogers, E., Xu, S., Lam, J., Owens, D.H., 2002, "LMIs – A Fundamental Tool in Analysis and Controller Design for Discrete Linear Repetitive Processes," *IEEE Transactions on Circuits*, vol. 49, no. 6, pp. 768-778.

[28] Paszke, W., Galkowski, K., Rogers, E., Owens, D.H., 2006, "H_∞ and Guaranteed Cost Control of Discrete Linear Repetitive Processes," *Linear Algebra and its Applications*, vol. 412, no. 2-3, pp. 93-131.

[29] Qi, H., Mazumder, J., Ki, H., 2006, "Numerical Simulation of Heat Transfer and Fluid Flow in Coaxial Laser Cladding Process for Direct Metal Deposition," *Journal of Applied Physics*, vol. 100, no. 2, pp. 024903:1-11.

[30] Lei, Y.P., Murakawa, H., Shi, Y.W., Li, X.Y., 2001, "Numerical Analysis of the Competitive Influence of Marangoni Flow and Evaporation on Heat Surface Temperature and Molten Pool Shape in Laser Surface Remelting," *Computational Materials Science*, vol. 21, no. 3, pp. 276-290.

[31] Picasso, M. and Hoadley, A.F.A., 1994, "Finite Element Simulation of Laser Surface Treatments including Convection in the Melt Pool," *International Journal of Numerical Methods for Heat and Fluid Flow*, vol. 4, no. 1, pp. 61-83.

[32] Hoadley, A.F.A. and Rappaz, M., 1992, "A Thermal Model of Laser Cladding by Powder Injection," *Metallurgical Transactions B*, vol. 23, no. 5, pp. 631-642.

[33] Kaplan, A.F.H. and Groboth, G., 2001, "Process Analysis of Laser Beam Cladding," *ASME Journal of Manufacturing Science and Engineering*, vol. 123, no. 4, pp. 609-614.

[34] Steen, W.M., Weerasinghe, V.M., Monson, P., 1986, "Some Aspects of the Formation of Laser Clad Tracks," *Proceedings of SPIE 0650, High Power Lasers and Their Industrial Applications*, Innsbruck, Austria, Oct. 21.

[35] Picasso, M., Marsden, C.F., Wagniere, J.D., Frenk, A., Rappaz, M., 1994, "A Simple but Realistic Model for Laser Cladding," *Metallurgical and Materials Transactions B*, vol. 25, no. 2, pp. 281-291.

[36] Srivastava, D., Chang, I.T.H., Loretto, M.H., 2001, "The Effect of Process Parameters and Heat Treatment on the Microstructure of Direct Laser Fabricated TiAl Alloy Samples," *Intermetallics*, vol. 9, no. 12, pp. 1003-1013.

[37] Lin, J., 1999, "A Simple Model of Powder Catchment Coaxial Laser Cladding," *Optics and Laser Technology*, vol. 31, no. 3, pp. 233-238.

[38] Kang, B., Waldvogel, J., Poulikakos, D., 1995, "Remelting Phenomena in the Process of Splat Solidification," *Journal of Materials Science*, vol. 30, pp. 4912-4925.

[39] Wang, S.-P., Wang, G.-X., Matthys, E.F., 1998, "Melting and Resolidification of a Substrate in Contact with a Molten Metal: Operational Maps," *International Journal of Heat Transfer*, vol. 41, no. 10, pp. 1177-1188.

[40] Luo, J., Pan, H., Kinzel, E.C., 2014, "Additive Manufacturing of Glass," *ASME Journal of Manufacturing Science and Engineering*, vol. 136, no. 6, pp. 061024:1-6.

[41] Knapp, C.H. and Carter, G.C., 1976, "The Generalized Correlation Method for Estimation of Time Delay," *IEEE Transactions on Acoustics, Speech, and Signal Processing*, vol. 24, no. 4, pp. 320-323.

[42] Prepelita, V., "Multiple (*n*,*m*)-Hybrid Laplace Transformation and Applications to Multidimensional Hybrid Systems, Part I," *University Polictehnica of Bucharest Scientific Bulletin, Series A*, vol. 72, no. 2, 2010, pp. 105-120.

[43] Godfrey, K., ed., 1993, *Perturbation Signals for System Identification*, Prentice Hall, New York.

[44] Eskinat, E., Johnson, S.H., Luyben, W.L., 1991, "Use of Hammerstein Models in Identification of Nonlinear Systems," *AIChE Journal*, vol. 37, no. 2., pp. 255-268.

[45] Sammons, P.M., Bristow, D.A., Landers, R.G., "Repetitive Process Control of Additive Manufacturing with Application to Laser Metal Deposition, Part I: Two-Dimensional Modeling and System Identification," *IEEE Transactions on Control Systems Technology* (under review).

[46] Tang, L., Landers, R.G., 2010, "Melt Pool Temperature Control for Laser Metal Deposition Processes, Part I: Online Temperature Control," *ASME Journal of Manufacturing Science and Engineering*, vol. 132, no. 1, pp. 011010:1-9.

[47] Fathi, A., Khajepour, A., Durali, M., Toyserkani, E., 2008, "Geometry Control of the Deposited Layer in a Nonplanar Laser Cladding Process Using a Variable Structure Controller," *ASME Journal of Manufacturing Science and Engineering*, vol. 130, no. 3, pp. 031003:1-11.

[48] Heralic, A., Christiansson, A-K., Lennartson, B., 2012, "Height Control of Laser Metal-Wire Deposition based on Iterative Learning Control and 3D Scanning," *Optics and Lasers in Engineering*, vol. 50, pp. 1230-1241.

[49] Song, L., Bagavath-Singh, V., Dutta, B., Mazumder, J., 2012, "Control of Melt Pool Temperature and Deposition Height during Direct Metal Deposition Process," *International Journal of Advanced Manufacturing Technology*, vol. 58, no 1, pp. 247-256.

[50] Chen, C.-T., *Linear System Theory and Design*, New York, Oxford University Press, 2009.

[51] Mireles, J., Terrazas, C., Gaytan, S.M., Roberson, D.A., Wicker, R.B., 2015, "Closed-Loop Automatic Feedback Control in Electron Beam Melting," *International Journal of Advanced Manufacturing Technology*, in press.

[52] Craeghs, T., Bechmann, F., Berumen, S., Kruth, J-P., 2010, "Feedback Control of Layerwise Laser Melting Using Optical Sensors," *Physics Procedia*, vol. 5 no. 2, pp. 505-514.

[53] Raghunath, N., Pandey, P.M., 2007, "Improving Accuracy Through Shrinkage Modelling Using Taguchi Method in Selective Laser Sintering," *International Journal of Machine Tools and Manufacture*, vol. 47, no. 6, pp. 985-995.

[54] Tang, L., Landers, R.G., 2011, "Layer-to-Layer Height Control for Laser Metal Deposition Process," *ASME Journal of Manufacturing Science and Engineering*, vol. 133, no. 4, pp. 021009:1-9.

[55] Vasinonta, A., Beuth, J.L., Griffith, M., 2007, "Process Maps for Predicting Residual Stress and Melt Pool Size in Laser-Based Fabrication of Thin-Walled Structures," *ASME Journal of Manufacturing Science and Engineering*, vol. 129, no. 2, pp. 101-109.

[56] Zhou, C., Chen, Y., 2012, "Additive Manufacturing based on Optimized Mask Video Projection for Improved Accuracy and Resolution," *Journal of Manufacturing Processes*, vol. 14, no. 2, pp. 107-118.

[57] Gockel, J., Beuth, J., Taminger, K., 2014, "Integrated Control of Solidification Microstructure and Melt Pool Dimensions in Electron Beam Wire Feed Additive Manufacturing on Ti-6Al-4V," *Additive Manufacturing*, vol. 1, no. 1, pp. 119-126.

[58] Limaye, A.S., Rosen, D.W., 2007, "Process Planning Method for Mask Projection Micro-Stereolithography," *Rapid Prototyping Journal*, vol. 13, no. 2, pp. 76-84.

[59] Sammons, P.M., Bristow, D.A., Landers, R.G., "Repetitive Process Control of Additive Manufacturing with Application to Laser Metal Deposition, Part II: Stability and Layer-to-Layer Control," *IEEE Transactions on Control Systems Technology*, to be submitted.

[60] Omer, E-S. A., Moore, K.L., 2011, "Norm-Optimal Control of Time-Varying Discrete Repetitive Processes with Iteration-Varying Reference Inputs," 7th *International Workshop on Multidimensional Systems*, Sept. 5-7, Poitiers, France.

[61] Ladson, L.S., Mitter, S.K., Waren, A.D., 1967, "The Conjugate Gradient Method for Optimal Control Problems," *IEEE Transactions on Automatic Control*, vol. 12, no. 2, pp. 132-138.

[62] Shewchuk, J.R., 1994, "An introduction to the conjugate gradient method without the agonizing pain."

[63] Pagurek, B., Woodside, C.M., 1968, "The Conjugate Gradient Method for Optimal Control Problems with Bounded Control Variables," *Automatica*, vol. 4, no. 5-6, pp. 337-349.

[64] Bristow, D.A., Tharayil, M., Alleyne, A.G., 2006, "A Survey of Iterative Learning Control," *IEEE Control Systems Magazine*, vol. 26, no. 3, pp. 96-114.

[65] Lu, L., Zheng, J., Mishra, S., 2015, "A Layer-to-Layer Model and Feedback Control of Ink-Jet 3-D Printing," *IEEE Transactions on Mechatronics*, vol. 20, no. 3, pp. 1056-1068.

[66] Garcia, C.E., Prett, D.M., Morari, M., 1989, "Model Predictive Control: Theory and Practice – A Survey," *Automatica*, vol. 25, no. 3, pp. 335-348.

[67] Pannocchia, G., Kerrigan, E.C., 2005, "Offset-Free Receding Horizon Control of Constrained Linear Systems," *AIChE Journal*, vol. 51, no. 12, pp. 3134-3146.

[68] Maeder, U., Borrelli, F., Morari, M., 2009, "Linear Offset-Free Model Predictive Control," *Automatica*, vol. 45, pp. 2214-2222.

[69] Optomec, 2014 "LENS MR-7," Datasheet, Accessed 20 October 2015.

[70] Optomec, 2014, "LENS Print Engine," Datasheet, Accessed 20 October 2015.

VITA

Patrick Michael Sammons was born in Bridgeton, Missouri. Patrick earned his Bachelor of Science in Mechanical Engineering from the University of Missouri – Columbia in 2009. In 2010, he joined the Mechanical and Aerospace Engineering Department at Missouri University of Science and Technology and completed his Master of Science in Mechanical Engineering there in 2012. In July 2016, he received his Ph.D. in Mechanical Engineering from Missouri University of Science and Technology. In August 2016, he joined the University of Michigan as a Post-Doctoral Research Fellow.